University of California
Santa Barbara

Transport Properties of III-N Hot Electron Transistors

A dissertation submitted in partial satisfaction
of the requirements for the degree

Doctor of Philosophy
in
Physics

by

Donald J. Suntrup III

Committee in charge:

Professor Umesh Mishra, Co-Chair
Professor Mark Sherwin, Co-Chair
Professor John Martinis
Professor Debdeep Jena

December 2015

The Dissertation of Donald J. Suntrup III is approved.

Professor John Martinis

Professor Debdeep Jena

Professor Mark Sherwin, Committee Co-Chair

Professor Umesh Mishra, Committee Co-Chair

September 2015

Transport Properties of III-N Hot Electron Transistors

by

Donald J. Suntrup III

For my parents,
Butch and Mary,
and for Darcey.

Acknowledgements

I am convinced beyond a doubt that this work would not have been possible without the support of many wonderful individuals. If I have learned anything in graduate school I've learned that a Ph.D. truly takes a village.

First and foremost I'd like to thank Umesh for providing such a stimulating research environment. I came to Umesh in my fourth year looking for a new research project. I must not have hidden my anxiety very well because I found out later that Umesh had noticed a terrified look on my face. He was kind enough to take a chance on a middle-aged grad student even though I had only an elementary knowledge of device physics and little to no experience doing device research. My time in his group turned out to be challenging but ultimately very satisfying. Umesh deserves credit not only for his renowned research chops but also for his seemingly boundless wisdom. It was a sincere privilege to have worked with him.

Many thanks to my committee members Mark Sherwin, John Martinis, and DJ. I managed to somehow find three superbly distinguished professors who were also willing to spend some of their precious time discussing my little research project. I am very grateful for their interest and advice.

As any current or former Mishra group student knows, none of the materials development would be possible without Stacia. The vastness of her MOCVD knowledge is almost incomprehensible. Not only is Stacia willing to talk through a tedious technical problem but she's also happy to sit around and riff about life. We are all so lucky to know her.

I want to thank the rest of the HET team who slogged through the past few years with me in fits and occasional starts. Geetak, in particular, was my research partner in crime, always willing to cheerfully entertain whatever idea or theory I had cooked up that

day and provide level-headed and intelligent feedback. I am sure that I would not have been able to complete this project in two and a half years without him. Matt Laurent was my gateway into the Mishra group. He was incredibly patient with me as the TA of the device physics class and later, after talking over coffee, pulled some strings to get me a job in the group. I am sure he is not aware of how much of a relief his help was. Haoran shouldered the vast majority of the growth work presented in this thesis. Her persistence and focus were astounding. There were periods of three or four months where growth after growth failed to turn out any working devices and she somehow kept at it. I am so grateful for the mornings we spent next to the MOCVD reactor chatting about nothing to keep from losing our minds. Lastly, I want to thank Elaheh, the intrepid keeper of the MBE machine. Always willing to go the extra mile or stay the extra night, Elaheh was an indispensable part of the HET team.

The Mishra group is a truly special place to work and I want to thank the group members past and present: Carl, Jing, Ramya, Shalini, Xiang, Jeong, Matt G., Steve, Brian, Xun, Karine, Cory, Yuuki, Davide, Silvia, Maher, Chirag, Onur and Anchal. Thanks to everyone for making me feel so welcome and for convincing me that, no matter what I tell myself, I have, in fact, become an engineer.

I would also like to thank Dirk and the rest of the Bouwmeester group, with whom I spent the first half of graduate school: Jenna, Brian, Sven, Mario, Morten and all the rest. Thanks to everyone for being so friendly and helpful and for giving me my first views of exceptional graduate-level research.

The nanofab staff runs a world-class operation in the clean room day in and day out: Tom, Brian T., Ning, Bill, Aidan, Tony, Don, Adam, Brian L. and Mike. These brave men encounter daily gas leaks, stepper alignment errors, and loose high-voltage wires with incredible patience and good humor. I have learned how special it is to have worked in a place that is equal parts renowned and fun.

Thanks to the faculty and staff of the Technology Management Program, particularly Dave Seibold. Dave has been an amazing mentor and friend and has helped smooth the ongoing transition from academia to industry. Thanks also to the physics and ECE staff members: Rob, Jennifer, Mike, Val, Alex and Shannon. These fine folks do so much invaluable behind-the-scenes work removing all the inevitable administrative roadblocks and keeping the research groups running smoothly.

I would like to thank my Santa Barbara friends for keeping me relatively sane throughout the past six years: Aaron, Matt, Andrew, Isaac, Ludo, Richard and others. A special thanks to Justin for our ritual Friday night dinners and Sunday morning Fareed Zakaria viewing parties. I will treasure those times always.

I am very lucky to have such a large and supportive family: my sisters Lindsey, Tracey, and Stephanie, and their husbands Dave, Jake and Jé. Thank you for reminding me where I come from and for keeping me grounded. An extra special thanks to my parents, Butch and Mary. I have felt your unwavering support ever since I became obsessed with building lego starships. You were steady even when I wasn't; you had confidence in me when I had none. I will never be able to describe to you what that has meant.

Finally, I want to thank Darcey for teaching me what "through thick and thin" looks like.

Curriculum Vitæ

Donald J. Suntrup III

Education

2015	Ph.D. in Physics, University of California, Santa Barbara.
2012	M.A. in Physics, University of California, Santa Barbara.
2009	B.S. in Physics, University of Texas at Austin.
2009	B.A. in English Literature, University of Texas at Austin.

Publications

"Barrier height fluctuations in InGaN polarization dipole diodes," **Donald J. Suntrup III**, Geetak Gupta, Haoran Li, Stacia Keller, Umesh K. Mishra, Applied Physics Letters, In review (2015)

"Establishment of the design space of III-N hot electron transistors for high current gain and extraction of mean free path using base thickness scaling," Geetak Gupta, Elaheh Ahmadi, **Donald J. Suntrup III**, Umesh K. Mishra, Applied Physics Letters, In review (2015)

"Measuring the signature of bias and temperature-dependent barrier heights in III-N materials using the hot electron transistor," **Donald J. Suntrup III**, Geetak Gupta, Haoran Li, Stacia Keller, Umesh K. Mishra, Semiconductor Science and Technology **30**, 105003 (2015)

"Measurement of the hot electron mean free path and the momentum relaxation rate in GaN," **Donald J. Suntrup III**, Geetak Gupta, Haoran Li, Stacia Keller, Umesh K. Mishra, Applied Physics Letters **105**, 263506 (2014)

"Design space of III-N hot electron transistors using AlGaN and InGaN polarization-dipole barriers," Geetak Gupta, Matthew Laurent, Haoran Li, **Donald J. Suntrup III**, Edwin Acuna, Stacia Keller, Umesh K. Mishra, Electronic Device Letters **36**(1), 23-25 (2014)

"In situ metalorganic chemical vapor deposition of Al_2O_3 on N-face GaN and evidence of polarity induced fixed charge," Xiang Liu, Jeonghee Kim, **Donald J. Suntrup III**, Steven Wienecke, Maher Tahhan, Ramya Yeluri, Silvia Chan, Jing Lu, Haoran Li, Stacia Keller, Umesh K. Mishra, Applied Physics Letters **104**, 263511 (2014)

"Fine tuning of micropillar cavity modes through repetitive oxidations," Morten P. Bakker, **Donald J. Suntrup III**, Henk Snyders, Tuan A. Truong, Pierre M. Petroff, Dirk Bouwmeester, Martin Van Exter, Optics Letters **38**, 17 (2013)

"Monitoring the formation of oxide apertures in micropillar cavities," Morten P. Bakker, **Donald J. Suntrup III**, Henk Snyders, Tuan A. Truong, Pierre M. Petroff, Martin Van Exter, Dirk Bouwmeester, Applied Physics Letters **102**, 101109 (2013)

"Shearing of frictional sphere packings," Jean-François Métayer, **Donald J. Suntrup III**, Charles Radin, Harry L. Swinney, and Matthias Schröter, Europhysics Letters **93**, 64003 (2011)

"Fiber-connectorized micropillar cavities," Florian Haupt, Sumant S. R. Oemrawsingh, Susanna M. Thon, Dustin Kleckner, Dapeng Ding, **Donald J. Suntrup III**, Pierre M. Petroff, and Dirk Bouwmeester, Applied Physics Letters **97**, 131113 (2010)

Honors and Awards

- Eugene Cota Robles Fellowship (UCSB Central Fellowship), 2009–2015
- Broida Fellowship, 2010–2011, 2009–2010
- Schlumberger Undergraduate Research Fellowship, 2008–2009, 2007, 2008
- College of Natural Sciences Dean's Honored Graduate (awarded to the top 1% of Natural Sciences students), 2009
- Walter E. Millet Endowed Undergraduate Scholarship, 2008
- Unrestricted Endowed Presidential Scholarship, 2008–2009
- Natural Science Book Award for Academic Distinction, 2007
- Melvin J. Reiger Scholarship, 2006, 2007
- Dr. Arnold Romberg Endowed Scholarship, 2006, 2007, 2008

Abstract

Transport Properties of III-N Hot Electron Transistors

by

Donald J. Suntrup III

Unipolar hot electron transistors (HETs) represent a tantalizing alternative to established bipolar transistor technologies. During device operation electrons are injected over a large emitter barrier into the base where they travel along the device axis with very high velocity. Upon arrival at the collector barrier, high-energy electrons pass over the barrier and contribute to collector current while low-energy electrons are quantum mechanically reflected back into the base. Designing the base with thickness equal to or less than the hot electron mean free path serves to minimize scattering events and thus enable quasi-ballistic operation. Large current gain is achieved by increasing the ratio of transmitted to reflected electrons. Although III-N HETs have undergone substantial development in recent years, there remain ample opportunities to improve key device metrics.

In order to engineer improved device performance, a deeper understanding of the operative transport physics is needed. Fortunately, the HET provides fertile ground for studying several prominent electron transport phenomena. In this thesis we present results from several studies that use the III-N HET as both emitter and analyzer of hot electron momentum states. The first provides a measurement of the hot electron mean free path and the momentum relaxation rate in GaN; the second relies on a new technique called electron injection spectroscopy to investigate the effects of barrier height inhomogeneity in the emitter. To supplement our analysis we develop a comprehensive theory of coherent electron transport that allows us to model the transfer characteristics

of complex heterojunctions. Such a model provides a theoretical touchstone with which to compare our experimental results. While these studies are of potential interest in their own right, we interpret the results with an eye toward improving next-generation device performance.

What kind of universe is it

that so runs riot?

— Chet Raymo

Contents

Chapter 1

Introduction

The hot electron transistor (HET) is a vertical, unipolar device that relies on the ballistic transport of high-energy electrons across highly scaled layers. While the concept of a ballistic HET has existed for decades, the particular challenges associated with building the device have stunted progress relative to more successful transistor technologies like the heterojunction bipolar transistor (HBT) and the high-electron-mobility transistor (HEMT). These devices have enjoyed widespread technical success and the sustained attention of device researchers. By contrast, the relatively scant development of hot electron devices has left ample room for further device improvements and for a deeper understanding of the relevant device physics.

In this opening chapter we will first introduce the hot electron transistor, discussing basic device function and relevant design parameters. Then, we will review previous efforts to build a technologically relevant HET using various materials and designs. Third, we will introduce the concept of hot electron spectroscopy and discuss the ways in which the HET can be used to study hot carrier transport in semiconductors. Fourth, we will discuss the III-N material system and highlight the ways in which the material properties of the III-Ns lend themselves to superior HET design. Finally, we will summarize and

present an outline of the work contained in this thesis.

1.1 The hot electron transistor: basic device function and design

The hot electron transistor (HET) is three-terminal device with a vertical topology (Figure 1.1). The device has of a double mesa structure with the emitter on top and the collector on the bottom. Each layer has a set of dedicated metal contacts allowing for the application of bias between layers and for the injection of current. A simple conduction band diagram along the intrinsic region of the device (pictured as the dashed line from z to z') is also shown in Fig. 1.1. The band diagram is composed of two back-to-back barriers to electron flow surrounding the base layer. The simplest way to realize this band diagram is to use three narrow bandgap materials in the base and in the emitter and collector contact regions and two wide band gap materials in the regions in between. The emitter-base and base-collector barrier heights are labeled ϕ_{EB} and ϕ_{BC}, respectively. At varying points in this thesis the barrier height (ϕ) may have units of either V or eV, depending on the context. Typically, the barrier height has units of eV when labeled on conduction band diagrams (to avoid the clutter of having to add q) and units of V when appearing in equations (to honor the traditional notation). The emitter and collector contact regions and the base are all highly n-type doped, which brings the Fermi level close to the conduction band edge. Therefore, the hole concentration is negligible throughout the device. Finally, the base thickness (t_{B}) is defined as the distance between the emitter and collector barrier maxima.

At zero bias (Fig. 1.1), the net electron flow across each junction in the device is zero. The HET is biased into active mode by applying a forward bias to the emitter

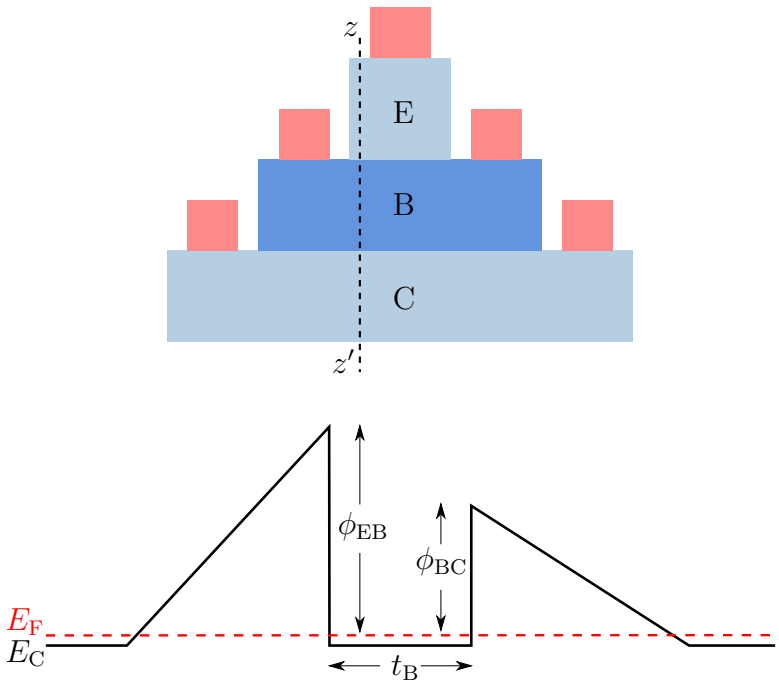

Figure 1.1: Hot electron transistor topology and conduction band diagram along the line z to z' at zero bias. The three regions corresponding to the emitter (E), base (B) and collector (C) have been labeled and the metal contacts are pictured in red. The emitter-base and base-collector barrier heights are labeled ϕ_{EB} and ϕ_{BC}, respectively, and the base thickness is labeled t_B. The Fermi level (E_F) is pictured as a dashed red line.

and a reverse bias to the collector (Fig. 1.2). This lowers the barrier on the emitter side causing electrons to be injected from the emitter into the base. Because the conduction band drops so abruptly in the base, the injected electrons instantaneously acquire a large kinetic energy in the direction perpendicular to the plane of the junction. These high-energy, "hot" electrons transit the base where they undergo scattering events that relax their longitudinal momenta. Upon arriving at the collector barrier, those electrons with kinetic energy larger than ϕ_{BC} can surmount the barrier and become collector current; electrons that have lost appreciable kinetic energy to scattering events are quantum mechanically reflected from the collector barrier. These reflected electrons continue to relax in the base, ultimately reaching the Fermi level where they contribute to base current. The HET obeys the usual current continuity condition relating the magnitudes of these three currents: $I_{\mathrm{E}} = I_{\mathrm{B}} + I_{\mathrm{C}}$.

There are several important figures of merit or performance metrics to consider when appraising transistor performance. The first, and most important, is the current gain (β) of the device. This metric represents the degree to which an output signal (I_{C}) is amplified with respect to an input signal (I_{B}): $\beta \equiv I_{\mathrm{C}}/I_{\mathrm{B}}$. Transistor amplifiers are characterized by $\beta > 1$ and, all else equal, larger β is associated with higher performance. A different, but related, performance metric is the current transfer ratio (α), defined as the fraction of the emitter current that makes it into the collector: $\alpha \equiv I_{\mathrm{C}}/I_{\mathrm{E}}$. We can use the current continuity equation to write the current gain in terms of the transfer ratio: $\beta = \frac{\alpha}{1-\alpha}$. From this relationship it is clear that a current gain of unity corresponds to the collection of half of the injected electrons ($\alpha = 0.5$).

Based on this physical description of transistor action, it is clear that β is highly dependent upon the energy difference between the hot electrons arriving at the collector and the collector barrier height. As such, we can identify several key design parameters that most strongly affect this energy difference. The first parameter is the difference

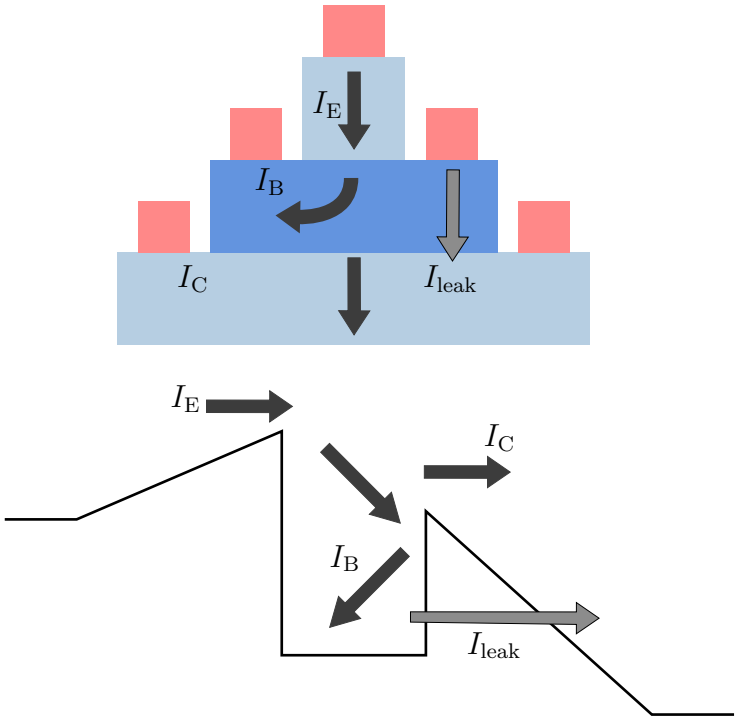

Figure 1.2: Forward active mode of hot electron transistor operation. The pathways for the emitter, base and collector currents have been labeled on the device schematic and on the conduction band diagram. The parasitic base-collector leakage current is also shown.

between emitter and collector barrier heights ($\phi_{\mathrm{EB}} - \phi_{\mathrm{BC}}$). To achieve $\beta > 1$ this difference should be large and positive, ensuring that the electrons are launched at a high energy with respect to the collector barrier. The second parameter that affects the electron arrival energy is the base thickness (t_{B}). Excessive scattering events reduce the longitudinal electron kinetic energy thereby degrading β. These scattering events can be minimized by designing the base thickness to be smaller than the hot electron mean free path: $t_{\mathrm{B}} < \lambda_{\mathrm{MFP}}$. If this condition is satisfied, the injected electrons will retain their initial kinetic energy and travel quasi-ballistically across the base.

Ballistic transport of this kind is desirable for high-frequency transistor amplifiers. Minority carrier transport in the base of a bipolar device is diffusive in nature. On a microscopic level, diffusive transport is thermally generated and, therefore, random. This means that diffusing electrons will experience many scattering events during their highly nonlinear trajectories across the base, resulting in a relatively long transit time. Ballistic electrons, by contrast, follow a straight-line trajectory through the base to the collector. The ballistic nature of electron transport in the HET promises to dramatically reduce the transit time delays that appear in bipolar devices.

In addition to transistor gain, the access resistance in the contact layers is an important metric to consider when evaluating transistor performance. Low-resistance contact regions enable the precise control of the intrinsic device by the extrinsic metal contacts. Achieving high-quality contact to the highly-scaled base layer is particularly challenging in most material systems. A trade-off typically exists between reducing the base thickness to improve current gain, and increasing the base thickness to improve access resistance. Lastly, it is important to consider the magnitude of parasitic leakage paths, particularly base-collector diode leakage (I_{leak}), which determines the breakdown voltage of the device (see Fig. 1.2). Beyond breakdown leakage currents begin to overwhelm the hot electron current in the collector and transconductance drops sharply.

The hot electrons traveling ballistically across the base are completely out of equilibrium with the host lattice. As such, these electrons have their own characteristic distribution of momenta, separate from the thermal electrons occupying the energy levels close the conduction band edge. If the hot electrons travel completely ballistically, we may assume that their momentum distribution follows that of the source electrode (i.e. a Fermi-Dirac distribution). However, even one scattering event renders the precise hot electron distribution unknowable a priori. We will discuss methods to approximately determine the scattered electron distribution later in this section. Furthermore, it is important to note that the assignment of a Fermi level or "electron temperature" to a hot electron ensemble is not always physically appropriate. Such an assignment requires a sufficient density of electrons so that electron-electron interactions occur on a time scale that is fast compared with the transit time. This condition is not necessarily satisfied for hot electrons in the base of a HET.

Having established the general design, operating principles and relevant elementary physics, we will now discuss past efforts to build a functioning HET.

1.2 The hot electron transistor: a historical perspective

The idea of the hot electron transistor (HET) was proposed over half a century ago as a potential alternative to the bipolar junction transistor (BJT). Early proponents suggested that implementation of a majority carrier device like the HET would eliminate charging delays from the minority carrier diffusion capacitance in BJTs while also increasing minority carrier mobility in the base. It was believed that these improvements would inevitably lead to unprecedented high-frequency performance. Since then, device

development has proceeded in fits and starts as researchers have struggled with the challenges inherent in building a ballistic device. While originally proposed as a potential breakthrough technology, HETs were also recognized as an effective tool to study hot electron transport in semiconductors. In this section we will briefly review the history of the HET from both a technological and a scientific perspective.

1.2.1 The HET as technology

The first hot electron transistor was developed by Mead[1] using a metal-oxide-metal-oxide-metal (MOMOM) configuration. The first metal-oxide junction served as a tunnel emitter of electrons into a thin metal base while the second junction served as the collector barrier. The thin metal base layer provided a highly conductive pathway to the intrinsic device without adding excessively to the hot electron transit length. However, it was difficult to evaporate thin metal layers without forming pinholes and the resulting current gain in these devices was $0.01 - 0.1$. Subsequent analysis suggested that the current gain of semiconductor-metal-semiconductor (SMS) HETs would be similarly low[2], owing to the difficulty of growing high-quality semiconductor crystals on thin metal films.

The idea was shelved for over a decade until Shannon proposed replacing the metal base with a degenerately doped semiconductor layer[3, 4]. This solution was designed to avoid the poor material quality of semiconductor-on-metal designs. A Schottky barrier and $n - p - n$ junction were proposed for the emitter and collector barriers, respectively. Subsequent device simulations[5] seemed to suggest that the golden age of HETs was once again upon us. A few years later, a variation of this design, which used a thin tunnel junction emitter, was proposed[6] and implemented[7, 8] in GaAs. Second-generation tunnel injector HETs in GaAs had current gain of ~ 1.3 at 40 K while InGaAs/InAlAs HETs had gain of only ~ 0.01[9]. Resonant tunnel HETs were also developed in GaAs

and had an improved current gain of ~ 10 at 77 K[10]. The relatively small band offsets characteristic of the III-As material system required the exclusive use of low-temperature measurements to avoid thermionic emission of base electrons into the collector. Because room temperature operation was prohibitively difficult to realize, GaAs HETs never found use in real technological applications and were, therefore, abandoned.

The first HETs to have current gain at room temperature were developed by Levi et al.[11, 12]. These devices contained an AlSbAs emitter, an InAs base and a GaSb collector. The emitter and collector barrier heights were 1.3 and 0.8 eV, respectively, large enough to block thermionic leakage currents at 300 K. Furthermore, the low bandgap InAs layer ensured fairly low-resistance contacts to the 10 nm base layer. All in all these devices had a room-temperature common-emitter current gain of 10. Despite the success, increasing β beyond 10 proved to be extremely difficult and, until very recently, this device represented the only room temperature HET ever demonstrated. Beyond considerations of gain, state-of-the-art HBTs outperformed the AlSbAs/InAs/GaSb HET along almost every other important device metric. HETs were, therefore, not considered to be a viable and competitive device technology at the time.

Despite these technical challenges, HETs were successfully used as a spectroscopic tool to study hot electron transport. Such an application does not require the transistor to have gain and, therefore, has the benefit of requiring less stringent performance metrics.

1.2.2 The HET as a scientific tool

Several decades ago, as device dimensions began to approach carrier scattering lengths, researchers proposed ballistic devices for both analog and digital device applications[13]. With these proposals came the desire for a deeper understanding of ballistic transport effects like velocity overshoot, which can be critically important for high-speed lat-

eral devices. Experimental techniques like photoemission spectroscopy had established themselves as reliable methods for probing hot carrier dynamics in metals[14] and in semiconductors[15, 16]. However, these methods almost always probed energy rather than momentum relaxation processes, which are most relevant for studying carrier mobility and other transport effects in electronic devices.

The idea to use the HET as a tool to study hot electron transport was first proposed by Hesto et al.[17] with the goal of unambiguously demonstrating ballistic transport across thin layers. To better understand the ways in which the HET may be used to study transport, we will briefly describe a generalized version of the hot electron spectroscopy method.

Figure 1.3 shows a simple conduction band diagram and two classes of electron ensembles (pictured in light blue): the majority carrier electrons near the band edge and the minority carrier hot electrons. The thermalized (majority carrier) electrons are responsible for carrying current between the intrinsic region (i.e. the intrinsic base and the layers immediately adjacent) and the ohmic contacts. The minority carrier hot electrons are created when thermalized electrons cross over the emitter-base barrier. Upon entering the base, these electrons gain a large amount ($\sim \phi_{\mathrm{EB}}$) of kinetic energy along the device axis resulting in a narrow distribution of highly directional longitudinal momenta. The hot electrons travel across the base with energies well above the conduction band edge. Scattering events in the base may partially relax the electron momenta causing the momentum distribution to widen. Once the electrons arrive at the collector, those with energies greater than ϕ_{BC} can cross over the barrier into the drift region of the collector, while those with energies less than ϕ_{BC} are reflected off the barrier. In this sense the collector barrier serves as a high pass filter for incoming electrons with the collector current given by

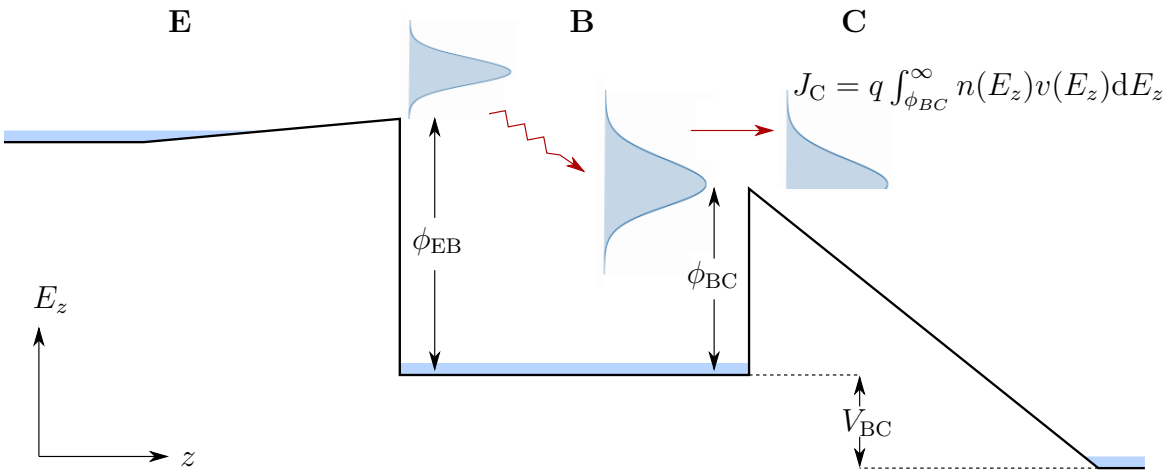

Figure 1.3: Hot electron spectroscopy using the HET. In this device ϕ_{EB} is constant while $\phi_{BC} = f(V_{BC})$.

$$J_C = q\int_{\phi_{BC}}^{\infty} n(E_z)v(E_z)dE_z, \tag{1.1}$$

where $n(E_z)$ is the distribution of electrons just to the left of the collector barrier and $v(E_z)$ is the component of their velocity perpendicular to the barrier interface. If ϕ_{BC} could be made variable, using a planar doped barrier, for example, measuring the change in J_C with collector bias (V_{BC}) can provide an estimate of the hot electron distribution function $n(E_z)$. In particular, if ϕ_{BC} varies linearly with V_{BC}, it is straightforward to show[18] that

$$\frac{dJ_C}{dV_{BC}} \propto n(E_z). \tag{1.2}$$

Equation (1.2) provides a means to extract information about the hot electron distribution $n(E_z)$ by measuring the dependence of J_C on V_{BC}. Once the barrier is biased away by applying $V_{BC} \sim \phi_{BC}$, the collector current (along with the derivative) increases rapidly due to thermally generated base-collector diode leakage. The experimental signature of quasi-ballistic transport is, therefore, a peak in the curve dJ_C/dV_{BC} vs. V_{BC} whose width is approximately equal to the width of the hot electron ensemble.

This method has been applied to GaAs HETs[19, 8] where it was used to unambigu-

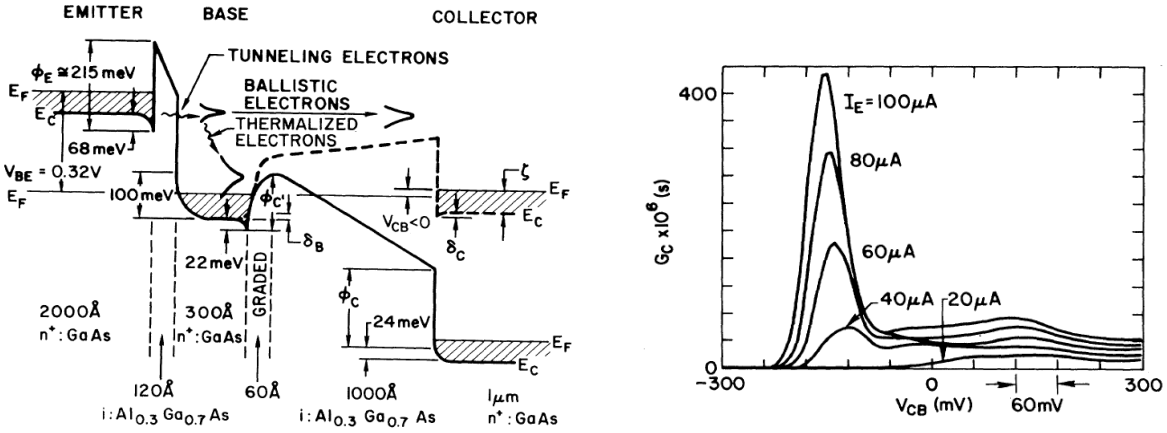

Figure 1.4: Device schematic and hot electron spectrum taken from Ref. [21]. For $V_{\mathrm{CB}} < 0$ clear peaks in $\mathrm{d}I_{\mathrm{C}}/\mathrm{d}V_{\mathrm{CB}}$ are observed. Such peaks provide very strong evidence of high-energy, quasi-ballistic transport in a GaAs HET.

ously detect ballistic electrons at cryogenic temperatures[20, 21]. A device schematic and hot electron spectrum from Ref. [21] is shown in Fig. 1.4. In this experiment electrons were tunnel injected into the base, the collector was swept from negative to positive bias, and the collector current was measured. The plot of $\mathrm{d}I_{\mathrm{C}}/\mathrm{d}V_{\mathrm{CB}}$ (or "$\mathrm{G_c}$" in the original figure) vs. V_{CB} shows clear peaks, which are energetically separated from the Fermi level. These data were used to show that roughly 50% of the injected electron ensemble traveled across the base without appreciable scattering.

In addition to simply demonstrating the presence of ballistic electrons, the HET has been used to measure the hot electron scattering rate[22] and the mean free path[23] in GaAs. In particular, it was discovered that if hot electrons were injected below the optical phonon energy in GaAs (~ 36 meV), they could travel for up to several microns before scattering[24]. These results strongly suggested that optical phonon emission is the dominant scattering mechanism for hot electrons in GaAs. Hot electron spectroscopy can also be used to estimate the optical phonon energy by varying the electron injection energy while measuring the transfer ratio. As the injection energy is scanned through

the optical phonon energy, there is a sharp increase in the carrier scattering rate causing the transfer ratio to momentarily decrease[25].

While these experiments differed in the details of their execution, they all leveraged the collector barrier as an analyzer of longitudinal momentum states and can all, therefore, be considered a form of hot electron spectroscopy. The scientific studies undertaken in this thesis will make use of the collector barrier in a conceptually similar way. In Chapters 3 and 5 we will present two different versions of electron spectroscopy to study both barrier-limited and hot carrier transport in III-N materials. Previous interpretations of electron spectroscopic data were incomplete because the detailed transfer properties of the collector barrier were neglected[25]. Our analysis will improve upon these methods by including the effects of potentially complicated transmission characteristics on the observed spectra.

In the next section we will discuss III-N material properties and their implications for HET design.

1.3 The III-N material system

The development of III-N materials has enabled dramatic technological advances in energy efficient solid state lighting and high-power switching applications. The III-Ns burst onto the technological scene with the invention of tunable, short-wavelength LEDs[26, 27] and laser diodes[28, 29] with $In_xGa_{1-x}N$ active regions. In the years since there have been impressive advances in the epitaxial growth of nitride films[30, 31, 32] as well as a deepening understanding of III-N material properties and bandstructure[33, 34, 35]. Such progress has enabled both optoelectronic devices like the ultralow threshold ultraviolet laser[36] and record-breaking high-frequency[37, 38, 39] and high-power[40] electronic devices like the high-electron-mobility transistor (HEMT). In this section we

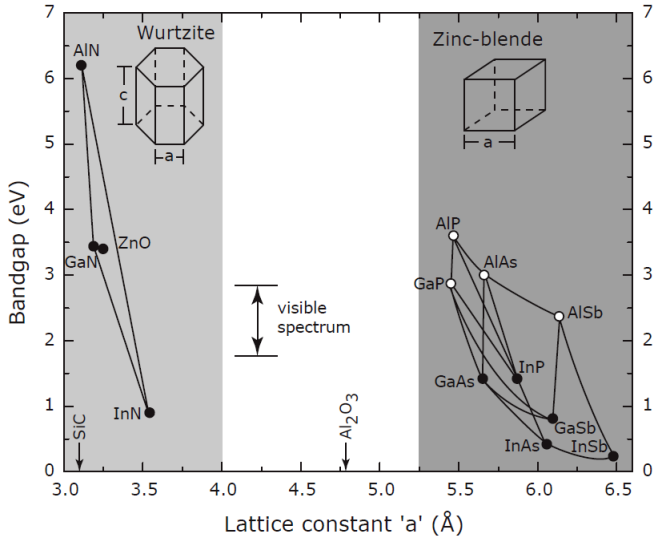

Figure 1.5: Band gaps and lattice constants for a variety of wurtzite and zincblende materials[41]. The wurtzite III-Ns span a very large range of band gaps but also have a large lattice mismatch to available substrate materials like Al_2O_3.

will review the material properties of the III-Ns, paying particular attention to those that affect hot electron transistor design.

The III-Ns (AlN, GaN, InN and their alloys) span a very large range of material band gaps (Fig. 1.5). In fact, the entire visible spectrum is theoretically accessible to the $In_xGa_{1-x}N$ alloy, making it an ideal candidate for light-emitting devices. For electronic devices, the wide range of bandgaps enables large heterojunction band offsets ($> 1\,eV$) that can be engineered to provide tunable barriers to current flow. One can imagine using such a band offset to form large emitter and collector barriers in a HET, thus enabling room temperature operation. This can immediately be identified as an advantage of III-N HETs over their III-As counterparts, which struggled to achieve barrier heights of more than a few hundred meV and, therefore, were unable to achieve room temperature transistor operation.

Gallium nitride can crystallize in either the zincblende or wurtzite structure, though the latter is more stable. The highly ionic Ga−N bond gives rise to a distribution of

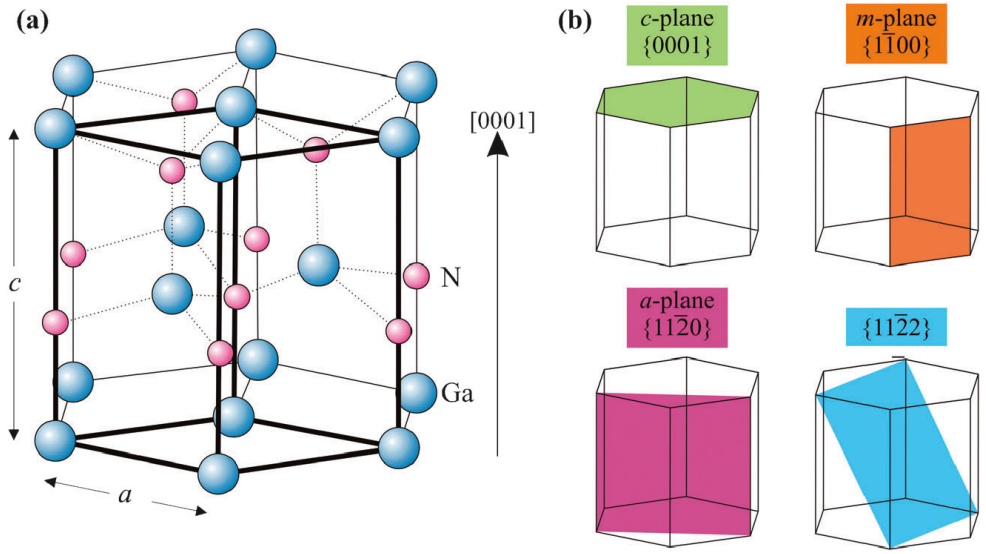

Figure 1.6: Crystal structure of wurtzite GaN. Polar c-plane growth occurs in the plane perpendicular to the [0001] direction.[43] Several nonpolar and semipolar planes are also pictured.

microscopic dipole moments oriented along the bonding axes. The symmetry properties of zincblende crystals ensure that the vector sum of these microscopic dipole moments is zero. Displacement of the constituent atoms from their equilibrium positions can, however, induce a nonzero polarization field in the zincblende crystal via the piezoelectric effect. Wurtzite crystals also contain piezoelectric polarization fields upon the application of strain. In fact, the piezoelectric coefficients in the wurtzite III-Ns are an order of magnitude larger than other III-V and II-VI compounds[42]. Additionally, the lack of inversion symmetry in the wurtzite phase gives rise to spontaneous polarization along the crystal c-axis [0001](Fig. 1.6). The resulting polarization fields can have dramatic effects on the conduction band diagram of c-plane III-N devices.

There are two polar (c-plane) crystal orientations available for growth: the plane perpendicular to the [0001] direction is called Ga-polar; the plane perpendicular to the [000$\bar{1}$] direction is called N-polar. These orientations are named for the atom that lies on the top of each hexagonal bilayer in the wurzite structure. While both Ga-polar and

N-polar orientations exhibit nonzero spontaneous polarization, the net dipole moment points in opposite directions. The nonpolar and semipolar planes pictured in Fig. 1.6 are preferred for certain optoelectronic devices where the presence of strong polarization fields is undesirable. In this thesis, however, all device structures are grown either directly on c-plane or slightly (4°) off axis.

Owing to the relative youth of III-N materials, a sufficiently large, cost-effective single-crystal substrate for nitride homoepitaxy has yet to be developed. As a result, III-N films are usually grown heteroepitaxially on lattice-mismatched substrates like Al_2O_3 (sapphire). The resulting strain accumulation leads to nonplanar growth modes, especially near the substrate interface. To separate crucial epitaxial layers from this highly defective region, thick GaN buffer layers are grown and allowed to strain relax with respect to the substrate. This method enables the subsequent growth of two-dimensional films but at the cost of introducing a high density ($10^8 - 10^{10}$ cm^{-2}) of threading dislocations into the crystal. We will briefly discuss the potential effect of dislocations on device behavior in a later chapter.

Because the GaN buffer layer is strain relaxed, thin InGaN or AlGaN epilayers grown on the buffer will be coherently strained to GaN. This introduces piezoelectric fields in the material that add to (subtract from) the spontaneous polarization field in AlGaN (InGaN) layers. The discontinuity in the polarization field at each III-N heterointerface results in a nonzero net interfacial polarization charge (Q_π). These charges produce strong dipolar electric fields that can be used to engineer barriers to electron flow. Because AlGaN/GaN and InGaN/GaN heterojunction barriers tend to have very high leakage currents, we will rely exclusively on these so-called polarization dipole barriers to form the emitter and the collector barriers in III-N HETs.

To understand how polarization engineering can be used to design electron barriers consider the structures shown in Fig. 1.7. The band diagrams of a Ga-polar

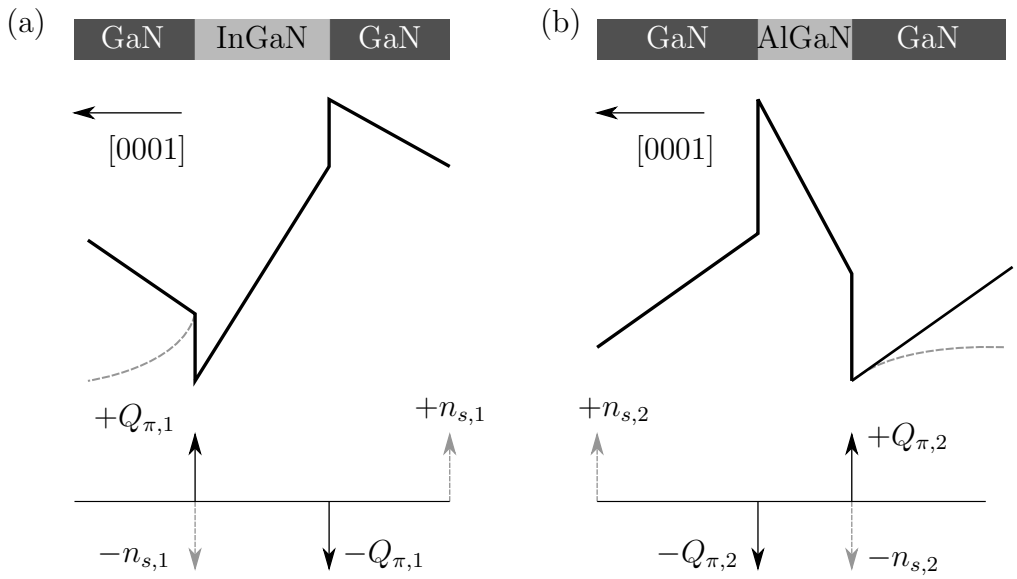

Figure 1.7: Conduction band diagram of a Ga-polar (a) InGaN and (b) AlGaN polarization dipole structure. The net polarization charge at each interface is labeled Q_π. In the absence of doping, the band diagram follows the thick black lines. Introducing dopants on either side of the dipole layer causes the $+Q_{\pi,i}$ to become screened and the bands to flatten on one side (dashed grey lines). This is the mechanism for polarization dipole barrier formation.

GaN/InGaN/GaN and a GaN/AlGaN/GaN junction are shown in Fig. 1.7(a) and (b), respectively. The interface charges that results from the polarization discontinuity are labeled $Q_{\pi,i}$. For a material with no free electrons, the $Q_{\pi,i}$ are the only charges in the vicinity of the dipole layer and the band diagram resembles the solid black lines in Fig. 1.7. In this case the bands on the $+Q_{\pi}$ side will continue to rise and a barrier cannot form. However, if shallow n-type dopants are added near, but not directly adjacent to, the dipole region, mobile electrons from the donor atoms will be attracted to the $+Q_{\pi,i}$ charge. The resulting accumulation of electrons screens the $+Q_{\pi,i}$ and flattens the bands on one side (dashed grey lines). Thus an asymmetric barrier to electron flow is formed. It is important that on the $-Q_{\pi,i}$ side the dopants be placed sufficiently far from the dipole layer so as not to cause excessive band bending, which reduces the asymmetry of the barrier. Also, recall that the above arguments apply to Ga-polar heterojunctions. For N-polar structures, the signs of the net interfacial polarization charges will all be reversed causing the bands in Fig. 1.7 to be reflected about the vertical axis.

The free electrons that accumulate at an Al(In)GaN/GaN interface are confined to a small longitudinal dimension (1−2 nm) and can thus be considered to be a two-dimensional electron gas (2DEG). For AlGaN/GaN junctions with sufficiently high Al content or AlGaN thickness, 2DEG densities can approach $2 \times 10^{13}\,\mathrm{cm}^{-2}$. The high charge density renders the AlGaN/GaN 2DEG uniquely suited to carrying current in highly scaled layers like the base of the HET. The use of the 2DEG to provide base charge represents a key improvement over past designs, which relied on bulk doping the base layer to get charge. In these structures scaling the base necessarily led to a reduction in base charge and, therefore, higher base resistance. By contrast, the base layer in a III-N HET can be scaled to < 3 nm without significantly degrading the 2DEG charge density. Therefore, we will make use of an AlGaN/GaN junction as the emitter in Ga-polar HETs and as the collector in N-polar HETs.

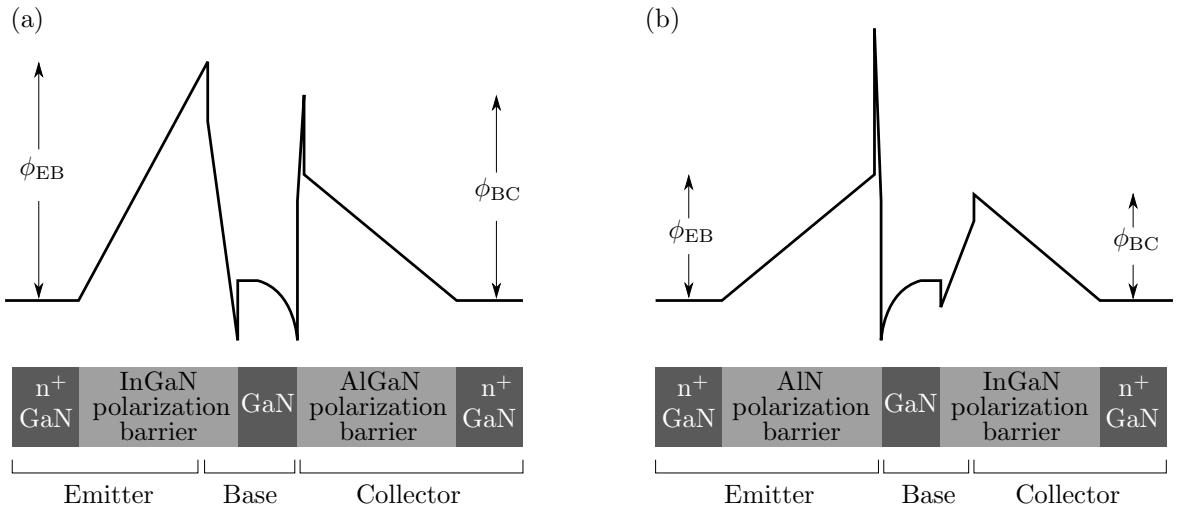

Figure 1.8: (a) N-polar and (b) Ga-polar HET designs and conduction band diagrams.

The InGaN polarization dipole also accumulates electrons on the highly doped side of the junction. Therefore, using the InGaN polarization barrier as the collector (emitter) in Ga-polar (N-polar) HETs adds additional charge to the base and further reduces the base resistance. The design structures and conduction band diagrams for both the Ga-polar and N-polar HET are shown in Fig. 1.8. The electric field in the dipole layers can reach $\sim$10 MV/cm allowing for the design of large $(0.75-1.5$ eV) emitter and collector barriers using the polarization dipole method. These large barriers enable the injection of very high-energy electrons while simultaneously enabling room temperature HET operation. In each of the designs pictured in Fig. 1.8, the compositions and thicknesses of the dipole layers are chosen to ensure that $\phi_{EB} > \phi_{BC}$ whenever possible.

1.4 Outline of the thesis

As the title suggests, the goal of this thesis is to better understand the transport physics of the III-N HETs pictured in Fig. 1.8 with the goal of ultimately improving device performance. Broadly speaking, there are two main areas on which we will focus

our attention: first, we would like to understand electron transport in the vicinity of the barrier regions. In the HET there are two barriers, the emitter and the collector, and we will describe the transport properties of both. An important distinction to make is that the source electrons incident on the emitter barrier are thermally generated while those incident on the collector are hot electrons from the base. Second, we would like to understand quasi-ballistic electron transport across the highly-scaled base layer. In this case there are no major barriers to electron flow and hot electron scattering processes become the main focus. Chapters 2−4 will cover barrier-limited transport phenomena while Chapter 5 will deal with quasi-ballistic base transport. Throughout our discussions we will point out the implications of our findings for transistor performance before summarizing and proposing several follow-up experiments in Chapter 6. Below we provide a more detailed outline.

In Chapter 2, we will present a theory of electron transmission through an arbitrary potential barrier. We will compare the three most popular methods for calculating the transmission probability before choosing the method most suited to our needs. The ability to determine the transmission characteristics of an arbitrary barrier will allow us to simulate the behavior of a hot electron wavepacket arriving at the collector barrier in a HET. This will help us to better understand experimental transistor data presented in later chapters. Then, we will use the barrier transmission characteristics to derive an expression for diode current density as a function of voltage and temperature. This expression will improve upon the canonical thermionic emission formula by including the effects of thermionic field emission on the diode current. The simulated diode characteristics can then be compared with experimental results presented in later chapters to help determine the physical causes of diode nonidealties. We will conclude Chapter 2 by presenting the theory of barrier height inhomogeneity and providing a sample analysis of a GaN Schottky diode.

Chapter 3 will begin with a presentation of the III-N Nitrogen-polar HET design. Then, we will analyze the common-emitter current characteristics of the first-generation N-polar HET and discuss major device advantages and deficiencies. Next, we will discuss the nonideal transport characteristics of the InGaN polarization dipole emitter diode in light of barrier height inhomogeneity theory. Such an analysis will allow us to extract quantitative information about the magnitude of lateral barrier height fluctuations and to propose a physical cause. Finally, we will present the HET as a tool to study emitter barrier transport by using the collector as an analyzer of emitted electron momentum states. Temperature-dependent HET measurements will be shown to corroborate the conclusions drawn from the emitter diode analysis.

In Chapter 4 we will present the III-N Ga-polar HET design and discuss its advantages over N-polar HETs. Then, we will present the common emitter current characteristics of a hybrid MOCVD/MBE HET device before moving on to discuss AlN emitter diode transport. We will apply an abbreviated version of the methods used in Chapter 3 to briefly analyze the emitter current characteristics before discussing the implications of the results for device operation.

In Chapter 5, we will discuss transport characteristics of hot electrons in the base of the HET. We will review possible electron scattering mechanisms in wurtzite GaN and determine which processes are most relevant for the hot electrons in our devices. Then we will present a method to measure the hot electron mean free path and momentum relaxation rate using the hot electron transistor before analyzing the extracted relaxation rates and discussing the implications for device performance. Finally, in Chapter 6 we will summarize our conclusions and propose a road map for future work.

Chapter 2

Coherent transport theory

Nearly all modern semiconductor devices make use of heterojunctions. Along with classical electric fields arising from space charge regions, for example, heterojunctions provide a means to precisely control the flow of charged carriers on extremely short time scales. Simply stated, a heterojunction is a plane in a crystal where the proportion of constituent elements changes, often abruptly. This change in crystal composition results in a spatially varying density of states that modulates the free carrier wavefunction in the direction perpendicular to the heterointerface. In order to understand heterojunction diode characteristics we must first understand the nature of the electron wavefunction in these regions.

Our treatment in this chapter will proceed by first discussing the coherent dynamics of conduction band electrons near a heterointerface. In particular, we will outline three different methods to calculate the transmission probability in these regions, discussing the merits and limitations of each method. Crucially, we will neglect electron-electron interactions so that each momentum eigenstate can be considered independently. This assumption allows us to use statistical considerations to calculate the total device current by performing a weighted sum of the current carried by each momentum eigen-

state. Coupled with a proprietary Schrödinger-Poisson solver that generates the device band diagram, this method enables a complete numerical simulation of current-voltage-temperature characteristics for arbitrary junctions. Such a simulation provides a theoretical standard with which to compare the experimental data presented in later chapters. Furthermore, simulating the transmission characteristics of an arbitrary collector barrier enables a theoretical estimate of the current transfer ratio in a HET.

Once we have derived an equation describing ideal diode transport, we will introduce the concept of barrier height inhomogeneity (BHI) and discuss its effects on transport properties.

2.1 The transmission coefficient

The problem of determining the motion of conduction band electrons in solid state systems has preoccupied scientists for over a century. The most rigorous treatment of this problem involves solving the many-body Schrödinger equation, but this turns out to be computationally prohibitive particularly on length scales that are relevant for macroscale devices. One the other hand, the maturation of growth techniques like molecular beam epitaxy (MBE) and metal-organic-chemical-vapor deposition (MOCVD) has enabled the aggressive scaling of device dimensions over the past several decades. The ability to grow semiconductor films composed of 1-10 monolayers has precluded the option to ignore quantum interference effects all together in favor of an entirely semi-classical treatment. Therefore, the intermediate length scales present in modern devices necessitate an approximate, yet still explicitly quantum mechanical, treatment of carrier transport.

In lieu of exact solutions, computationally tractable approaches like density functional theory (DFT)[44, 34] and Monte-Carlo[45, 46] simulations have become popular tools

for studying band structure and transport. These methods, however, usually require complicated numerics and sizable computational power. Here, we will use an alternative approach based on the effective mass theorem and the envelope function description [47]. While this will simplify the problem dramatically, it will also restrict the applicability of the theory to high symmetry points in the Brillouin zone. Furthermore, our model will ignore the effects of inelastic scattering, which requires a higher level treatment.

According to Bloch's theorem, the wavefunction near, say, the Γ valley minimum has the form

$$\Psi(\vec{r}) = \psi(\vec{r})u_{k=0}(\vec{r}), \tag{2.1}$$

where $u(\vec{r})$ is periodic in the material lattice constant and $\psi(\vec{r})$ is a slowly varying envelope function. The central assumption of the envelope description is that the periodic components $u(\vec{r})$ are nearly identical in every region of a heterostructure. This, in turn, requires that all materials be latticed matched in the plane of a heterointerface [48]. Crucially, this condition is satisfied both for lattice matched junctions like AlGaAs/GaAs as well as for coherently strained materials like the III-Ns. Making this assumption allows us to factor out the atomic-scale oscillations represented by $u(\vec{r})$ from the dynamical equations. What remains is the one-dimensional Schrödinger equation for the envelope functions:

$$-\frac{\hbar^2}{2}\frac{\partial}{\partial z}\frac{1}{m^*(z)}\frac{\partial}{\partial z}\psi(z) + E_{\mathrm{C}}(z)\psi(z) = E\psi(z), \tag{2.2}$$

where $\hat{z}$ is the direction perpendicular to the interface, E_{C} is the position-dependent conduction band minimum, E is the total energy, m^* is the position-dependent effective mass, and $\hbar$ is the reduced Planck's constant. All atomic-scale effects are implicitly contained in the effective mass and in the dispersion relation $E(\vec{k})$. It is important to note that m^* is an explicitly bulk property and that the very concept of effective mass is not well-defined in the vicinity of a heterojunction or within a thin layer. Nevertheless, we

will adopt the assumption that local electron properties, even in the vicinity of boundary layers, resemble the material properties of the bulk. While this assumption is useful from a mathematical perspective, the physical meaning of effective mass in these regions is unclear.

Our goal will be to determine, for an arbitrary potential barrier and a given initial electron momentum k_i, the ratio of the transmitted to the incident current density. In all cases considered in this chapter, we will assume that the barrier in question is surrounded by electron reservoirs that emit a thermal distribution of electron momenta toward the barrier. In practice these reservoirs are composed of highly doped semiconductor layers with ohmic metal contacts. Device bias will be reflected in different electrochemical potentials (or Fermi levels) in the reservoirs. Because the free carrier concentration is very high in the reservoirs, the conduction band is flat and the incoming and outgoing electrons can be considered to be plane waves:

$$\begin{aligned} \psi_i &= A_i e^{ik_i z} + B_i e^{-ik_i z}, \\ \psi_f &= A_f e^{ik_f z}, \end{aligned} \tag{2.3}$$

where $k_{i,f} = \sqrt{2m^*_{i,f}(E - E_{Ci,f})}/\hbar$. We have stipulated here that carriers are incident only from the left. Furthermore, each wavefunction has an associated probability current density given by

$$J = \frac{\hbar}{2m^* i}\left(\psi^* \frac{\partial \psi}{\partial z} - \psi \frac{\partial \psi^*}{\partial z}\right). \tag{2.4}$$

The transmission probability is then the ratio of incident to transmitted probability current density. Combining Eqs. (2.3) and (2.4) for incoming and outgoing waves and taking the ratio gives

$$\widetilde{T} = \frac{J_f}{J_i} = \frac{|A_f|^2}{|A_i|^2}\frac{v_f}{v_i}, \tag{2.5}$$

where v_i and v_f are the initial and final electron velocities, respectively.

In the following sections, we will discuss three methods to calculate the transmission probability and compare their ability to describe relevant heterostructures.

2.1.1 The WKB approximation

The most commonly used method to estimate the transmission probability of charged carriers in the vicinity of one-dimensional potential barriers is based on the Wentzel-Kramers-Brillouin (WKB) approximation[49, 50, 51]. This method is popular for device simulations because of its analytical simplicity and ease of use. In this section we will briefly outline the WKB method and highlight both its abilities and limitations.

As a starting point, the simplest form of the one-dimensional Schrödinger equation is

$$-\frac{\hbar^2}{2m^*}\frac{\partial^2}{\partial z^2}\psi(z) + E_{\mathrm{C}}(z)\psi(z) = E\psi(z). \tag{2.6}$$

This is a second order differential equation for the wavefunction ψ and is not analytical except in a very few special cases. One such case is that of a constant potential (i.e. $E_{\mathrm{C}}(z) = E_{\mathrm{C}}^0$), which has oscillatory, plane wave solutions:

$$\psi(z) = Ae^{\pm ikz},\ k \equiv \sqrt{2m^*(E - E_{\mathrm{C}}^0)}/\hbar, \tag{2.7}$$

where A is a complex constant and the deBroglie wavelength associated with ψ is $\lambda = 2\pi/k$. While this a tidy and simple solution, it describes an extremely limited, and not very interesting, subset of problems. The scope of this solution widens if the assumption is made that the potential, while not strictly constant, varies slowly compared with the deBroglie wavelength. This means that from the prospective of a traveling charge at any given moment, the potential "looks" locally constant. The physical situations that most

accurately satisfy this approximation are high energy carriers (i.e. small λ) and smoothly and slowly varying potentials. Intuitively we might expect that if the potential varies slowly enough, the wavefunction could remain oscillatory while the amplitude (A) and phase ($k(z)z$) vary gradually. This picture of a wavefunction that gradually adapts to changes in potential inspired an alternate name for WKB: the adiabatic approximation.

Solving the Schrödinger equation (2.6) with this updated form of the wavefunction yields[52]:

$$\psi(z) \sim \frac{C}{\sqrt{2m^*(E - E_{\mathrm{C}}(z))}} e^{\pm \frac{i}{\hbar} \int \sqrt{2m^*(E - E_{\mathrm{C}}(z))} \mathrm{d}z}, \tag{2.8}$$

where C is another complex constant. This solution implies that for a slowly varying potential barrier between z_i and z_f, the transmission probability at energy E is given by:

$$\widetilde{T}(E) \simeq \exp\left(\frac{-2}{\hbar} \int_{z_i}^{z_f} \sqrt{2m^*(E_{\mathrm{C}}(z) - E)} \mathrm{d}z \right). \tag{2.9}$$

For arbitrary barriers the integral in Eq. (2.9) can be evaluated numerically for $E < E_{\mathrm{C,max}}$ ($\widetilde{T}(E) = 1$ for $E > E_{\mathrm{C,max}}$)[53]. The WKB approximation breaks down at the so-called classical turning points where $E \simeq E_{\mathrm{C}}$ and care must be taken so that the wavefunction does not diverge to infinity in these regions. This issue is particularly problematic when trying to adapt the WKB treatment to bound state calculations. However, even for unbound, current-carrying states, the WKB method becomes less accurate at higher energies when the tunneling probability become appreciable.

Equation (2.9) also does not account for wavefunction interference effects arising from reflections at multiple material boundaries. Such interference effects are most pronounced when the barrier width is on the order of the deBroglie wavelength as is the case in III-N polarization dipole layers, for example. Historically as semiconductor device structures were scaled to dimensions comparable to the electron deBroglie wavelength, it became clear that conventional analytical approaches based on the WKB approximation were no

longer valid[54]. A more rigorous, numerical solution was needed.

2.1.2 The transfer matrix method

The following approach for solving for the transmission characteristics of arbitrary potential barriers arose out of a desire to model tunnel currents in multiquantum well structures[55, 56, 57]. The approach, known as the transfer matrix method (TMM), involves breaking the potential into segments in which the exact solution to the Schrödinger equation is known. Enforcing continuity of the wavefunction and its spatial derivative at each boundary leads to a 2×2 matrix for each interface. Multiplying these matrices together yields a direct relationship between incoming and outgoing wave components.

The Schrödinger equation is directly solvable for a constant or for a linearly varying potential segment and indeed these are the two most widely used segment shapes[58, 59, 60]. The potential barriers formed by III-N polarization dipoles lend themselves well to linear potential segments and this is the approach we will take in this section.

Consider the stepwise linear potential pictured in Fig. 2.1. In any one of the labeled segments, the one-dimensional, the time-independent Schrödinger equation reads

$$\frac{\partial^2 \psi}{\partial z^2} + \frac{2m^*}{\hbar^2} \left(E - E_{\mathrm{C}}(z) \right) \psi = 0, \tag{2.10}$$

where within any segment $[z_i, z_{i+1}]$, the conduction band minimum is linear:

$$E_{\mathrm{C}}(z) = E_{\mathrm{C}}(z_i) + \frac{E_{\mathrm{C}}(z_{i+1}) - E_{\mathrm{C}}(z_i)}{z_{i+1} - z_i}(z - z_i). \tag{2.11}$$

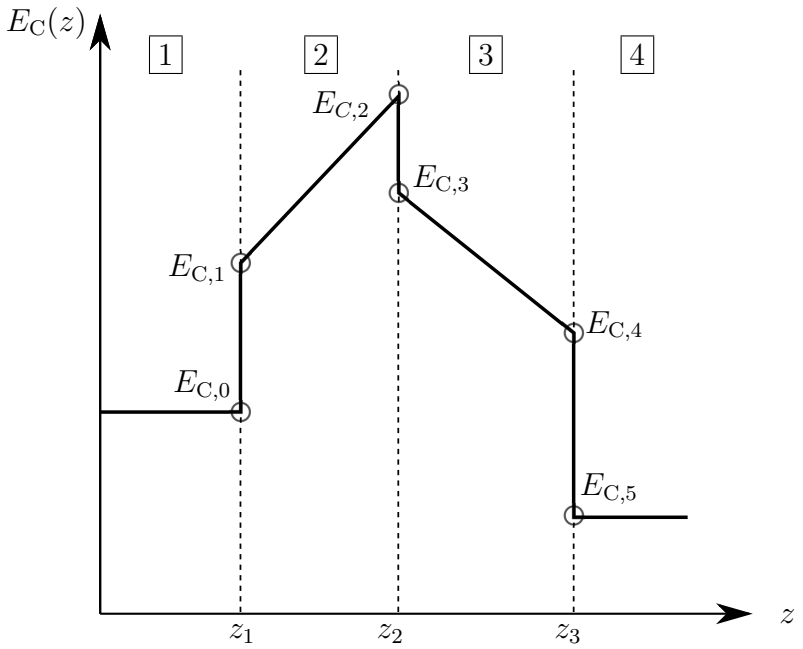

Figure 2.1: Piecewise linear potential used to derive the transmission coefficient via the transfer matrix method. The boxed numbers indicate potential segments and the $E_{\mathrm{C},i}$ represent values of the conduction band edge at various points.

If we define two constants for each linear region:

$$\alpha_i \equiv -\left(\frac{\hbar^2}{2m_i^*}\frac{z_{i+1}-z_i}{E_{\mathrm{C}}(z_{i+1})-E_{\mathrm{C}}(z_i)}\right)^{1/3},$$
$$\beta_i \equiv -\left(\frac{2m_i^*}{\hbar^2}\right)^{1/3}\left(\frac{z_{i+1}-z_i}{E_{\mathrm{C}}(z_{i+1})-E_{\mathrm{C}}(z_i)}\right)^{2/3}\left(E-E_{\mathrm{C}}(z_i)+z_i\frac{E_{\mathrm{C}}(z_{i+1})-E_{\mathrm{C}}(z_i)}{z_{i+1}-z_i}\right), \tag{2.12}$$

and make the substitution $u_i(z) \equiv \beta_i - z/\alpha_i$ we find that the wavefunction in region i evolves according to

$$\frac{\mathrm{d}^2\psi_i}{\mathrm{d}u^2} - u_i(z)\psi_i = 0. \tag{2.13}$$

This is the Airy equation whose solutions are the well-known Airy functions:

$$\psi_i(z) = A_i\mathrm{Ai}(u_i(z)) + B_i\mathrm{Bi}(u_i(z)), \tag{2.14}$$

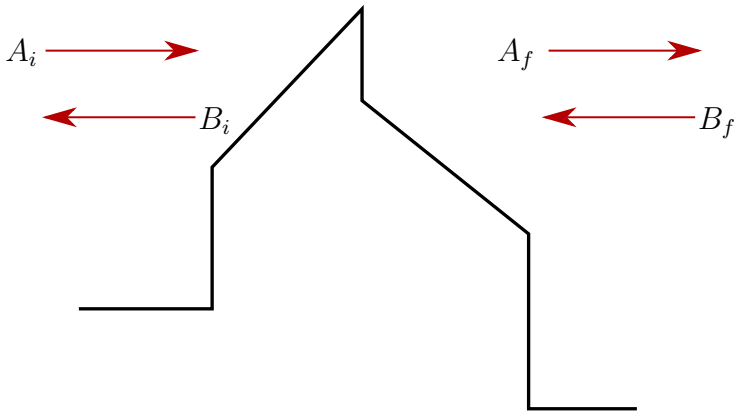

Figure 2.2: Schematic of the incoming and outgoing plane waves in the TMM method. For the example in the text, $i = 1$ and $f = 4$.

where A_i and B_i are complex constants.

We can derive transfer matrices at each boundary by writing the wavefunction in each region and enforcing continuity of ψ and $(1/m^*)\partial\psi/\partial z$. Note that these two conditions are implied by the continuity of probability flux as defined in Eq. (2.4). In the example pictured in Fig. 2.1, the wavefunctions in each region are:

$$\begin{aligned}
\psi_1(z) &= A_1 e^{ik_1 z} + B_1 e^{-ik_1 z}, \\
\psi_2(z) &= A_2 \mathrm{Ai}(u_2(z)) + B_2 \mathrm{Bi}(u_2(z)), \\
\psi_3(z) &= A_3 \mathrm{Ai}(u_3(z)) + B_3 \mathrm{Bi}(u_3(z)), \\
\psi_4(z) &= A_4 e^{ik_4 z} + B_4 e^{-ik_4 z},
\end{aligned} \tag{2.15}$$

where $k_1 = \sqrt{2m_1^*(E - E_{\mathrm{C},0})}/\hbar$, $k_4 = \sqrt{2m_4^*(E - E_{\mathrm{C},5})}/\hbar$, and

$$\begin{aligned}
u_i(z) &= -\left(\frac{2m_i^*}{\hbar^2}\right)^{1/3} \left(\frac{z_{i+1} - z_i}{E_{\mathrm{C}}(z_{i+1}) - E_{\mathrm{C}}(z_i)}\right)^{2/3} \left(E - E_{\mathrm{C}}(z)\right), \\
u_i'(z) &= \frac{\mathrm{d}u_i(z)}{\mathrm{d}z} = \left(\frac{2m_i^*}{\hbar^2}\right)^{1/3} \left(\frac{E_{\mathrm{C}}(z_{i+1}) - E_{\mathrm{C}}(z_i)}{z_{i+1} - z_i}\right)^{1/3}.
\end{aligned} \tag{2.16}$$

Our goal is to determine the propagation matrix ($\hat{P}$) connecting the wave components

on the left side of the barrier with those on the right (see Fig. 2.2):

$$\begin{pmatrix} A_i \\ B_i \end{pmatrix} = \hat{P} \begin{pmatrix} A_f \\ B_f \end{pmatrix} = \begin{pmatrix} P_{11} & P_{12} \\ P_{21} & P_{22} \end{pmatrix} \begin{pmatrix} A_f \\ B_f \end{pmatrix}. \tag{2.17}$$

To this end we treat each region of Fig. 2.1 separately and recognize that

$$\hat{P} = \prod_{i}^{n} \hat{P}_i, \tag{2.18}$$

where n is the number of boundaries between potential segments. Note that the order of matrix multiplication is such that the matrix index increases from left to right.

We impose the condition that our initial and final rightward traveling wavefunctions are plane waves with wave vectors k_i and k_f, respectively. Equations (2.5) and (2.17) together imply

$$\widetilde{T} = \frac{|A_f|^2}{|A_i|^2} \frac{v_f}{v_i} = \frac{1}{|P_{11}|^2} \frac{v_f}{v_i}. \tag{2.19}$$

The problem is then reduced to finding the propagation matrix for each potential region, multiplying them together, and taking the ratio given by Eq. (2.19).

To derive the exact form of the $\hat{P}_i$ in Eq. (2.18), we write the explicit forms of ψ and $(1/m^*)\partial\psi/\partial z$ immediately to the left and right of each boundary and equate them. These boundary conditions imply the following propagation matrix for an electron crossing the plane at z_1 in Fig. 2.1:

$$\hat{P}_1 = \frac{1}{2} \begin{pmatrix} e^{-ik_1 z_1} \left(\mathrm{Ai}(u_2) + \gamma_1 \mathrm{Ai}'(u_2) \right) & e^{-ik_1 z_1} \left(\mathrm{Bi}(u_2) + \gamma_1 \mathrm{Bi}'(u_2) \right) \\ e^{ik_1 z_1} \left(\mathrm{Ai}(u_2) - \gamma_1 \mathrm{Ai}'(u_2) \right) & e^{ik_1 z_1} \left(\mathrm{Bi}(u_2) - \gamma_1 \mathrm{Bi}'(u_2) \right) \end{pmatrix}, \tag{2.20}$$

where $\gamma_1 = \frac{u_2'}{ik_1} \frac{m_1^*}{m_2^*}$, and all functions and their derivatives are evaluated at z_1. This matrix applies generally for an electron crossing a plane from a flat to a sloping band.

For the plane at z_2, the propagation matrix is found to be

$$\hat{P}_2 = \pi \begin{pmatrix} \mathrm{Ai}(u_3)\mathrm{Bi}^{'}(u_2) - \gamma_2 \mathrm{Ai}^{'}(u_3)\mathrm{Bi}(u_2) & \mathrm{Bi}(u_3)\mathrm{Bi}^{'}(u_2) - \gamma_2 \mathrm{Bi}^{'}(u_3)\mathrm{Bi}(u_2) \\ -\mathrm{Ai}(u_3)\mathrm{Ai}^{'}(u_2) + \gamma_2 \mathrm{Ai}^{'}(u_3)\mathrm{Ai}(u_2) & -\mathrm{Bi}(u_3)\mathrm{Ai}^{'}(u_2) + \gamma_2 \mathrm{Bi}^{'}(u_3)\mathrm{Ai}(u_2) \end{pmatrix}, \tag{2.21}$$

where $\gamma_2 = \frac{u_3^{'}}{u_2^{'}} \frac{m_2^*}{m_3^*}$, and all functions and their derivatives are evaluated at z_2. Here, we have made use of the property that $\mathrm{Ai}(u_i)\mathrm{Bi}^{'}(u_i) - \mathrm{Bi}(u_i)\mathrm{Ai}^{'}(u_i) = \pi^{-1}$. The form of this matrix applies to any electron crossing a plane between sections with two different, nonzero slopes.

Finally, for the plane at z_3, the propagation matrix is

$$\hat{P}_3 = \pi \begin{pmatrix} e^{ik_4 z_3}\left(\mathrm{Bi}^{'}(u_3) - \gamma_3 \mathrm{Bi}(u_3)\right) & e^{-ik_4 z_3}\left(\mathrm{Bi}^{'}(u_3) + \gamma_3 \mathrm{Bi}(u_3)\right) \\ e^{ik_4 z_3}\left(-\mathrm{Ai}^{'}(u_3) + \gamma_3 \mathrm{Ai}(u_3)\right) & e^{-ik_4 z_3}\left(-\mathrm{Ai}^{'}(u_3) - \gamma_3 \mathrm{Ai}(u_3)\right) \end{pmatrix}, \tag{2.22}$$

where $\gamma_3 = \frac{m_4^*}{m_3^*} \frac{ik_4}{u_3^{'}}$, and all functions and their derivatives are evaluated at z_3. This matrix applies for an electron crossing a plane from a sloping band to a flat band. With these three matrices describing all possible boundaries, we are able to construct a propagation matrix for any arbitrary barrier according to Eq. (2.18).

While this method has accurately described the transport of free electrons near barrier regions, its application to quasi-bound state transport has resulted in numerical instabilities, especially for thick barriers. Furthermore, the evaluation of the Airy functions in the case of nearly flat bands tends to produce singularities[61]. A more widely applicable method, one that can accurately describe both flat and sloping bands and remains numerical stable for thick barriers, is described in the next section.

2.1.3 The quantum transmitting boundary method

The quantum transmitting boundary method (QTBM) was initially proposed by Lent[62] to address the problem of coherent electron transport in two-dimensional systems. The method we will outline here is a simplified, one-dimensional version of this method developed primarily by Frensley[63, 64]. This method differs from the transfer matrix method in several important ways: first, the conduction band diagram produced from the Schrödinger-Poisson solver is directly used (i.e. no fitting of line segments is necessary). Secondly, rather than assuming an analytical form for the wavefunction and solving piecewise for the coefficients, the entire wavefunction is solved for directly. Thirdly, and most importantly, the QTBM is not prone to the numerical overflow issues that can restrict the applicability of the transfer matrix method.

For a system with position-dependent effective mass, the simplest Hermitian form of time-independent, 1-D Schrödinger equation is

$$-\frac{\hbar^2}{2}\frac{\partial}{\partial z}\frac{1}{m^*(z)}\frac{\partial}{\partial z}\psi(z) + E_{\mathrm{C}}(z)\psi(z) = E\psi(z). \tag{2.23}$$

The QTBM relies on finite difference methods to transform Eq. (2.23) from a differential operator equation on continuous variables to a matrix equation with a finite number of elements. To this end we define a mesh size Δ such that any position can be written as an integer multiple of the mesh: $z_j = j\Delta$. Furthermore, we will insist that the effective mass, the potential and the wavefunction be defined only on mesh points with the following

notation:

$$\begin{aligned} m^*(z_j) &\equiv m_j^*, \\ \psi(z_j) &\equiv \psi_j, \\ E_{\mathrm{C}}(z_j) &\equiv E_{\mathrm{C},j}. \end{aligned} \tag{2.24}$$

To discretize the kinetic energy operator in equation Eq. (2.23) we will assume that Δ is small enough that both $m^*(z)$ and $\psi(z)$ vary linearly between mesh points. The latter assumption allows us to make use of the two-point, central difference approximation to the first derivative[65]:

$$\left.\frac{\partial}{\partial z}\psi(z)\right|_{z=z_j} \simeq \frac{\psi(z_j+\frac{\Delta}{2})-\psi(z_j-\frac{\Delta}{2})}{\Delta} = \frac{\psi_{j+\frac{1}{2}}-\psi_{j-\frac{1}{2}}}{\Delta}, \tag{2.25}$$

where we have made use of the property that $z_j \pm \Delta/2 = z_{j\pm\frac{1}{2}}$. We can use this same approximation to write:

$$\begin{aligned} -\frac{\hbar^2}{2}\frac{\partial}{\partial z}\frac{1}{m_z^*}\left.\frac{\partial}{\partial z}\psi(z)\right|_{z=z_j} &= -\frac{\hbar^2}{2\Delta}\left(\left.\frac{1}{m^*}\frac{\partial\psi}{\partial z}\right|_{j+1/2} - \left.\frac{1}{m^*}\frac{\partial\psi}{\partial z}\right|_{j-1/2}\right) \\ &= -\frac{\hbar^2}{2\Delta}\left(\frac{1}{m^*_{j+1/2}}\frac{\psi_{j+1}-\psi_j}{\Delta} - \frac{1}{m^*_{j-1/2}}\frac{\psi_j-\psi_{j-1}}{\Delta}\right). \end{aligned} \tag{2.26}$$

Now we use the piecewise linearity of m^* to write $m^*_{j\pm1/2} = \frac{1}{2}(m_j^* + m_{j\pm1}^*)$ so that Eq. (2.23) is transformed to[66]:

$$H\psi_j = -s_j\psi_{j-1} + d_j\psi_j - s_{j+1}\psi_{j+1} = E\psi_j, \tag{2.27}$$

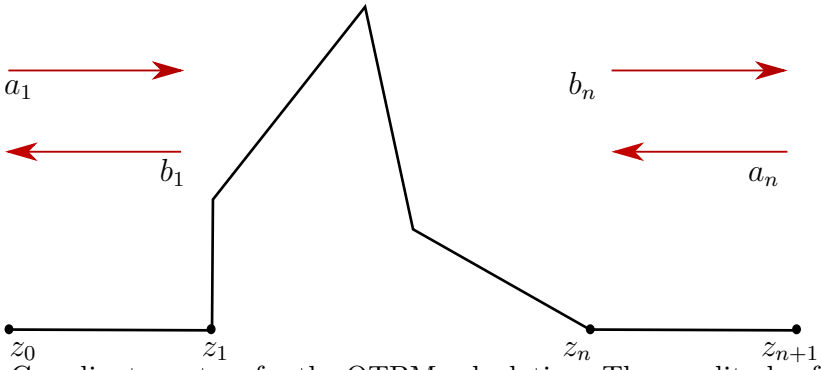

Figure 2.3: Coordinate system for the QTBM calculation. The amplitude of incoming and outgoing plane waves are labeled a and b, respectively.

where

$$s_j = \frac{\hbar^2}{\Delta^2}\left(\frac{1}{m^*_{j-1}+m^*_j}\right),$$
$$d_j = \frac{\hbar^2}{\Delta^2}\left(\frac{1}{m^*_{j+1}+m^*_j}+\frac{1}{m^*_{j-1}+m^*_j}\right)+E_{\mathrm{C},j}. \tag{2.28}$$

Note that the assumptions of piecewise linearity for both m^* and ψ ensure that the usual continuity requirements for ψ and $(1/m^*)\partial\psi/\partial z$ are satisfied everywhere, including across potential discontinuities. Therefore, the boundary conditions at such a discontinuity are automatically satisfied and need not be separately imposed.

Equation (2.27) represents a set of linear equations for ψ. For a closed (or isolated) system, the tridiagonal matrix can be immediately diagonalized to yield the eigenvalues. To achieve a complete description of an open system, where the barrier region is connected to two large electron reservoirs (i.e. ohmic contacts), Eq. (2.27) must be supplemented with appropriate boundary conditions.

To this end we will assume that the contact regions emit plane wave electrons into the barrier region. The coordinate system for this situation is pictured in Fig. 2.3. In the regions $j \leq 1$ and $j \geq n$ the potential is constant and the wavefunctions are given

by:

$$\psi(z_j) = \begin{cases} a_1 e^{ik_1(z_j - z_1)} + b_1 e^{-ik_1(z_j - z_1)}, \; z_j \leq z_1 \\ a_n e^{-ik_n(z_j - z_n)} + b_n e^{ik_n(z_j - z_n)}, \; z_j \geq z_n. \end{cases} \tag{2.29}$$

If we define a propagation factor $\zeta_j \equiv e^{ik_j \Delta}$, we can write Eq. (2.29)

$$\psi_j = \begin{cases} a_1 \zeta_1^{j-1} + b_1 \zeta_1^{1-j}, \; j \leq 1 \\ a_n \zeta_n^{n-j} + b_n \zeta_n^{j-n}, \; j \geq n. \end{cases} \tag{2.30}$$

We then obtain the following expressions for the wavefunction near the boundaries:

$$\begin{aligned} \psi_0 &= a_1 \zeta_1^{-1} + b_1 \zeta_1, \\ \psi_1 &= a_1 + b_1, \\ \psi_n &= a_n + b_n, \\ \psi_{n+1} &= a_n \zeta_n^{-1} + b_n \zeta_n. \end{aligned} \tag{2.31}$$

Combining the first and second pair of Eqs. (2.31) to eliminate b yields:

$$\begin{aligned} (\alpha_1 - E)\psi_0 - s_1 \psi_1 &= a_1 s_1 (\zeta_1^{-2} - 1), \\ -s_{n+1}\psi_n + (\alpha_n - E)\psi_{n+1} &= a_n s_{n+1} (\zeta_n^{-2} - 1), \end{aligned} \tag{2.32}$$

where $\alpha_1 - E \equiv s_1 \zeta_1^{-1}$ and $\alpha_n - E \equiv s_{n+1} \zeta_n^{-1}$. Combining the two equations (2.32) with the system of equations represented by (2.27) allows us to write the matrix representation

of the discrete Schrödinger equation:

$$\begin{pmatrix} \alpha_1 - E & -s_1 & & & & & \\ -s_1 & d_1 - E & -s_2 & & & & \\ & -s_2 & d_2 - E & -s_3 & & & \\ & & \ddots & \ddots & \ddots & & \\ & & & -s_n & d_n - E & -s_{n+1} & \\ & & & & -s_{n+1} & \alpha_n - E \end{pmatrix} \begin{pmatrix} \psi_0 \\ \psi_1 \\ \psi_2 \\ \vdots \\ \psi_n \\ \psi_{n+1} \end{pmatrix} = \begin{pmatrix} a_1 s_1(\zeta_1^{-2} - 1) \\ 0 \\ 0 \\ \vdots \\ 0 \\ a_n s_{n+1}(\zeta_n^{-2} - 1) \end{pmatrix}. \tag{2.33}$$

Given incident wave amplitudes a_1 and a_n the full wavefunction can be calculated by diagonalizing the above matrix provided that α_1 and α_n are known. This, in turn, requires that we specify the propagation factors $\zeta_{1,n}$ at the boundary points. To do this we will make use of the fact that the forward and backward traveling waves must satisfy the Schrödinger equation separately in the contact regions. Furthermore, in these regions the effective mass is constant and the wavefunction values on mesh points are related via simple phase shifts. Using these facts to solve the Schrödinger equation in the contacts yields the following energy-dependent boundary conditions:

$$\begin{aligned} E &= d_1 - s_1(\zeta_1^{-1} + \zeta_1), \\ E &= d_n - s_n(\zeta_n^{-1} + \zeta_n), \end{aligned} \tag{2.34}$$

or

$$\zeta_i = \frac{d_i - E}{2s_i} \pm \frac{1}{2}\sqrt{\left(\frac{E - d_i}{s_i}\right)^2 - 4}. \tag{2.35}$$

Concerning the sign in Eq. (2.35), the root is chosen such that $\Im(\zeta) \geq 0$, which corresponds to incoming electron waves per Eq. (2.30). Once calculated the ζ_i are used to determine the α_i, which are then plugged in to complete the matrix (2.33).

As a review, the QTBM method proceeds as follows: first, the s and d values are calculated from position-dependent effective masses and from the potential; second, for a given incoming energy E, the propagation factors $\zeta_{1,n}$ are calculated and used to determine $\alpha_{1,n}$; finally, the matrix is populated according to Eq. (2.33) and the equation is solved for ψ.

We again assume that we have only left-incident electrons (i.e. $a_n = 0$) so that the transmission probability is given by:

$$\widetilde{T} = \frac{|\psi_n|^2}{|a_1|^2}\frac{v_n}{v_1}, \tag{2.36}$$

where v_i is the electron velocity at the boundary points.

To determine the relative accuracy and applicability of these three methods, we will calculate the transmission probability using all three methods discussed in this chapter and compare them for a typical barrier. Consider the triangular barrier pictured in Fig. 2.4. The transmission probability for this barrier is pictured in Fig. 2.5.

From the figure the three methods give very similar results for small incident electron energies. However, at energies near and above the highest point of the barrier, the WKB result deviates from the numerical methods. It is well-known from quantum mechanics that incident electrons with energies larger than the barrier potential can nonetheless be reflected due to wavefunction interference effects. This reflection is the cause of $\widetilde{T} < 1$ at high energy as seen in the TMM and QTBM curves. We will be interested in accurately simulating this high energy behavior in two instances: first, in diodes where most of the barrier has been biased away, the current carrying electrons will have high energy with respect to the conduction band edge in the grounded electrode; second, when estimating the collector transfer characteristics in a hot electron transistor, the electrons arriving at the collector may have high energies. For these reasons the WKB approach is not

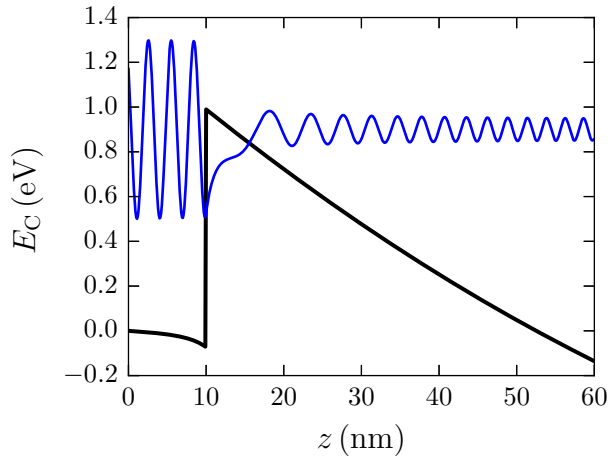

Figure 2.4: Triangular conduction band diagram used in the comparison of the transmission calculation methods. The wavefunction for an electron with incoming energy 0.9 eV, as calculated by the QTBM, is pictured in blue. The transmission probability can be understood graphically as the ratio of the wavefunction amplitudes at the edges of the barrier region.

suitable to our analysis. The other two methods, the TMM and the QTBM, give nearly identical results for the triangle barrier.

While the TMM and QTBM give comparable results in this case, there are two situations where the TMM is unreliable: first, for flat or nearly flat bands the values of the Airy functions appearing in Eqs. (2.20)−(2.22) become extremely large (as a result of the divergence of the u_i in Eq. (2.16)). Successive multiplication of matrices composed of these exponential growing terms leads to numerical overflow. This can result in large rounding errors when calculating theoretical diode currents. Second, the TMM is prone to numerical overflow when calculating bound states as in a two-dimensional electron gas (2DEG) or quantum well (in this case the u_i diverge in the complex plane). Therefore, the QTBM is the most widely applicable method for calculating transfer characteristics and this is the method we will use for the remainder of this thesis.

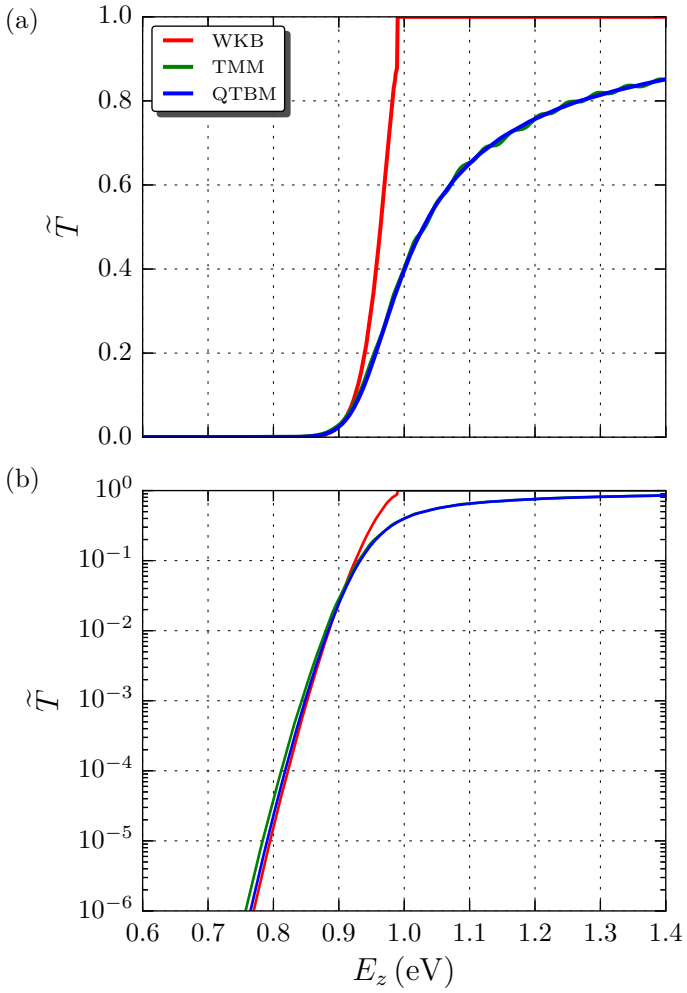

Figure 2.5: Transmission probability on a linear (a) and semilog (b) scale for the barrier in Fig. 2.4 calculated using the WKB, TMM and QTBM approaches. The three methods are in general agreement at low energies but the WKB curve begins to deviate from the TMM and QTBM curves at high energy.

2.2 Calculation of diode currents: The Tsu-Esaki formula

The ability to calculate the transmission coefficient of an arbitrary potential barrier is very useful when applied to the collector side of the HET. However, in order to accurately model diode transport and ultimately compare with experimental results, we must leverage the transmission probability to build a device-scale model of thermionic and thermionic field transport. Statistical physics allows us to transform the microscale description of the previous section into a macroscale description that is directly applicable to devices.

The conceptual picture of the model is as follows: the reservoirs surrounding the barrier region emit free electrons toward the barrier; each electron momentum state coherently evolves according the Schrödinger equation in the barrier region; finally, the transmitted component of the electron wave is collected by the reservoir on the opposite side of the barrier. In the previous section, we determined the precise nature of the interaction between each single electron and the barrier region. In this section we will add up the contributions from the thermally distributed electrons emitted from the reservoirs and thereby derive an expression for the voltage-dependent current. It should be noted that throughout this treatment we will neglect drift-diffusion and trap-assisted processes for simplicity. The theory of electron thermionic field emission from one parabolic band to another was first described by Tsu[67] and in this section we seek to elaborate upon this theory. Consider the simple potential barrier shown in Fig. 2.6. The differential current flowing from region 1 to region 2 is given by

$$\mathrm{d}J_{1\to 2} = qv_z \mathrm{d}n_{1\to 2}, \tag{2.37}$$

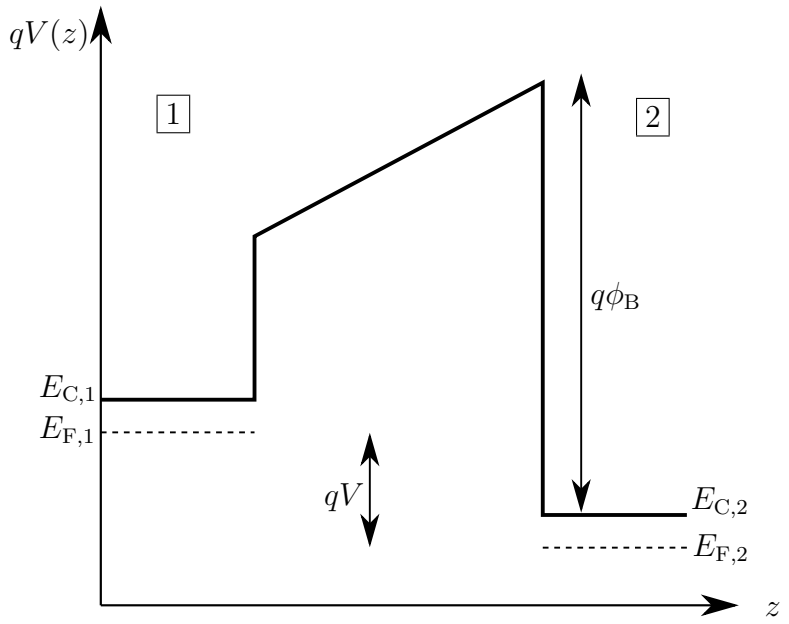

Figure 2.6: Generalized schematic potential used in the derivation of the Tsu-Esaki formula. The conduction band minima and quasi Fermi levels on either side are labeled $E_{\mathrm{C},i}$ and $E_{\mathrm{F},i}$, respectively. The applied bias is labeled V and the barrier height $q\phi_{\mathrm{B}}$.

where q is the elementary charge, v_z is the electron velocity in the direction perpendicular to the barrier (i.e. $\hat{z}$), and $\mathrm{d}n_{1\to 2}$ is the differential electron concentration flowing from region $1 \to 2$. The latter quantity is the product of the density of states in region 1, the occupation of full electron states in region 1, the occupation of empty electron states in region 2, the transmission probability of the barrier and the k-space volume element:

$$\mathrm{d}n_{1\to 2} = g_1(k_x, k_y, k_z)\widetilde{T}(k_z)f_1(\varepsilon)(1 - f_2(\varepsilon))\mathrm{d}k_x\mathrm{d}k_y\mathrm{d}k_z. \tag{2.38}$$

Here g_1 is the density of available electronic states in region 1 per volume in k-space, $\widetilde{T}(k_z)$ is the transmission probability at longitudinal momentum k_z and $f_i(\varepsilon)$ is the Fermi-Dirac function in region i. Note that $\mathrm{d}n_{1\to 2}$ has units of inverse volume as expected.

Throughout this section we will adopt the following notation: energies labeled with the Roman letter E will refer to absolute energies while those labeled with the Greek letter ε will refer to kinetic energies. For example, an electron with kinetic energy ε has total

energy $E = E_C + \varepsilon$ where E_C represents the energy at the conduction band edge. Also, transmission probabilities will be labeled with a tilde (as in $\widetilde{T}$) while absolute temperature will be labeled with the usual T. To avoid confusion, functions of temperature will always appear immediately next to powers of the Boltzmann constant (k_B).

With those conventions in mind, we can use Eq. (2.38) write the total current flowing from region 1 to region 2 as

$$dJ_{1\to 2} = qv_z g_1(k_x, k_y, k_z)\widetilde{T}(k_z) f_1(\varepsilon)(1 - f_2(\varepsilon))dk_x dk_y dk_z. \tag{2.39}$$

The density of states g_1 is calculated by assuming that the semiconductor is a cube of length L, which is much larger than a lattice constant. By applying periodic boundary conditions at the cube edges so that available free electron states are quantized, the k-space density of states can be calculated to be $1/4\pi^3$ (including spin degeneracy). Furthermore, we can make use of the dispersion relation for electrons in parabolic bands to write the following equations:

$$\begin{aligned}
\varepsilon &= \frac{\hbar^2}{2m^*}\left(k_x^2 + k_y^2 + k_z^2\right), \\
v_z &= \frac{1}{\hbar}\frac{\partial \varepsilon}{\partial k_z} = \frac{\hbar k_z}{m^*}, \\
\varepsilon_z &= \frac{\hbar^2 k_z^2}{2m^*}, \\
v_z dk_z &= \frac{1}{\hbar}\frac{\partial \varepsilon}{\partial k_z} dk_z = \frac{1}{\hbar} d\varepsilon_z,
\end{aligned} \tag{2.40}$$

where m^* is the parabolic band effective mass, assumed here to be isotropic.

Making these substitutions into Eq. (2.39) we find

$$dJ_{1\to 2} = \frac{q}{4\pi^3\hbar}\widetilde{T}(\varepsilon_z) d\varepsilon_z f_1(\varepsilon)(1 - f_2(\varepsilon)) dk_x dk_y. \tag{2.41}$$

We will now change coordinates from Cartesian (k_x,k_y) to cylindrical (k_ρ,φ) via the following relations:

$$\begin{aligned} k_\rho &= \sqrt{k_x^2 + k_y^2}, \\ \varphi &= \tan^{-1}\left(\frac{k_x}{k_y}\right), \\ \varepsilon_\rho &= \frac{\hbar^2 k_\rho^2}{2m^*}, \\ \mathrm{d}\varepsilon_\rho &= \frac{\hbar^2 k_\rho}{m^*}\mathrm{d}k_\rho, \\ \mathrm{d}k_x\mathrm{d}k_y &= k_\rho \mathrm{d}k_\rho \mathrm{d}\varphi. \end{aligned} \tag{2.42}$$

Substitution into Eq. (2.41) and integration over ε_z, ε_ρ and φ gives

$$J_{1\to 2} = \frac{qm^*}{2\pi^2\hbar^3}\int_0^\infty \widetilde{T}(\varepsilon_z)\mathrm{d}\varepsilon_z \int_0^\infty f_1(\varepsilon)(1 - f_2(\varepsilon))\mathrm{d}\varepsilon_\rho. \tag{2.43}$$

Note that because the integrands do not depend on the azimuthal angle, integration over φ has produced a factor of 2π.

The tunnel current from region 2 to region 1 is identical to Eq. (2.43) but with the Fermi-Dirac function indices swapped:

$$J_{2\to 1} = \frac{qm^*}{2\pi^2\hbar^3}\int_0^\infty \widetilde{T}(\varepsilon_z)\mathrm{d}\varepsilon_z \int_0^\infty f_2(\varepsilon)(1 - f_1(\varepsilon))\mathrm{d}\varepsilon_\rho. \tag{2.44}$$

The total current is then

$$\begin{aligned} J &= J_{1\to 2} - J_{2\to 1} \\ &= \frac{qm^*}{2\pi^2\hbar^3}\int_0^\infty \widetilde{T}(\varepsilon_z)\mathrm{d}\varepsilon_z \underbrace{\int_0^\infty (f_1(\varepsilon) - f_2(\varepsilon))\,\mathrm{d}\varepsilon_\rho}_{\equiv N(\varepsilon_z)}, \end{aligned} \tag{2.45}$$

where $N(\varepsilon_z)$ is the supply function and is related to the difference in supply electron concentrations on each side of the barrier. The first important result is:

$$\boxed{J = \frac{qm^*}{2\pi^2\hbar^3}\int_0^\infty \widetilde{T}(\varepsilon_z)N(\varepsilon_z)\mathrm{d}\varepsilon_z.} \tag{2.46}$$

To obtain a closed-form expression for Eq. (2.46) we need an analytical expression for the supply function $N(\varepsilon_z)$.

2.2.1 The supply function

The supply function appearing in Eq. (2.46) describes the source electron distribution that emerges from the reservoirs surrounding the barrier. We will assume the reservoir electrons follow a Fermi-Dirac distribution:

$$f(\varepsilon) = \frac{1}{1+\exp\left(\frac{\varepsilon+E_\mathrm{C}-E_\mathrm{F}}{k_\mathrm{B}T}\right)}, \tag{2.47}$$

where $\varepsilon = \varepsilon_x+\varepsilon_y+\varepsilon_z$ and E_F and E_C are the Fermi level and conduction band minimum, respectively, in the region of interest. The Fermi level at a given temperature and doping level is determined by solving the charge neutrality equation iteratively. Crucially, we also assume that the *tunnel current does not affect the electron distribution at the barrier edge.* This is tantamount to an assumption of quasi-equilibrium conditions in and around the barrier. It is also worth noting that while we will assume a Fermi-Dirac distribution for the simulations in this thesis, Eq. (2.46) is generally applicable to any carrier distribution functions that are isotropic in the plane of the barrier.

Recasting the distribution function as the sum of two terms we find

$$N(\varepsilon_z) = \int_0^\infty f_1(\varepsilon)\mathrm{d}\varepsilon_\rho - \int_0^\infty f_2(\varepsilon)\mathrm{d}\varepsilon_\rho. \tag{2.48}$$

If we again rewrite ε in terms of cylindrical components, the first term in Eq. (2.48) becomes

$$\int_0^\infty f_1(\varepsilon)\mathrm{d}\varepsilon_\rho = \int_0^\infty \frac{1}{1+\exp\left(\frac{\varepsilon_z+\varepsilon_\rho+E_{\mathrm{C},1}-E_{\mathrm{F},1}}{k_\mathrm{B}T}\right)}\mathrm{d}\varepsilon_\rho, \tag{2.49}$$

where $E_{\mathrm{F},1}$ is the quasi Fermi level and $E_{\mathrm{C},1}$ is the conduction band minimum in region 1 (See Fig. 2.6).

Finally, we define $x \equiv \frac{\varepsilon_z+\varepsilon_\rho+E_{\mathrm{C},1}-E_{\mathrm{F},1}}{k_\mathrm{B}T}$ and the resulting integral can be found in an integral table:

$$\int_0^\infty f_1(\varepsilon)\mathrm{d}\varepsilon_\rho = k_\mathrm{B}T\ln\left(1+\exp\left(\frac{E_{\mathrm{F},1}-\varepsilon_z-E_{\mathrm{C},1}}{k_\mathrm{B}T}\right)\right). \tag{2.50}$$

Adding the contribution from region 2 we find

$$N(\varepsilon_z) = k_\mathrm{B}T\ln\left(\frac{1+\exp\left(\frac{E_{\mathrm{F},1}-\varepsilon_z-E_{\mathrm{C},1}}{k_\mathrm{B}T}\right)}{1+\exp\left(\frac{E_{\mathrm{F},2}-\varepsilon_z-E_{\mathrm{C},2}}{k_\mathrm{B}T}\right)}\right). \tag{2.51}$$

Plugging this into Eq. (2.46) gives

$$J = \frac{qm^*}{2\pi^2\hbar^3}k_\mathrm{B}T\int_0^\infty \widetilde{T}(\varepsilon_z)\ln\left(\frac{1+\exp\left(\frac{E_{\mathrm{F},1}-\varepsilon_z-E_{\mathrm{C},1}}{k_\mathrm{B}T}\right)}{1+\exp\left(\frac{E_{\mathrm{F},2}-\varepsilon_z-E_{\mathrm{C},2}}{k_\mathrm{B}T}\right)}\right)\mathrm{d}\varepsilon_z. \tag{2.52}$$

This is the Tsu-Esaki formula[67]. It describes the thermionic and thermionic field emission current carried by electrons in parabolic bands. We can rewrite the prefactor using the Richardson constant

$$A^* \equiv \frac{4\pi qm^*k_\mathrm{B}}{h^3}, \tag{2.53}$$

to obtain

$$\boxed{J = \frac{A^* T}{k_\mathrm{B}} \int_0^\infty \widetilde{T}(\varepsilon_z) \ln\left(\frac{1+\exp\left(\frac{E_{\mathrm{F},1}-\varepsilon_z-E_{\mathrm{C},1}}{k_\mathrm{B}T}\right)}{1+\exp\left(\frac{E_{\mathrm{F},2}-\varepsilon_z-E_{\mathrm{C},2}}{k_\mathrm{B}T}\right)}\right) \mathrm{d}\varepsilon_z.} \tag{2.54}$$

For typical textbook derivations of thermionic emission currents (see Ref. [68], for example) the transmission characteristics are simplified such that

$$\begin{aligned} \widetilde{T}(\varepsilon_z) &= 0,\ \varepsilon_z < \varepsilon_{z,\mathrm{min}} \\ \widetilde{T}(\varepsilon_z) &= 1,\ \varepsilon_z \geq \varepsilon_{z,\mathrm{min}}. \end{aligned} \tag{2.55}$$

In other words electrons that have kinetic energy in excess of the barrier maximum are perfectly transmitted while those below are completely reflected. Plugging this condition in to Eq. (2.54) gives

$$\begin{aligned} J = \frac{A^* T}{k_\mathrm{B}} \int_{\varepsilon_{z1,\mathrm{min}}}^\infty \ln\left(1+\exp\left(\frac{E_{\mathrm{F},1}-\varepsilon_z-E_{\mathrm{C},1}}{k_\mathrm{B}T}\right)\right) \mathrm{d}\varepsilon_z \\ -\frac{A^* T}{k_\mathrm{B}} \int_{\varepsilon_{z2,\mathrm{min}}}^\infty \ln\left(1+\exp\left(\frac{E_{\mathrm{F},2}-\varepsilon_z-E_{\mathrm{C},2}}{k_\mathrm{B}T}\right)\right) \mathrm{d}\varepsilon_z, \end{aligned} \tag{2.56}$$

or

$$J = A^* T^2 \left(\exp\left(\frac{E_{\mathrm{F},1}-\varepsilon_{z1,\mathrm{min}}-E_{\mathrm{C},1}}{k_\mathrm{B}T}\right) - \exp\left(\frac{E_{\mathrm{F},2}-\varepsilon_{z2,\mathrm{min}}-E_{\mathrm{C},2}}{k_\mathrm{B}T}\right)\right). \tag{2.57}$$

If we consider the right hand lead in Fig. 2.6 (region 2) to be a metal, $E_{\mathrm{F},2} = E_{\mathrm{C},2} = 0$ and $\varepsilon_{z2,\mathrm{min}} = q\phi_\mathrm{B}$. In region 1, $\varepsilon_{z1,\mathrm{min}} = q\phi_\mathrm{B} - qV - E_{\mathrm{C},1} + E_{\mathrm{F},1}$. Plugging in these values to Eq. (2.57) gives:

$$\boxed{J = A^* T^2 \exp\left(\frac{-q\phi_\mathrm{B}}{k_\mathrm{B}T}\right)\left(\exp\left(\frac{qV}{k_\mathrm{B}T}\right)-1\right) = J_\mathrm{S}\left(\exp\left(\frac{qV}{k_\mathrm{B}T}\right)-1\right),} \tag{2.58}$$

where

$$J_{\mathrm{S}} \equiv A^{*}T^{2}\exp\left(\frac{-q\phi_{\mathrm{B}}}{k_{\mathrm{B}}T}\right) \tag{2.59}$$

is the saturation current. The saturation current is equal to either the leftward or rightward flowing current density at zero bias. These two currents, of course, cancel each other out at zero bias leading to zero net current flow by definition.

Equation (2.58) is the canonical thermionic emission current formula. Despite the simplicity of this equation, the more general expression given by Eq. (2.54) should be used to calculate diode current whenever possible. Equation (2.54) retains the contribution from tunneling electrons (i.e. thermionic field emission) and allows for the reflection of electrons that have kinetic energy in excess of $q\phi_{\mathrm{B}}$. For III-N barriers, which often employ thin polarization dipole layers containing large electric fields, electron resonance effects can lead to appreciable electron reflection even at high energy. Accurate diode simulations must account for this. All diode simulations that appear in this thesis will be generated with Eq. (2.54) using the QTBM method to calculate the transmission probability. A sample calculation, based on the triangular barrier in Fig. 2.4, is pictured in Fig. 2.7.

A modified form of Eq. (2.58) is usually used to analyze experimental $I-V-T$ data:

$$\boxed{J = J_{\mathrm{S}}\left(\exp\left(\frac{qV}{nk_{\mathrm{B}}T}\right)-1\right)}, \tag{2.60}$$

where n is called the ideality factor. Ideal diodes described by purely thermionic transport are characterized by $n = 1$ and, in general, the magnitude of n in excess of unity is a measure of the nonideality of the device characteristics. Broadly speaking there are two causes of the condition $n > 1$: first, voltage partitioning reduces the proportion of the applied bias that appears across the intrinsic device. Partitioning can be due to ohmic voltage drops in the device contacts and access regions or to a spatial separation between

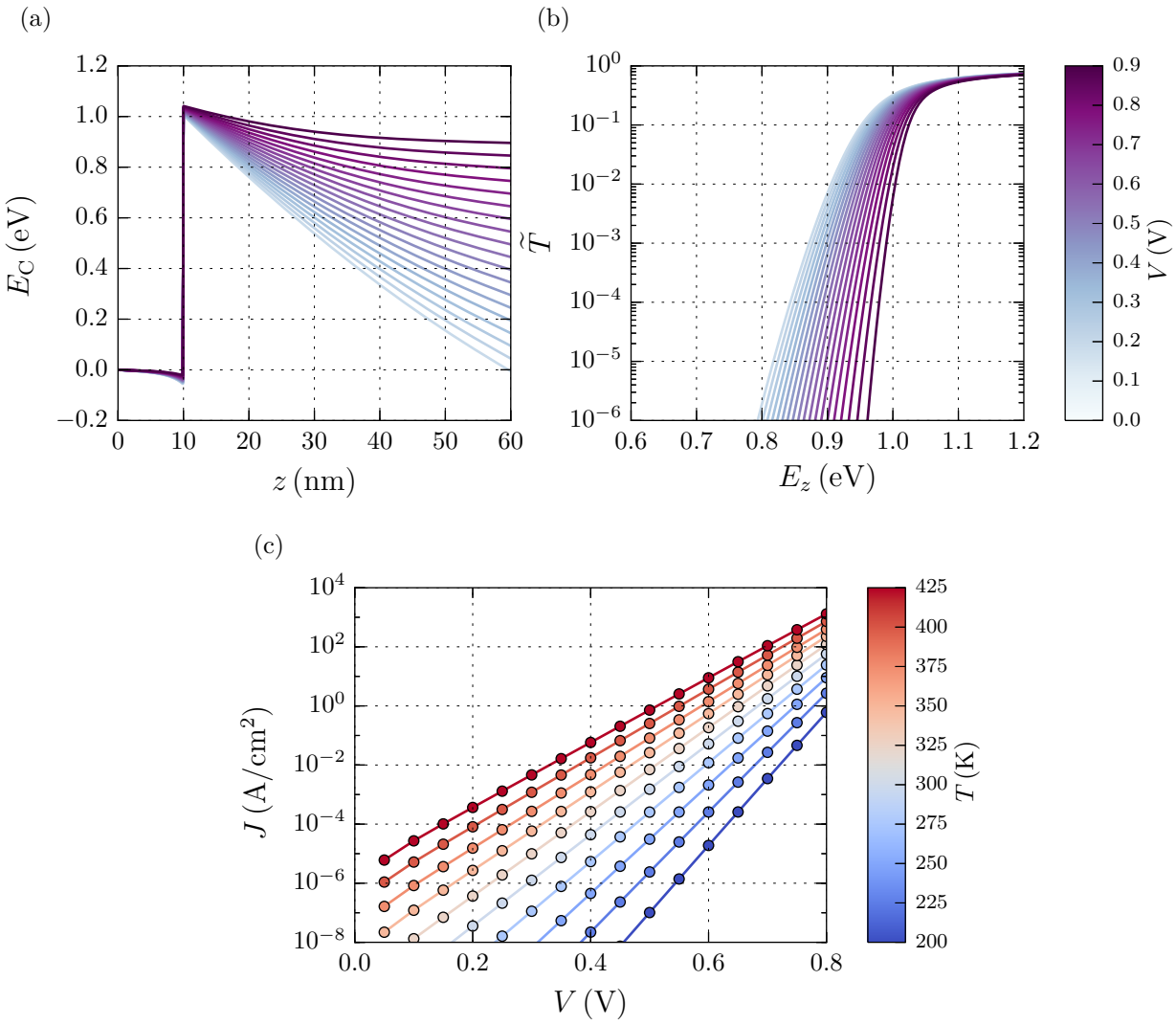

Figure 2.7: Numerical calculation of diode $I-V-T$ characteristics based on Eq. (2.54). Pictured are (a) the conduction band diagram and (b) the bias-dependent transmission probability. The forward bias $I-V-T$ curves are pictured in (c).

the barrier maximum and the control electrode. Both of these effects are straightforward to understand and will be explored in the coming chapters. Second, $n > 1$ can be caused by the existence of current transport processes that are not strictly thermionic. A classic example is the presence of generation-recombination currents in p−n diodes, which causes $n \sim 2$ in certain regimes of device bias[68]. Processes like field emission (i.e. tunneling) and trap-assisted transport can also cause $n > 1$. For extreme cases where $n \gg 1$, the exponential in Eq. (2.60) can be Taylor expanded to first order in the applied bias resulting in $J \propto V$, or ohmic transport. On the other hand, $n = 1$ represents the smallest possible dynamic resistance for intraband transport between Fermi-Dirac ensembles. We may, therefore, consider the magnitude of n to be directly proportional to the "resistivity" of the transport process in question.

Throughout this thesis both simulated and experimental diode $I-V-T$ characteristics will be analyzed by using Eq. (2.60) to extract the temperature and bias-dependence of the barrier height (ϕ_{B}) and ideality factor (n). As we will see, such an analysis will allow us to better understand the transport processes that dominate in real devices.

2.3 Example: The GaN Schottky diode

To test the efficacy of our model based on Eq. (2.54) and to understand the procedure for analyzing real devices we will now compare simulated and experimental results using a GaN Schottky diode as a test structure (Fig. 2.8). Our goal will be to determine the degree to which potentially anomalous diode characteristics can be attributed to thermionic field emission effects.

The method for comparing theoretical and experimental results of the GaN Schottky diode will proceed as follows: first, a set of theoretical $I-V-T$ curves is generated using Eq. (2.54) and a design band diagram. Second, epitaxial layers are grown by metal-

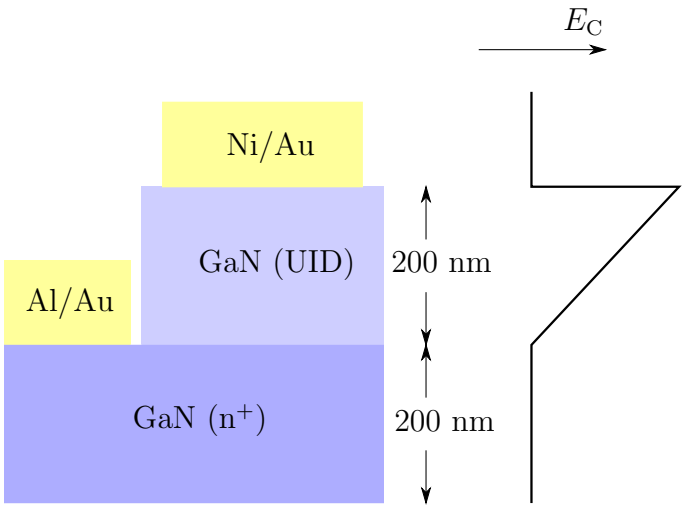

Figure 2.8: Layer structure and associated conduction band diagram for the GaN Schottky diode.

organic chemical vapor deposition (MOCVD) in the Ga-polar orientation on a sapphire substrate according to the design pictured in Fig. 2.8. Diode structures are fabricated and $I-V-T$ data are taken. Next, both sets of data are fitted and analyzed according to the procedure outlined in this section. Finally, the theoretical and experimental quantities that are extracted from the analysis are compared. As the data are presented, we will pause to consider any relevant implications for device transport.

The theoretical and experimental forward bias $I-V-T$ characteristics of a GaN Schottky diode are pictured in Fig. 2.9. Thermionic emission currents are exponentially dependent on forward bias so that the current increases by many orders of magnitude over a relatively small bias range. For this reason a semilog scale is most appropriate for our analysis.

For low biases the current increases exponentially and the semilog current is linear. In the experimental data (Fig. 2.9(b)), ohmic voltage drops in the device extrinsic regions limit the magnitude of the forward current and cause a flattening of the curves at high bias. These extrinsic effects are not accounted for in the simulations and are, therefore, not present in the theoretical curves. Because we are interested in intrinsic

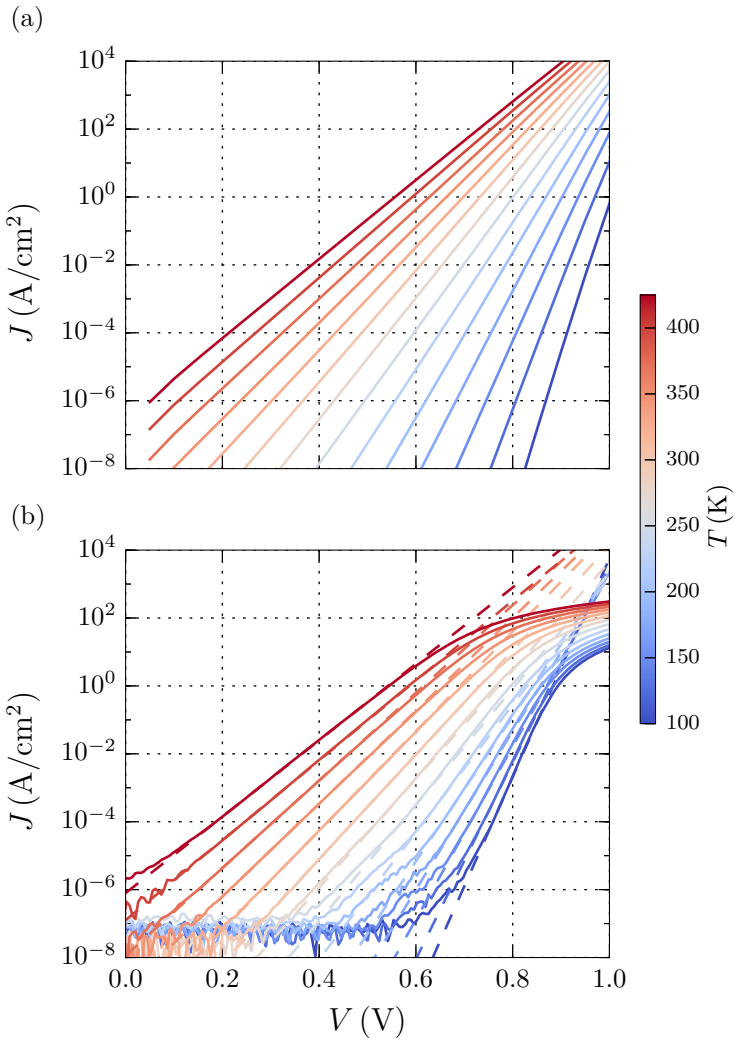

Figure 2.9: Semilog plot of theoretical (a) and experimental (b) forward bias $I-V-T$ curves for the GaN Schottky diode. The linear fit for each temperature is represented by a dashed line.

device transport, we will restrict the following analysis to low bias regimes where resistive voltage drops are negligible.

Comparing the low bias regimes of the theoretical and experimental curves pictured in Fig. 2.9, we find good agreement at high temperatures; at low temperatures theoretical calculations underestimate the magnitude of the current present in the real device. Therefore, we may make the following hypothesis at the outset of our analysis: the thermionic emission model represented by Eq. (2.54) accurately describes charge transport in the GaN Schottky diode at high temperatures; at low temperatures, an additional, unknown transport mechanism dominates. This simple observation is crucial; however, further analysis is needed to obtain a more detailed picture of device transport.

To this end we rewrite Eq. (2.60) on a semilog scale:

$$\ln(J) = \ln(J_{\mathrm{S}}) + \frac{q}{nk_{\mathrm{B}}T}V, \tag{2.61}$$

where we have assumed that the diode is sufficiently forward biased that the reverse current contribution is negligible. A linear fit to $\ln(J) - V$ data that obey Eq. (2.61) has slope $q/nk_{\mathrm{B}}T$ and ordinate axis intercept $\ln(J_{\mathrm{S}})$. In our analysis such a linear fit is performed at each temperature for both the theoretical and experimental data. These fits are represented by dashed lines in Fig. 2.9. From the slope and the intercept of the fit line, n and J_{S} can be determined, respectively.

If the Richardson constant (A^*) is known, the barrier height can be determined from J_{S} via Eq. (2.59):

$$\phi_{\mathrm{B}} = \frac{k_{\mathrm{B}}T}{q}\ln\left(\frac{A^*T^2}{J_{\mathrm{S}}}\right). \tag{2.62}$$

The ideality factor and the barrier height are extracted from the theoretical and experimental $I - V$ curves using this method and the known theoretical value of the

Richardson constant in GaN ($26.4\,\mathrm{A/cm^2K^2}$). The results are pictured in Fig. 2.10.

The data in Fig. 2.10 demonstrate the close agreement between theoretical and experimental quantities at high temperatures. This agreement reinforces our earlier observation that the thermionic field emission model accurately describes the high temperature physics of real Schottky diodes. However, at low temperatures, experimental values of the ideality factor are higher and calculated barrier heights are lower than theoretical predictions. To understand these results, we will first discuss the theoretical values.

For an ideal diode described by Eq. (2.58), n and ϕ_{B} are independent of temperature (i.e. $n = 1$). However, Fig. 2.10 reveals gentle dependencies of both of these simulated quantities on temperature. As we will see, these trends can be explained entirely by the thermionic field emission component of the current given by Eq. (2.54). Consider first the increase in the theoretical n from ~ 1.05 to ~ 1.1 with decreasing temperature. We can consider the integral in Eq. (2.54) to be the sum of two components: the thermionic field component of the total current is carried by electrons with kinetic energy less than the barrier height (ϕ_{B}); the purely thermionic component is carried by electrons with energies greater than ϕ_{B}. Therefore, by integrating Eq. (2.54) up to $\varepsilon_z = \phi_{\mathrm{B}}$ and dividing by the total current, we can determine the fraction of the total current attributed to thermionic field emission at each temperature (Fig. 2.11).

Because the transmission probability is variable for tunneling electrons, thermionic field emission appears to be more "resistive" than pure thermionic transport. To understand this, consider the assumption of perfect transmission for high energy electrons incident on a barrier. This assumption implies that the barrier acts as a perfect high pass filter for incident electrons. The exponential distribution of incident electrons, therefore, ensures a perfectly exponential $I - V$ relationship. By contrast, if we allow for the possibility of quantum mechanical reflections at the barrier interface, the transmission probability will vary within the energies occupied by the incident electron distribution.

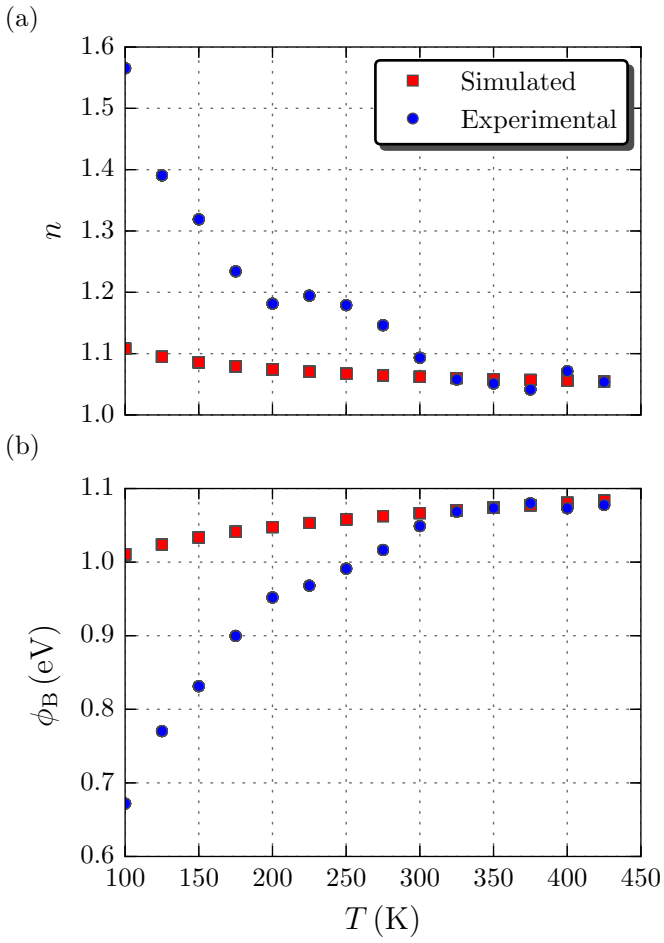

Figure 2.10: Simulated and experimental values of (a) the ideality factor and (b) the barrier height. The latter were calculated using $A^* = 26.4\,\mathrm{A/cm^2K^2}$. Theoretical and experimental values agree well for high temperatures but diverge as the temperature decreases.

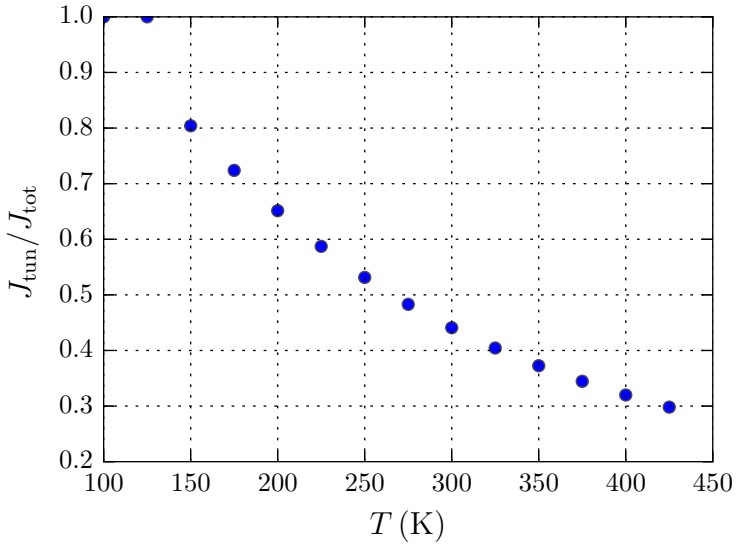

Figure 2.11: Thermionic field emission current contribution as a function of temperature. Because the thermionic field emission process is more resistive, the increase in the thermionic field component with decreasing temperature leads directly to the increase in simulated ideality factor.

Therefore, the barrier no longer transmits the exponential tail of the incident distribution as it does for pure thermionic emission, but rather acts as a comparatively more complicated electron filter. The result is that as thermionic field emission becomes dominant, n increases beyond unity.

Next, we will consider the slight increase in the theoretically extracted barrier height with temperature seen in Fig. 2.10(b). This phenomenon is best understood by considering the energy distribution of transmitted electrons $\widetilde{T}(E_z)N(E_z)$ (Fig. 2.12). These curves indicate the relative contribution from electrons in the energy range E_z to $E_z+\mathrm{d}E_z$ to the total current, which is simply the area under each curve in Fig. 2.12 multiplied by A^*T/k_{B}.

For a given temperature, the electron concentration decreases with energy while the transmission probability increases. These opposing trends result in local maxima in the product $\widetilde{T}(E_z)N(E_z)$ (labeled as colored dots in Fig. 2.12). These maxima indicate

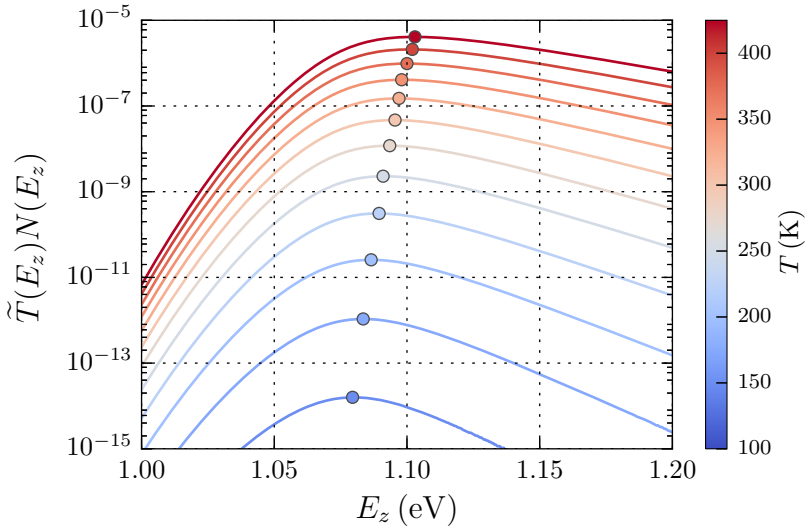

Figure 2.12: Energy distribution of the emitted electrons at a forward bias of 0.7 V. The dots on each curve represent the maximum value of the product $\widetilde{T}(E_z)N(E_z)$. These curves are an indicator of which injection energies contribute most to overall diode current. The increase in the energy of these maxima leads to an increase in barrier height with temperature as seen in simulated $I-V-T$ curves.

which electron energies contribute most to overall device current. As the temperature increases, the local maxima move to increasingly higher energies. In other words, the average electron injection energy increases with temperature such that ϕ_{B} appears to increase. The observed trends in both simulated n and simulated ϕ_{B} with temperature can, therefore, be clearly explained by thermionic field emission effects.

The ideality factor and the barrier height contain the effects of voltage and temperature, respectively, on device current. The overall magnitude is determined by the Richardson constant (A^*). Up to this point, calculating ϕ_{B} has required an input value of A^*. The advantage of this method is that ϕ_{B} can be determined from a single temperature $I-V$ curve; however, it is sometimes difficult to accurately predict the value of A^* a priori. A more rigorous method is to use a family of $I-V-T$ curves to extract both ϕ_{B} and A^* simultaneously. To do this we rewrite the expression for the saturation

(a)

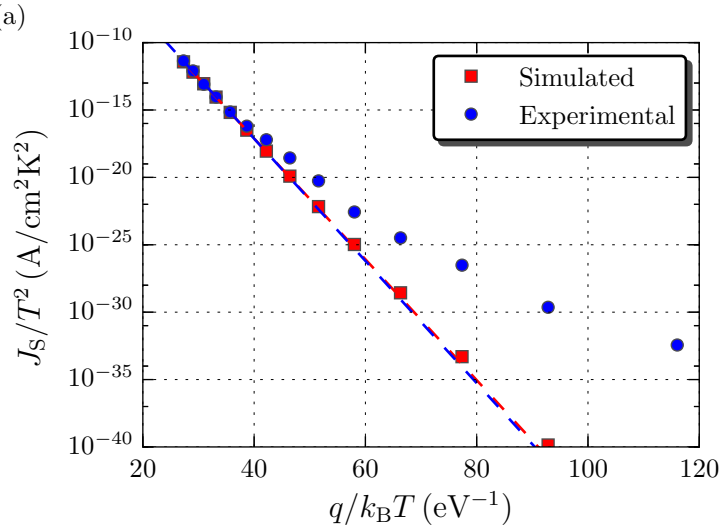

(b)

	ϕ_B (eV)	A^* (A/cm^{2}K^2)
Simulated	1.03	6.45
Experimental	1.04	10.2

Figure 2.13: (a) Simulated (red) and experimental (blue) Richardson plots. The dashed lines represent linear fits to the high temperature data. (b) Table of barrier height and Richardson constant values extracted from the high temperature linear fits.

current in Eq. (2.59) on a semilog scale:

$$\ln\left(\frac{J_S}{T^2}\right) = \ln(A^*) - \frac{q\phi_B}{k_BT}. \tag{2.63}$$

A plot of the left hand side of Eq. (2.63) versus q/k_BT is called a Richardson plot. In the event that such a plot is linear, ϕ_B and A^* can be determined from the slope and intercept of a linear fit, respectively. A Richardson plot of the theoretical and experimental data is pictured in Fig. 2.13.

The Richardson data are linear at high temperatures for both the theoretical and the experimental data. Linear fits are performed in this high temperature region and the extracted barrier heights and Richardson constants are listed in Fig. 2.13(b). These values are in excellent agreement, again verifying the accuracy of the simulation at high temperature. At low temperatures both sets of data experience "bowing" or nonlinearity. The slight bowing in the theoretical Richardson data is due to the thermionic field emission effects discussed earlier. In particular, as the apparent barrier height decreases with temperature, J_S/T^2 decreases at a rate that is slower than would be expected if the barrier height were independent of temperature. The comparatively large bowing present in the experimental data, therefore, cannot be explained by thermionic field emission effects alone. This suggests the presence of a transport mechanism that has not yet been accounted for.

The theoretical value of the Richardson constant ($26.4\,\mathrm{A/cm^2K^2}$) is derived under the assumption of perfect transmission for high-energy electrons. As we have seen, there can be appreciable electron reflection at the metal-semiconductor interface that can affect the extracted value of A^*. To determine the effect of quantum mechanical reflection on the Richardson constant, we turn to the conditions (2.55). Formally, we assumed that the transmission probability for electrons with energy equal to or larger than the barrier maximum is unity. If we modify this assumption so that these electrons are instead transmitted with probability $\widetilde{T}_0$, it is straightforward to show that Eq. (2.59) is preserved with the modified Richardson constant

$$A^{**} \simeq \widetilde{T}_0 A^*. \tag{2.64}$$

Strictly speaking, the transmission probability is not constant over the entire energy range occupied by the source electrons. Therefore, Eq. (2.64) is useful primarily as an

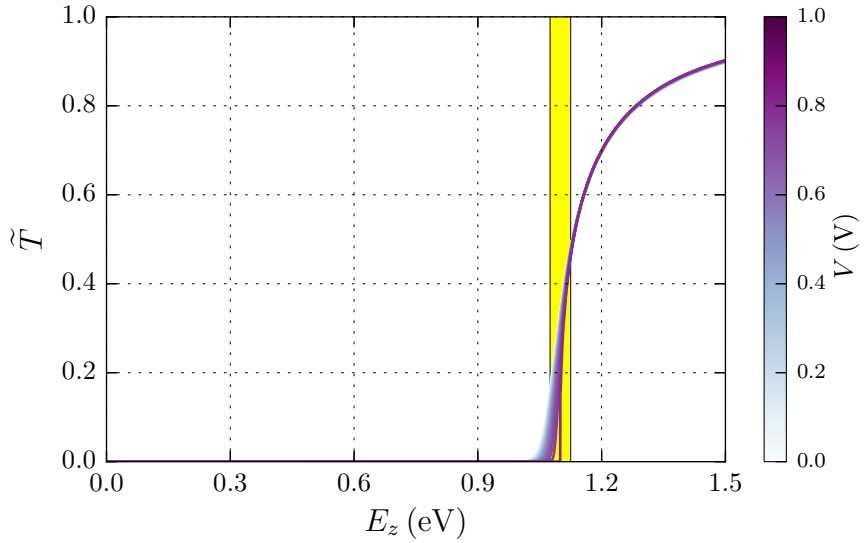

Figure 2.14: Transmission probability of the GaN Schottky diode. The yellow box indicates the energy of the barrier maximum.

order of magnitude estimate. Consider the value $A^* = 6.45\,\mathrm{A/cm^2K^2}$ extracted from the simulated $I-V-T$ curves along with the transmission characteristics for the GaN Schottky diode shown in Fig. 2.14. If we take the transmission probability in the vicinity of the barrier maximum to be ~ 0.25, we would expect a Richardson constant of $0.25 \times 26.4\,\mathrm{A/cm^2K^2} = 6.6\,\mathrm{A/cm^2K^2}$, nearly identical to the value we extract. For more extreme cases like the tunnel injectors used in Ga-polar HETs (see Chapter 4), we expect small tunneling probabilities to result in $A^* \ll 26.4\,\mathrm{A/cm^2K^2}$.

The data presented in this section have demonstrated the need for a conceptual shift in our understanding of A^*. Whereas the Richardson constant was formally thought to be a strictly material quantity (determined by the effective mass in the source electron material), a more accurate picture is one where A^* is *both* a material and a device concept. In other words, we cannot separate the value of A^* from the specific device structure under consideration. There is no "Richardson constant for GaN" but rather a "Richardson constant for device X."

In this section we have accurately described the relevant $I-V-T$ characteristics for simulated and high-temperature experimental diode currents. In particular, we have attributed the slight temperature dependence of simulated values of ϕ_{B} and n to thermionic field emission effects. Furthermore, we have discussed the effect of quantum mechanical reflections at the barrier interface on the extracted value of A^*. However, none of these concepts can explain the experimental low-temperature behavior of the GaN Schottky diode. For real diodes, the low-temperature changes in ϕ_{B}, n and the linearity of the Richardson plot are all more extreme than thermionic field emission theory would suggest. In the next section, we will introduce a new effect that can account for the extreme low-temperature behavior of experimental diodes.

2.4 Barrier height inhomogeneity theory

In the final section of this chapter, we will discuss the effects of laterally inhomogeneous barrier heights on measured transport properties. Until now we have implicitly assumed that the barrier height in Eq. (2.59) is constant in the plane of the band discontinuity. In real devices this barrier height can fluctuate in the lateral dimension (Fig. 2.15) and give rise to nonideal current characteristics. We will discuss the physical origin of these fluctuations and the requisite data analysis methods in later chapters. In this section we aim only to determine the effects of lateral inhomogeneity on Eqs. (2.58)−(2.59).

Barrier height inhomogeneity (BHI) has become a leading candidate to explain anomalous $I-V$ behavior in real Schottky diodes. The presence of BHI was first proposed to explain the large discrepancy between barrier heights extracted via $I-V$ and $C-V$ methods[69, 70]. A parallel conduction model, in which a nominally uniform barrier is replaced with two or more barriers in parallel, was found to accurately describe such

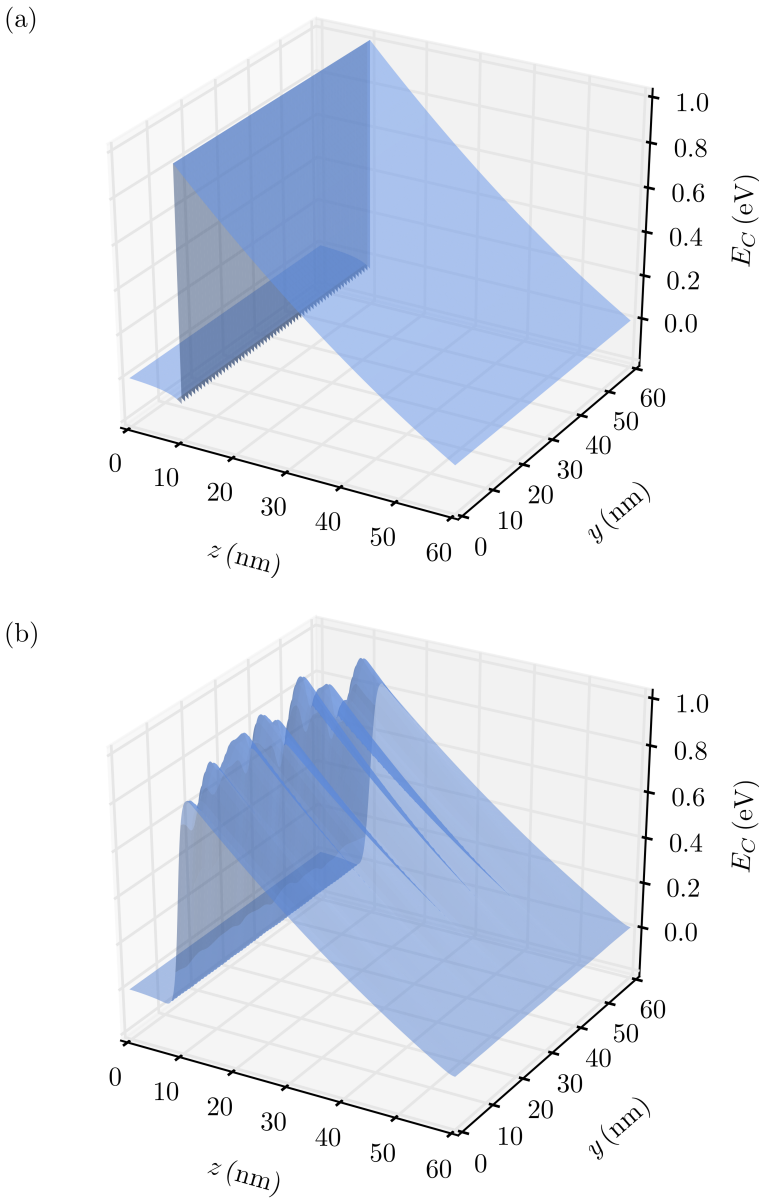

Figure 2.15: 3-dimensional schematic of the conduction band diagram for a laterally (a) homogeneous and (b) inhomogeneous triangle barrier.

nonideal behavior in $IrSi_x$/Si Schottky diodes. The physical origin of BHI in these diodes was thought to be the coexistence of several stable phases of $IrSi_x$, each of which forms a unique interface dipole with Si. Several years later internal photoemission spectroscopy was done on both n-Si[71] and p-Si[72] Schottky diodes and the observed BHI was attributed to nonuniform native oxide thickness and nonuniform interface state density, respectively.

The first comprehensive theory describing the effects of BHI on the transport properties of thermalized electrons was proposed by Tung[73]. The theory holds that an applied bias can distort the inhomogeneous barrier potential via the "pinch-off" effect[74] causing the mean barrier height to increase with bias. Furthermore, the thermalized electron distribution near the barrier varies with lattice temperature so that at high temperature, for example, a larger number of electrons "sample" high barrier regions than at low temperature. These two effects conspire to produce $I-V-T$ characteristics that are more accurately described by replacing the constant barrier height with a bias and temperature-dependent barrier height ($\phi_{\mathrm{B}} \rightarrow \phi'_{\mathrm{B}}(V,T)$) in the usual thermionic emission equations.

To understand this effect quantitatively, we begin with Eq. (2.59) and replace ϕ_{B} with a statistical distribution of barrier heights. In general, one can consider any arbitrary distribution of barrier heights and calculate the resulting $I-V-T$ characteristics. Most of these distributions require the use of simulation software to obtain numerical results. Here, we will consider a Gaussian distribution of barrier heights to obtain analytical results, which can be more easily interpreted. Such a distribution has the form

$$P(\phi_{\mathrm{B}}) = \frac{1}{\sigma_{\mathrm{S}}\sqrt{2\pi}} \exp\left(-\frac{(\overline{\phi}_{\mathrm{B}} - \phi_{\mathrm{B}})^2}{2\sigma_{\mathrm{S}}^2}\right), \tag{2.65}$$

where $\overline{\phi}_{\mathrm{B}}$ is the mean barrier height and σ_{S} is the standard deviation. The distribution

has been normalized such that $\int_{-\infty}^{\infty} P(\phi_{\mathrm{B}})\mathrm{d}\phi_{\mathrm{B}} = 1$.

To obtain the saturation current for an inhomogeneous barrier we replace $\exp(-q\phi_{\mathrm{B}}/k_{\mathrm{B}}T)$ in Eq. (2.59) with a weighted sum over the distribution:

$$\begin{aligned} J_S &= A^*T^2 \int_{-\infty}^{\infty} P(\phi_{\mathrm{B}})\exp\left(\frac{-q\phi_{\mathrm{B}}}{k_{\mathrm{B}}T}\right)\mathrm{d}\phi_{\mathrm{B}} \\ &= \frac{A^*T^2}{\sigma_{\mathrm{S}}\sqrt{2\pi}} \int_{-\infty}^{\infty} \exp\left(-\frac{(\overline{\phi}_{\mathrm{B}} - \phi_{\mathrm{B}})^2}{2\sigma_{\mathrm{S}}^2}\right)\exp\left(\frac{-q\phi_{\mathrm{B}}}{k_{\mathrm{B}}T}\right)\mathrm{d}\phi_{\mathrm{B}} \\ &= A^*T^2\exp\left(\frac{-q}{k_{\mathrm{B}}T}\left(\overline{\phi}_{\mathrm{B}} - \frac{q\sigma_{\mathrm{S}}^2}{2k_{\mathrm{B}}T}\right)\right). \end{aligned} \tag{2.66}$$

The details of the integral evaluation can be found in Appendix A. Equation (2.66) can be rewritten

$$J_S = A^*T^2\exp\left(\frac{-q\phi_{\mathrm{B}}^{'}}{k_{\mathrm{B}}T}\right), \tag{2.67}$$

where

$$\phi_{\mathrm{B}}^{'} \equiv \overline{\phi}_{\mathrm{B}} - \frac{q\sigma_{\mathrm{S}}^2}{2k_{\mathrm{B}}T}. \tag{2.68}$$

We are, therefore, able to model a Gaussian barrier distribution and its effect on thermal electrons with a single homogeneous, temperature-dependent barrier.

The voltage dependence of $\phi_{\mathrm{B}}^{'}$ is implicitly contained in the term σ_{S}, which is, in general, bias-dependent. To understand this consider the inhomogeneous barrier in Fig. 2.15(b) to be composed of "patches" within which the barrier height is constant. If these patches responded to bias-induced electric fields identically, one would not expect σ_{S} to depend on bias. In this case the values of the barrier height in each patch may change with bias, but the overall shape of the distribution would remain constant. In actuality the patches do not respond identically to bias. For a given applied bias, the low barrier patches allow more current to flow and are thus less able to absorb additional applied voltage than the high barrier patches. The result is that the low and high barrier

patches respond differently to bias in such a way that the overall barrier distribution is distorted. In particular, forward bias lowers the high barrier regions more than it does low barrier regions so that the overall barrier distribution becomes more homogeneous. Therefore, strictly speaking the apparent barrier height is a function of *both* bias and temperature. When discussing inhomogeneous barriers, we will refer only to values of $\phi_{\mathrm{B}}^{'}$, or the apparent barrier height, and $\overline{\phi}_{\mathrm{B}}$ the mean value of an inhomogeneous barrier distribution. Because we have shown that the apparent barrier height depends on both bias and temperature, the unqualified concept of "barrier height" (ϕ_{B}) has no relevant physical meaning.

Including the effects of thermionic field emission (via A^{**}) and of BHI (via $\phi_{\mathrm{B}}^{'}(V,T)$), we may write a single master equation describing real diode transport:

$$\boxed{J = A^{**}T^{2}\exp\left(-\frac{q\phi_{\mathrm{B}}^{'}(V,T)}{k_{\mathrm{B}}T}\right)\left(\exp\left(\frac{qV}{k_{\mathrm{B}}T}\right)-1\right)}. \tag{2.69}$$

Note that there is no explicit use of the ideality factor n in Eq. (2.69). An alternate form of Eq. (2.69) can be written by replacing the bias-dependent apparent barrier height with the barrier height at zero bias ($\phi_{\mathrm{B}}^{'}(V,T) \rightarrow \phi_{\mathrm{B}}^{'}(0,T)$) and by replacing V with V/n. This replacement makes it clear that the physical source of the ideality factor within BHI theory is the bias-dependence of σ_{S} in Eq. (2.68). Setting these two forms of the diode equation equal to each other yields an expression for the ideality factor:

$$n = \left(1 - \frac{q}{2k_{\mathrm{B}}T}\frac{\sigma_{\mathrm{S}}^{2}(0) - \sigma_{\mathrm{S}}^{2}(V)}{V}\right)^{-1}, \tag{2.70}$$

where $\sigma_{\mathrm{S}}(0)$ is the standard deviation of the barrier height fluctuations at zero bias. Equation (2.70) suggests that the ideality factor will decrease with increasing temperature, as it does in Fig. 2.10, as a larger number of high-energy carriers "rides above" the

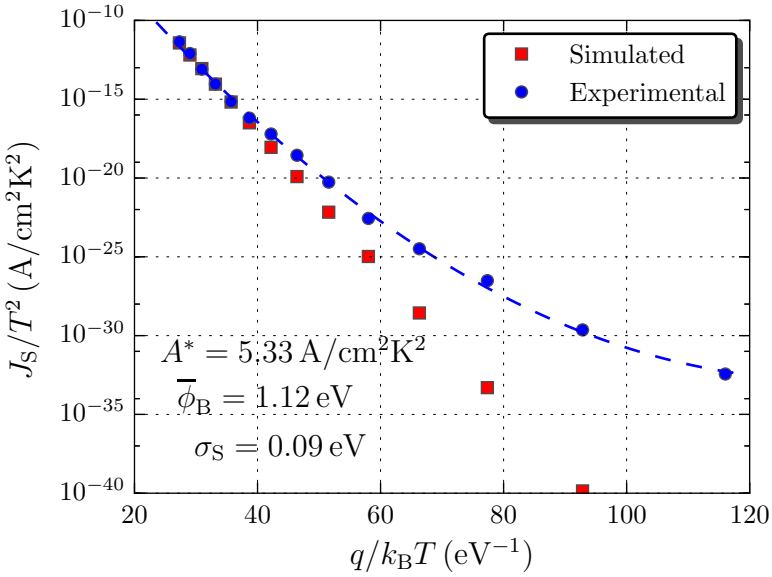

Figure 2.16: Simulated (red) and experimental (blue) Richardson plots. The blue dashed line represents a quadratic fit to the data and A^{**}, $\overline{\phi}_\mathrm{B}$ and σ_S are extracted via Eq. (2.71).

potential fluctuations.

Finally, we turn to the effect of BHI on the Richardson plot. The replacement of ϕ_B with $\phi_\mathrm{B}^{'}(V,T)$ modifies Eq. (2.63) in such a way that it becomes nonlinear in powers of $q/k_\mathrm{B}T$:

$$\ln\left(\frac{J_\mathrm{S}}{T^2}\right) = \ln(A^{**}) - \left(\frac{q}{k_\mathrm{B}T}\right)\overline{\phi}_\mathrm{B} + \frac{1}{2}\left(\frac{q}{k_\mathrm{B}T}\right)^2\sigma_\mathrm{S}^2. \tag{2.71}$$

A quadratic fit to a plot of $\ln(J_\mathrm{S}/T^2)$ vs. $q/k_\mathrm{B}T$ immediately yields A^{**}, $\overline{\phi}_\mathrm{B}$ and σ_S from the zeroth, first and second order coefficients, respectively. A modified Richardson plot of the GaN Schottky data displaying the quadratic fit is pictured in Fig. 2.16. The quadratic equation (2.71) provides an excellent fit to the experimental Richardson data. Additionally, the extracted values of $\overline{\phi}_\mathrm{B}$ and A^{**} are nearly identical to the expected values. The relatively small barrier height standard deviation of 8% results in a large nonlinear component as the temperature becomes small.

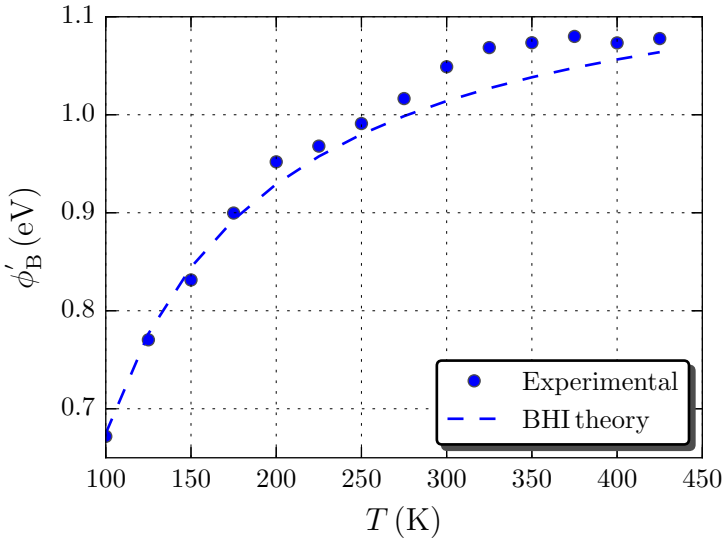

Figure 2.17: Apparent barrier height from experimental data (blue) and BHI theory (dashed line). The latter are calculated using the values of $\overline{\phi}_B$ and σ_S extracted from the nonlinear Richardson plot in Fig. 2.16.

Using the values of $\overline{\phi}_B$ and σ_S extracted from the nonlinear Richardson plot, we can compare the expression (2.68) to the experimental values of the apparent barrier height (Fig. 2.17). We find that Eq. (2.68) accurately describes the temperature dependence of the apparent barrier height over the entire temperature range.

In this chapter we have developed a theory of coherent electron transport that allows us to calculate the transmission probability for an arbitrary barrier. Such a calculation enables the generation of theoretical diode $I-V-T$ curves that include the effects of thermionic field emission. We have also introduced the concept of barrier height inhomogeneity and shown that its presence can explain anomalous low-temperature Schottky diode $I-V$. In the next two chapters, we will analyze experimental hot electron transistor (HET) and emitter diode data in light of the theories we have developed in this chapter. Chapter 3 will cover N-polar HETs with InGaN injector barriers; Chapter 4 will cover Ga-polar HETs with AlN injector barriers.

Chapter 3

N-polar HETs and InGaN emitter diode transport

In this chapter we will discuss the material and electrical characteristics of the Nitrogen-polar HET. We will begin by describing the N-polar HET design and its advantages over Ga-polar devices. Second, we will discuss the growth, fabrication and current transport characteristics of a first-generation device. Third, we will introduce the N-polar HET as a tool to study InGaN emitter barrier transport. More broadly we will demonstrate that such a tool can provide a useful probe into fundamental materials science phenomena. Numerical simulations will supplement our analysis of experimental data whenever possible. Finally, we will discuss the implications of our analysis for current-generation N-polar HETs.

3.1 Device design, growth and fabrication

The design structure of the N-polar HET is based on the polarization dipole barrier approach discussed in Chapter 1. However, because the signs of the polarization

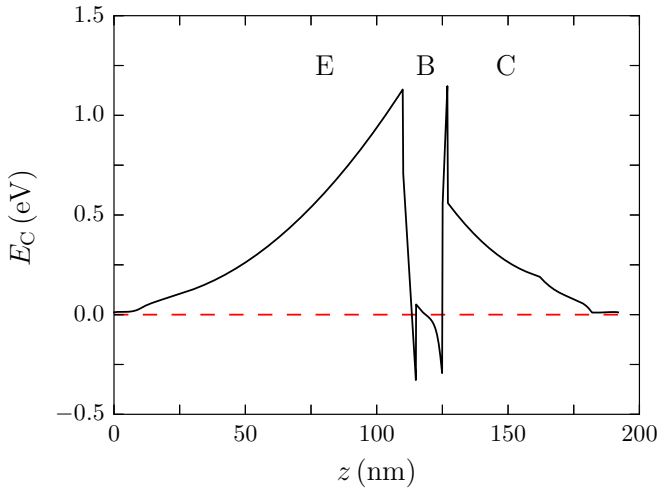

Figure 3.1: Conduction band diagram for the N-polar HET with 10 nm GaN base. The regions of the band diagram that correspond to the emitter, base and collector have been labeled along with the equilibrium Fermi level (dashed red line).

charge discontinuities are opposite those of Ga-polar interfaces, the roles of the InGaN and AlGaN polarization dipole barriers are reversed with respect to Ga-polar HETs. Specifically, an InGaN polarization dipole is used to form the emitter barrier while an AlGaN polarization dipole forms the collector. A typical band diagram for an N-polar polarization dipole barrier HET is shown in Fig. 3.1.

N-polar polarization dipole HETs have several distinct advantages over their Ga-polar counterparts. First, the majority of the 2DEG charge is induced by the AlGaN/GaN junction, which is located on the collector side of the base rather than on the emitter side. Therefore, etching off the emitter does not deplete the base charge in the access regions as it does in Ga-polar HETs. Second, because InGaN has a smaller band gap than GaN, depositing ohmic metals directly on the InGaN layer provides a low-resistance, unalloyed ohmic contact to the GaN base layer underneath[75]. Accurate etching to the thin base layer can then be achieved with simple timed etches rather than with selective etches, which are required for current-generation Ga-polar devices[76]. Third, in the

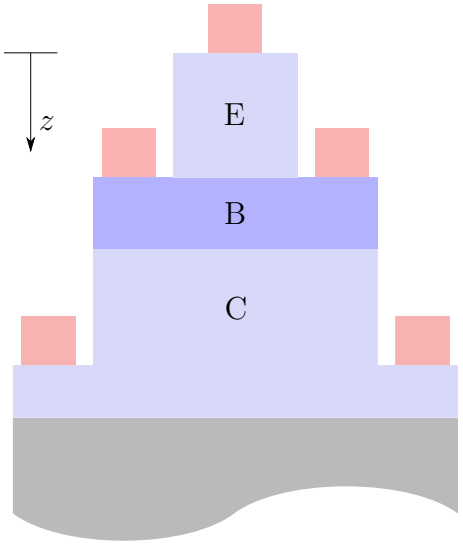

Material	thickness (nm)	doping (cm^{-3})
GaN	50	5e18
GaN	100	UID
$In_{0.12}Ga_{0.88}N$	5	UID
GaN	10	UID
$Al_{0.5}Ga_{0.5}N$	2	UID
$Al_{0.15}Ga_{0.85}N$	35	UID
grade	20	4e18
GaN	200	5e18
Buffer + Sapphire		

Figure 3.2: First generation N-polar HET layer structure and processed device schematic. The layers that compose the emitter, base and collector have been labeled and the metal contacts are pictured in red. The z-axis as it appears in Fig. 3.1 has also been labeled.

forward active mode of device bias ($V_{BE} > 0, V_{CB} > 0$), the 2DEG density increases with respect to equilibrium. This is due to electron accumulation at the AlGaN/GaN interface that results from the application of a positive bias at the collector contact. The result is that the base resistance decreases as the device is biased further into active mode rather than increasing as in Ga-polar HETs. Finally, in contrast with the current-limiting tunnel emitters used in Ga-polar HETs, the InGaN emitter diode acts as a thermionic emission barrier allowing for larger emitter current densities, which will ultimately be necessary for RF performance.

3.2 First-generation N-polar HETs

A processed device schematic and layer structure for the first-generation N-polar HET is pictured in Fig. 3.2. The device was grown by MOCVD on a 4° miscut sapphire substrate. The precise composition of the 2 nm AlGaN interlayer in Fig. 3.2 is

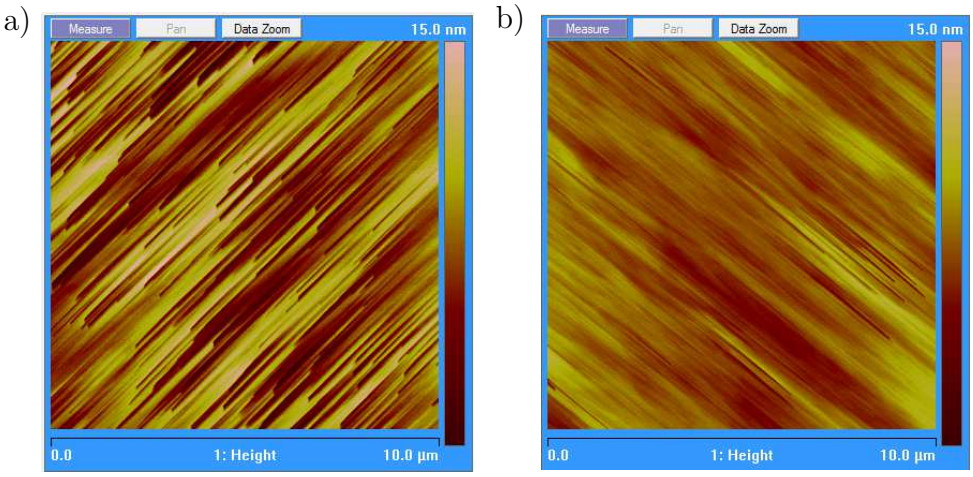

Figure 3.3: Atomic force microscope (AFM) images of the N-polar HET surface over a $10\,\mu\text{m} \times 10\,\mu\text{m}$ area. Sample (a) shows significant step bunching with rms roughness of 2.7 nm; sample (b) shows smooth surface morphology with rms roughness of 1.2 nm.

unknown, owing to the unintentional incorporation of Ga into MOCVD AlN films[77]. It is known that the surface morphology of N-polar films grown by MOCVD is highly dependent upon the epitaxial growth conditions[78, 32]. Because of the very thin layers present in the N-polar HET, it is necessary to obtain films with a root mean squared (rms) surface roughness of less than $\sim$ 2 nm over a $100\,\mu\text{m}^2$ area. This will ensure that electrical short paths cannot form between adjacent step edges. Obtaining such low surface roughness throughout a layer structure composed of both compressively and tensiley strained materials is a significant challenge. If the adatom surface mobility is too low, 3-dimensional hexagonal features tend to form[79]; if the surface mobility it too high, step bunching occurs (Fig. 3.3(a)). Therefore, to successfully grow a smooth, two-dimensional HET structure, the growth conditions must be carefully optimized to ensure intermediate adatom surface mobility throughout.

After growth the sample was processed using traditional optical lithography and reactive ion etching (RIE) with BCl_3/Cl_2 etch chemistry. First, the emitter mesa was etched to a depth of $\sim$ 20 nm above the InGaN layer. Next, the collector mesa isolation was per-

formed with a second RIE etch. Third, a series of timed RIE etches were performed using the base contact mask layer. Finally, an ohmic metal stack consisting of 30 nm/300 nm Al/Au was deposited on the emitter, base and collector using e-beam evaporation. This is the standard HET process that allows for DC measurement of device characteristics at room temperature. Because the temperature-dependent measurement setup in our lab was equipped only with ground-signal-ground (GSG) probes, several additional process steps were required to allow transistor $I - V - T$ measurements. After completing the standard process outlined above, a blanket 100 nm layer of PECVD SiO_2 was deposited. Vias were made in the oxide layer using an inductively coupled plasma (ICP) etch with CHF_3 gas. Finally, large contact pads consisting of 30 nm/200 nm Ti/Au were deposited. The complete process flow is shown in Fig. 3.4.

Previous measurements of Ga-polar III-N HETs were performed in the common-base configuration[80]. It has been demonstrated[81] that for HETs with high base resistance and large base-collector diode leakage, both common-base and Gummel measurements can yield erroneously high values of transistor gain as the base-collector diode leakage current is mistaken for hot electron current. For such a device, no clear current modulation is evident in the common-emitter configuration. A more rigorous measurement procedure consists of an initial common-emitter measurement to demonstrate transistor action and measure device current gain ($\beta = J_C/J_B$). For properly functioning devices, a subsequent measurement in the Gummel configuration should yield an identical value for β. Accordingly, we will first analyze the common-emitter characteristics of the first generation N-polar HET before moving on to Gummel measurements. It is important to demonstrate the accuracy of the Gummel measurement because, as we will see in the next section, it represents the most natural configuration for studying emitter barrier transport.

The emitter (J_E) and collector (J_C) current densities measured in the common-emitter

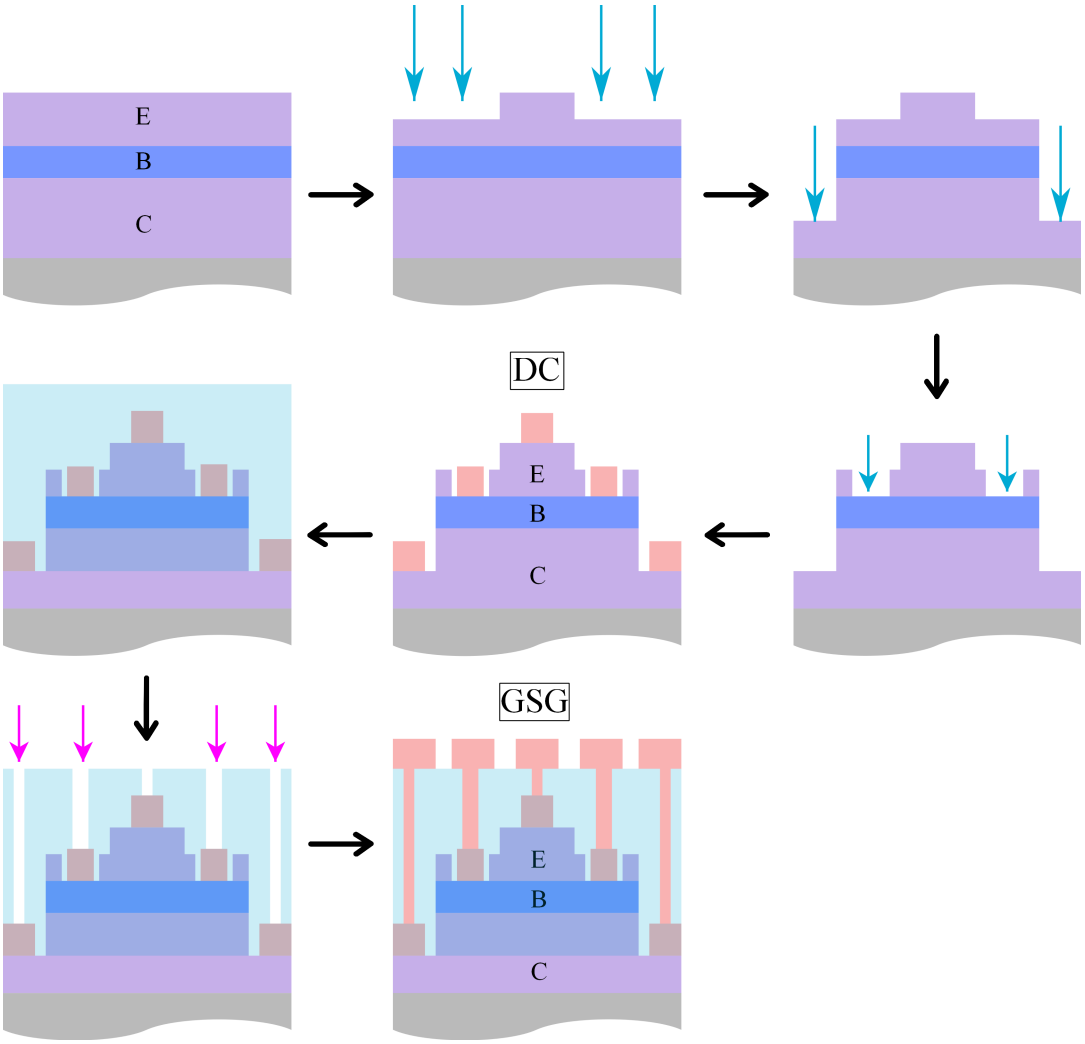

Figure 3.4: GSG-compatible N-polar HET process flow. The blue arrows represent BCl_3/Cl_2 RIE etches and the purple arrows represent CHF_3 ICP etches. Metal contacts are pictured in red. The final process step for the DC and the GSG devices have also been labeled.

configuration are shown in Fig. 3.5(a) and (b), respectively. In this configuration, the emitter terminal is grounded, a fixed base current density (J_B) is injected and the collector is swept from zero to reverse bias. The measurement is repeated for a series of prescribed base current values. The sign of the injected base current is positive, corresponding to the extraction of electrons from the base contacts. Because the transistor control element is a current rather than a voltage, for each applied collector bias (V_C), the potential in the base adjusts to maintain the prescribed base current. The voltage appearing across the emitter-base junction will, therefore, depend upon the device resistance and the current gain at each combination of J_B and V_C. This point is essential for understanding common-emitter device characteristics. We will assume that the base access resistance is very small such that the potential difference between the base contacts and the intrinsic base region is nearly zero. We will justify this assumption later in this section.

For zero base current, the potential in the base is zero. Because the emitter is also grounded, no emitter current flows. As V_C increases, the collector current remains zero until the base-collector diode begins to leak (around 4 V in Fig. 3.5(b)). The device breakdown is, therefore, determined by the ability of the collector barrier to block current in reverse bias. For nonzero base current, the intrinsic base has a positive potential with respect to ground. For $V_C = 0$, this causes both the emitter and the collector diodes to inject current into the base. However, if the collector barrier is smaller than the emitter barrier, the positive potential in the base will cause the collector to inject more current than the emitter. Thus, the required base current is supplied by the injected collector current and the emitter current remains very small. The collector current, meanwhile, is negative, corresponding to electron flow from the collector into the base.

As V_C is increased from zero, the forward bias across the base-collector diode decreases so that the magnitude of the injected collector current decreases (i.e. J_C becomes less negative). In order to maintain a constant base current, the emitter must inject more

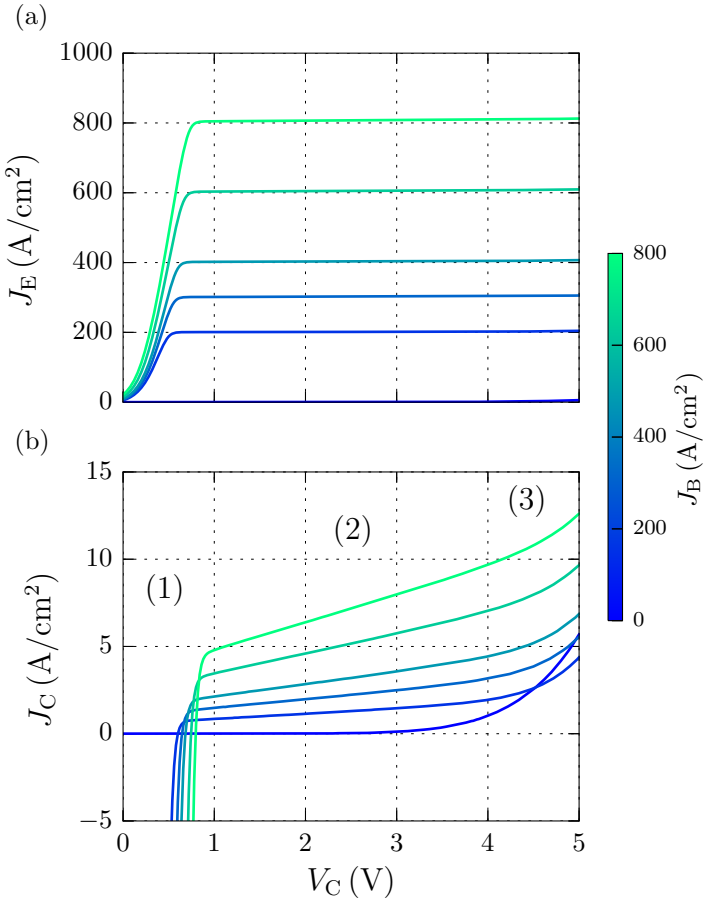

Figure 3.5: Common emitter $I - V$ characteristics for the N-polar HET at room temperature. The emitter current is shown in (a) while the collector current is shown in (b). The three regimes of transistor operation are labeled as (1) - turn-on, (2) - saturation and (3) - breakdown.

current into the base (J_E increases). This is called the turn-on region of the device (region (1) in Fig. 3.5(b)). At $V_C \sim 0.75$ V, the current injected from the collector is zero and all base and collector current is supplied by the injected emitter current. At this point, further application of V_C has little effect on J_E or J_C. This is the saturation regime of device operation (region (2)) and is the operating region of transistor amplifiers. Finally, as V_C is increased further, the base-collector diode leakage current becomes larger than the hot electron collector current and the device breaks down (region (3)).

In the saturation region ($1\,\mathrm{V} < V_C < 4\,\mathrm{V}$), J_E and J_C are nearly, but not exactly, constant. For ideal transistors, the emitter and collector regions are completely decoupled from one another and the saturation currents are flat. The nonzero slope of the saturation current present in real devices is called output conductance and is a measure of the coupling of the emitter and collector terminals. This coupling is undesirable because it reduces the voltage gain of the device. In bipolar transistors, output conductance is caused by modulation of the base-collector depletion region width, which leads to base width narrowing[68]. This, in turn, causes an increase in emitter current in order to satisfy the boundary conditions on the diffusion charge in the base. By contrast, output conductance in the HET is caused primarily by the bias-dependent transfer characteristics of the collector barrier. As the collector is reverse biased, it becomes more transparent to incoming hot electrons. Therefore, increasing the collector bias causes an increase in the current transfer ratio (α) and, therefore, β. Because fewer electrons are reflecting off the collector and contributing to base current, the emitter must inject more current to maintain constant base current. By this mechanism, increasing V_C leads to increases in J_E, J_C and α.

To demonstrate this effect, we will calculate the transfer ratio of the collector barrier for various values of V_C using the techniques outlined in Chapter 2. The calculation proceeds as follows: first, for each collector bias and corresponding band diagram

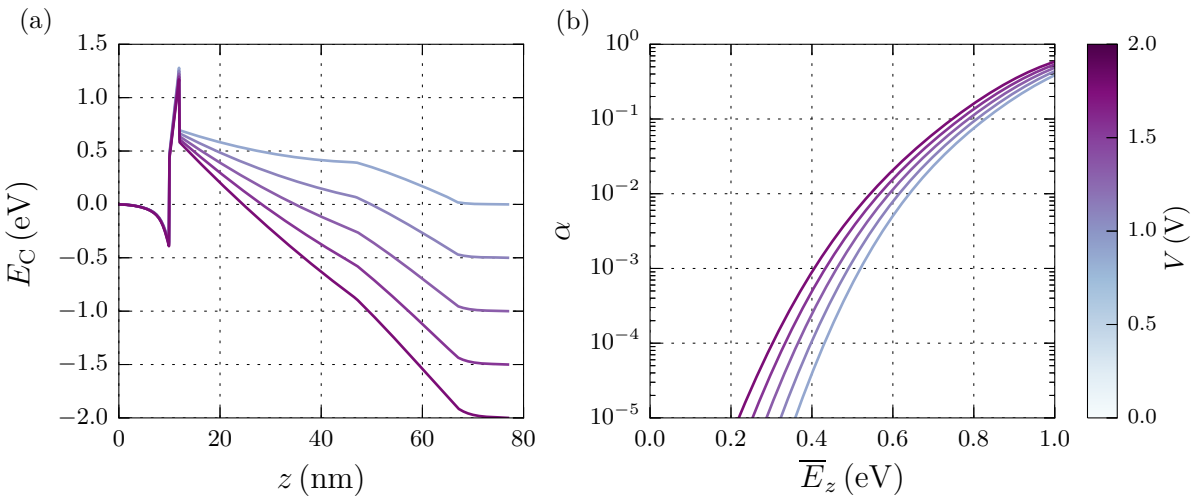

Figure 3.6: (a) Collector barrier conduction band diagrams for base-collector reverse biases of $0-2$ V. (b) Simulated transfer ratios for a Gaussian packet of electrons with mean arrival energy $\overline{E}_z$. For a given arrival energy, which is fixed by the injection energy and the base width, the barrier becomes more transparent with increasing collector bias and α increases.

(Fig. 3.6(a)), the energy-dependent transmission probability ($\widetilde{T}(E_z)$) is calculated via the QTBM method. Second, because the electrons arriving at the collector are not monoenergetic, a mean energy ($\overline{E}_z$) is chosen and a normalized Gaussian distribution ($P(\overline{E}_z, E_z)$) of electron energies is populated around the mean. The width of the distribution is equal to the full width at half maximum of the corresponding Fermi-Dirac function ($\sim 0.03\,\text{eV}$ at room temperature). The transfer ratio at each $\overline{E}_z$ is then calculated via

$$\alpha(\overline{E}_z) = \int P(\overline{E}_z, E_z)\widetilde{T}(E_z)\mathrm{d}E_z. \tag{3.1}$$

The simulated function $\alpha(\overline{E}_z)$ is pictured in Fig. 3.6(b). The transfer ratio increases with $\overline{E}_z$ as expected. Furthermore, for a constant $\overline{E}_z$, α increases with collector bias, which causes nonzero output conductance via the mechanism discussed earlier.

For the real device, the common-emitter current transfer ratio was measured to be $\alpha = 3.88 \times 10^{-3}$ for a drive current of $J_B = 200\,\text{A/cm}^2$ and $V_C = 0.8\,\text{V}$. The DC current

gain was $\beta = \frac{\alpha}{1-\alpha} = 3.9 \times 10^{-3}$. While these values are very low and must be improved upon, this device represents the first demonstration of common-emitter modulation in an N-polar III-N HET. The main cause of low β in this device is the large base-collector barrier, which reflects the vast majority of incoming hot electrons. From Fig. 3.6(b), $\alpha \sim 0.004$ corresponds to a mean arrival energy of about $0.5 - 0.6$ eV. To achieve current gain ($\beta > 1$) with this collector barrier, we must achieve $\alpha > 0.5$ or an arrival energy of about 1 eV.

To confirm our results, we performed an additional measurement in the Gummel configuration: the base and collector were grounded while a negative bias was applied to the emitter. The resulting base and collector currents were then measured (Fig. 3.7). Both the base and collector currents rise with emitter forward bias (V). Ohmic voltage drops become significant for applied biases in excess of ~ 0.9 V, beyond which the rate of increase of J_{B} with V slows dramatically. These resistive voltage drops ultimately limit the achievable injection current density in the HET. To compare the current gain measured in the Gummel configuration with common-emitter, the bias point $V = 1.0$ V was chosen. This bias corresponds to the base current ($\sim 200\,\mathrm{A/cm^2}$) that was used in the common-emitter extraction of β. At 1 V, $\beta = 4.2 \times 10^{-3}$, very similar to the value extracted from common-emitter measurements.

The contacts to the highly-scaled based layer were characterized via the transfer length method (TLM) and the results appear in Fig. 3.8. The contacts are ohmic and the contact and sheet resistances are $0.34\,\Omega \cdot \mathrm{mm}$ and $517\,\Omega/\square$, respectively. These are excellent values for unalloyed, unoptimized base contacts, and they demonstrate the promise of N-polar HETs for achieving ultralow contact resistance to a highly scaled base layer. This measurement allows us to revisit our earlier claim that the voltage drop between the base contacts and the intrinsic base region is nearly zero. Given the values of R_{c} and R_{sheet} as well as the device geometry, the voltage drop in the base extrinsic

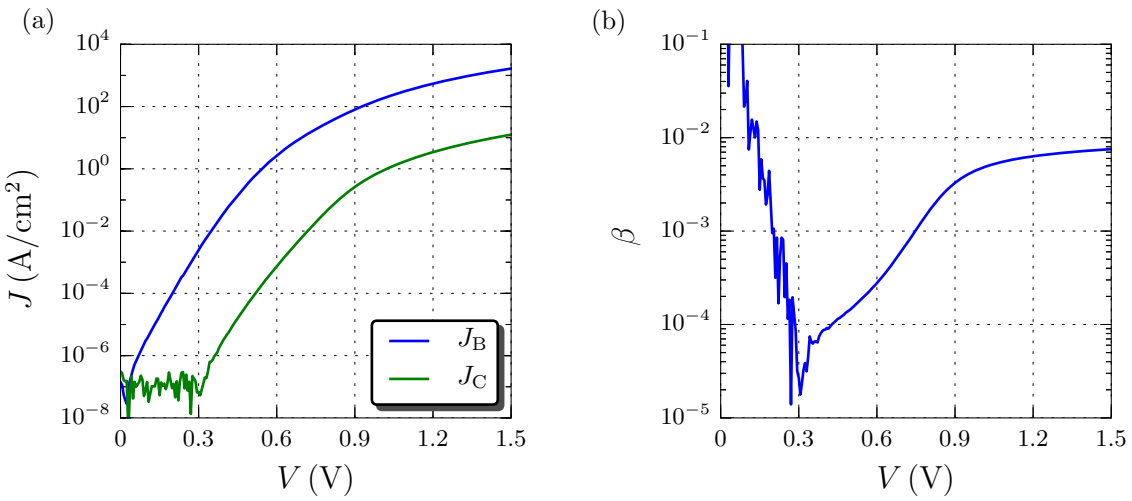

Figure 3.7: (a) Gummel $I-V$ characteristics for the first generation N-polar HET at room temperature. (b) Current gain ($\beta = J_C/J_B$) calculated from (a). The noisy data for $V < 0.3$ V is due to the collector current noise in (a).

regions is calculated to be ~ 0.003 V for an emitter-base bias of 1.25 V (see Appendix B for details regarding the calculation). This value of emitter-base voltage corresponds to the maximum J_B in common-emitter measurements and, therefore, represents the largest possible extrinsic voltage drop. The very small value of the extrinsic base resistance ($1.56\,\Omega$) demonstrates that the base contacts have a negligible effect on transistor $I-V$ characteristics.

Summarizing our results to this point, we have demonstrated the first N-polar III-N HET with common-emitter transconductance. The large base-collector barrier reflects most of the incoming hot electrons resulting in very low current gain ($\beta = 0.004$). However, the base-collector diode has fairly low leakage and the base access resistance is very low. Therefore, it is possible to obtain accurate values for the current gain and transfer ratio from Gummel $I-V$ characteristics without the corrupting effects of erroneous leakage currents. The N-polar HET must be improved dramatically before it can become a viable transistor technology. However, these first-generation devices can already

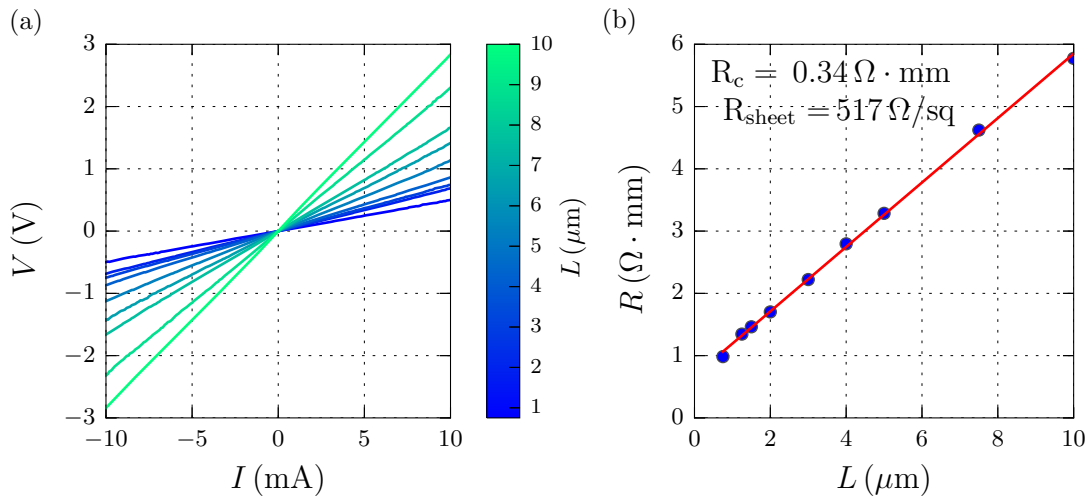

Figure 3.8: Base layer TLM measurements of the first-generation HET. (a) Ohmic $V - I$ behavior is seen for all TLM spacings. (b) The contact and sheet resistances are found to be $0.34\,\Omega \cdot \text{mm}$ and $517\,\Omega/\square$, respectively.

be used to study fundamental transport physics in III-N heterostructures. Such studies have important materials science implications, as we will see in the next section.

3.3 InGaN polarization dipole barrier transport

We turn our attention now to an investigation of the N-polar HET emitter barrier. The goals of this analysis are two-fold: from a scientific perspective, we hope to leverage the capability of the collector barrier as an analyzer of hot electron states to study emitter barrier transport; from a technological perspective, we would like to determine the effects of nonideal emitter characteristics on transistor performance. We will begin this section by discussing two-terminal InGaN polarization dipole diode (PDD) characteristics. Then, we will present transistor measurements as a way to fortify the conclusions drawn from the diode analysis.

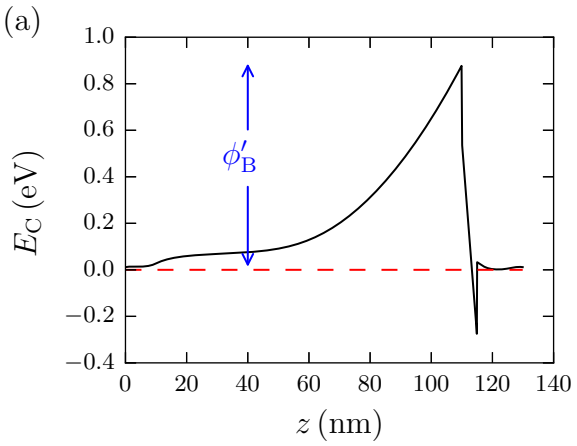

(b)

Material	thickness (nm)	doping (cm^{-3})
GaN	50	5e18
GaN	100	UID
$In_{0.1}Ga_{0.9}N$	5	UID
GaN	200	5e18
Buffer + Sapphire		

Figure 3.9: (a) Conduction band diagram of the InGaN PDD. The apparent barrier height (ϕ'_B) is labeled along with the zero bias Fermi level (dashed red line). (b) PDD layer structure with z-axis orientation as it appears in (a).

3.3.1 InGaN polarization dipole diode analysis

The InGaN PDD used in this study was designed to closely mimic the emitter barrier that appears in the N-polar HET. The conduction band diagram and layer structure are shown in Fig. 3.9. The PDD was grown by MOCVD on a miscut sapphire substrate and was fabricated using a truncated version of the process shown in Fig. 3.4 (BCl_3/Cl_2 mesa isolation and Al/Au ohmic contacts).

During measurement, the diode was placed in a vacuum chamber and brought to target temperatures in the range $100 - 400$ K using a Lake Shore 330 model temperature controller with a PID feedback loop. Temperatures below ambient were achieved using liquid nitrogen as a cooling agent. At each target temperature, the sample was left for $10 - 15$ minutes before measurements were made to ensure thermal equilibrium was achieved between the device and the sample stage. Then, the top contact was grounded and the voltage on the bottom contact swept from -3 V to $+3$ V while measuring the current.

The InGaN emitter diode $I - V - T$ characteristics are shown in Fig. 3.10. At

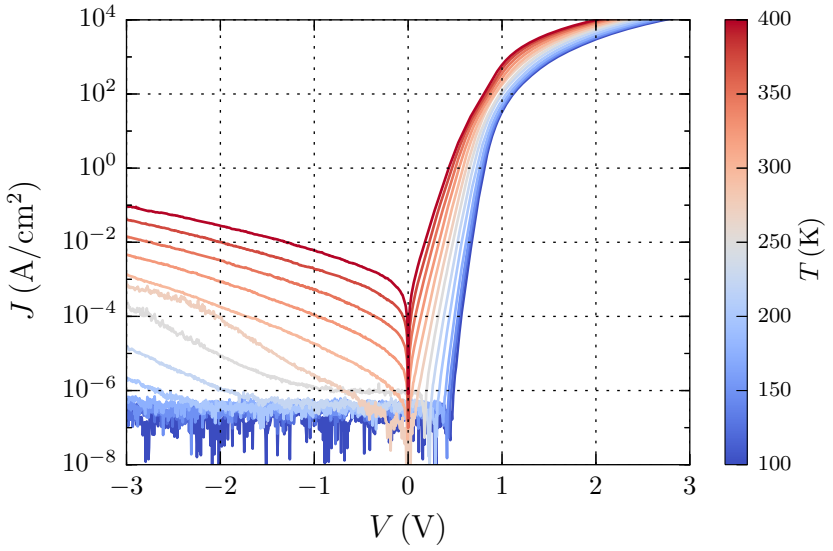

Figure 3.10: $I-V-T$ data for the InGaN polarization dipole diode for the temperature range $100-400$ K. Ohmic voltage drops limit the achievable current density beyond 1 V applied bias. The linear fits to the forward bias current are performed within the first 200 mV of device turn-on.

low bias the current increases quasi-exponentially for all temperatures. For an applied forward bias of about 1 V, the current begins to saturate as ohmic voltage drops become appreciable. The device turn-on voltage decreases with increasing temperature, a result of the increased supply of high-energy electrons incident on the barrier at high temperature. While the turn-on voltage increases at low temperatures, it remains less than 0.5 V at 100 K, nearly half of the design barrier height of ~ 0.9 eV (see Fig. 3.9(a)). This suggests the presence of an unknown, low-energy current pathway that dominates low-temperature transport.

Following the procedure outlined in Chapter 2, a linear fit to the low-bias forward current at each temperature is performed. The slope of this linear fit is $q/nk_{\mathrm{B}}T$ and the intercept is $\ln(J_{\mathrm{S}})$, where J_{S} is the saturation current. Assuming $A^* = 26\,\mathrm{A/cm^2K^2}$ allows us to calculate the apparent barrier height (ϕ'_{B}) from J_{S} while the ideality factor (n) is calculated from the slope. This procedure is done for both the experimental data

pictured in Fig. 3.10 and for simulated $I-V-T$ curves generated using the band diagram in Fig. 3.9(a) and the methods outlined in Chapter 2. The results for the simulated and experimental ideality factors and apparent barrier heights are pictured in Fig. 3.11.

The high-temperature ideality factor for the simulated diode current is ~ 1.2. There are two contributions to $n > 1$ in the simulated data: first, voltage partitioning ensures that only a fraction of the applied bias is dropped in the UID GaN above the InGaN layer. The remainder appears across the InGaN dipole layer, which causes the barrier height to increase with bias. This effect is due to simple electrostatic considerations and is present whenever the barrier maximum is not immediately adjacent to the control electrode. In particular, if the barrier maximum is a distance t_2 away from the control electrode and t_1 away from the grounded electrode, the ideality factor attributed to voltage partitioning is:

$$n_V = 1 + \frac{t_2}{t_1}\frac{\epsilon_1}{\epsilon_2}, \tag{3.2}$$

where ϵ_i is the low-frequency dielectric constant in the ith material. In the PDD, t_1 = 100 nm and t_2 = 5 nm so that $n_V \sim 1.05$. Voltage partitioning can also arise from resistive access regions and barrier-limited contacts. However, these contributions can be shown to be negligible for the very small currents considered here.

The second contribution to $n > 1$ in the simulated data is thermionic field emission (see Chapter 2 for a detailed discussion). Note that the background doping is relatively high in N-polar GaN ($\sim 2 \times 10^{17}\,\mathrm{cm}^{-3}$). This leads to increased band bending and, therefore, a larger thermionic field current than in Ga-polar devices. The ideality factor due to thermionic field emission is $n_{\mathrm{TFE}} \sim 1.14$. The combined effect of voltage partitioning and thermionic field emission is given by the product of the ideality factors: $n_V \times n_{\mathrm{TFE}} = 1.2$, the total high-temperature ideality factor. Voltage partitioning and thermionic field emission are also present in real PDD devices. However, the simulation,

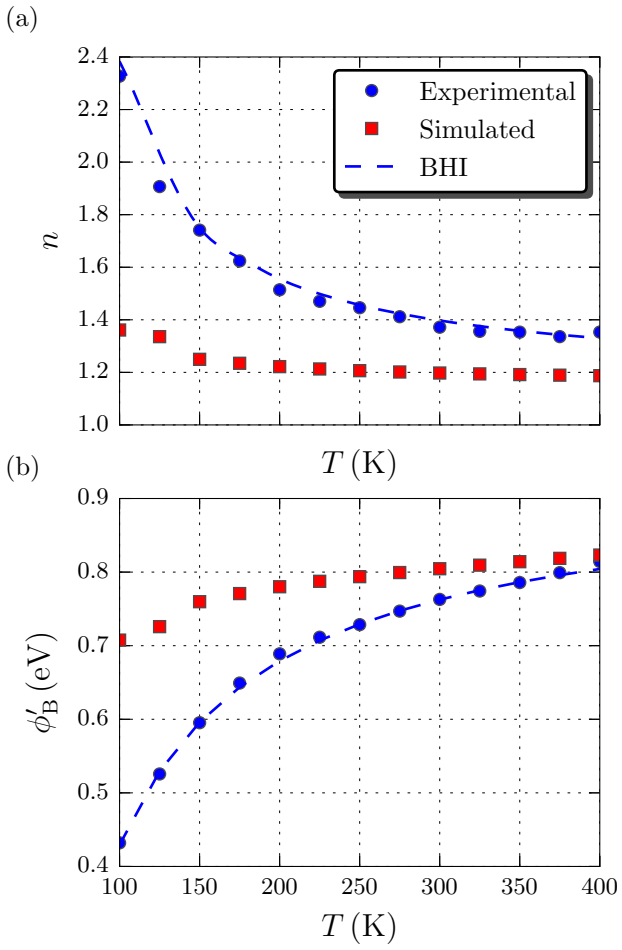

Figure 3.11: Simulated and experimental values of (a) the ideality factor and (b) the apparent barrier height. The latter were calculated using $A^* = 26\,\mathrm{A/cm^2K^2}$. Theoretical and experimental values begin to converge at high temperatures but diverge as the temperature decreases. The dashed blue line in (a) represents the product of the BHI contribution to n (Eq. (3.3)) and the simulated values. The dashed blue line in (b) represents Eq. (3.4) with the values of $\overline{\phi}_B$ and σ_S taken from the second-order fit in Fig. 3.12.

which takes into account only these two effects, produces ideality factors that are smaller than experimental values. Therefore, there must be an additional source of $n > 1$ in real PDDs.

Similarly, the simulation overestimates the value of ϕ'_{B}. Thermionic field emission causes ϕ'_{B} to increase with temperature but at a slower rate than the experimental values. Like the Schottky diode in Chapter 2, the simulated and experimental values of ϕ'_{B} match well at high temperatures but diverge at low temperatures. The Richardson plot (Fig. 3.12) reveals a similar relationship between simulated and experimental results.

These discrepancies can be clearly explained by barrier height inhomogeneity (BHI) in the InGaN PDD. The deviation of the low-bias current from perfect linearity in Fig. 3.10 is characteristic of inhomogeneous barrier transport[82]. A detailed discussion of the effects of BHI on measured diode characteristics can be found in Chapter 2. Here we summarize the important results:

1. Upon application of forward bias, the inhomogeneous barrier distribution is distorted and the mean barrier height increases causing $n > 1$. The temperature and bias dependence of n is given by

$$n = \left(1 - \frac{q}{2k_{\mathrm{B}}T}\frac{\sigma_{\mathrm{S}}^2(0) - \sigma_{\mathrm{S}}^2(V)}{V}\right)^{-1}. \tag{3.3}$$

2. For a Gaussian distribution of barrier heights, the canonical thermionic emission equation remains valid if we substitute an apparent barrier height,

$$\phi'_{\mathrm{B}} = \overline{\phi}_{\mathrm{B}} - \frac{q\sigma_{\mathrm{S}}^2}{2k_{\mathrm{B}}T}, \tag{3.4}$$

for the constant quantity ϕ_{B}. In Eq. (3.4), $\overline{\phi}_{\mathrm{B}}$ is the mean, zero-bias barrier height and σ_{S} is the zero-bias standard deviation of the barrier distribution.

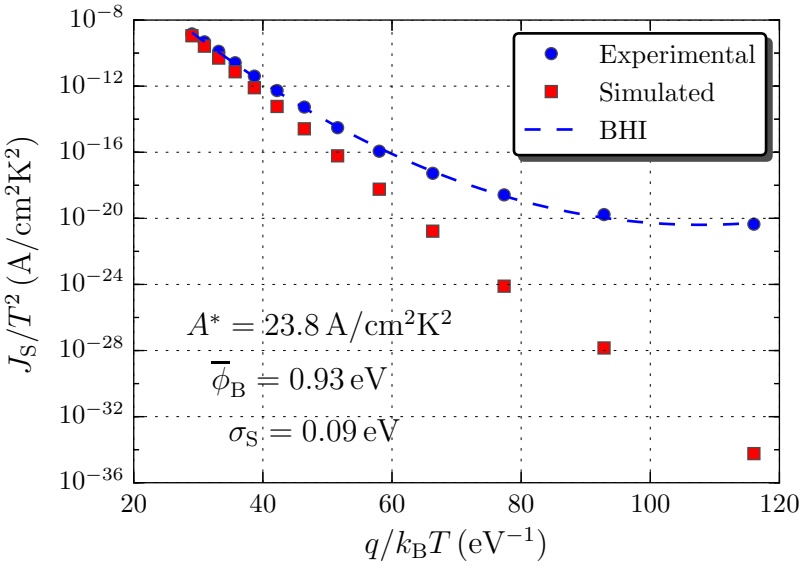

Figure 3.12: (a) Simulated and experimental Richardson plot for the PDD. The values of A^*, $\overline{\phi}_\mathrm{B}$ and σ_S are extracted from the quadratic fit (dashed blue line) to the experimental Richardson data via Eq. (3.5).

3. The Richardson data are no longer linear but obey the quadratic equation:

$$\ln\left(\frac{J_\mathrm{S}}{T^2}\right) = \ln(A^*) - \left(\frac{q}{k_\mathrm{B}T}\right)\overline{\phi}_\mathrm{B} + \frac{1}{2}\left(\frac{q}{k_\mathrm{B}T}\right)^2\sigma_\mathrm{S}^2. \tag{3.5}$$

For diodes containing inhomogeneous barriers, a second-order fit to the Richardson data simultaneously yields A^*, $\overline{\phi}_\mathrm{B}$ and σ_S from the zeroth, first and second order coefficients, respectively. The fit is performed on the PDD Richardson data and is shown in Fig. 3.12 (dashed blue line). The extracted value $A^* = 23.8\,\mathrm{A/cm^2K^2}$ is nearly equal to the theoretical value of 26 $\mathrm{A/cm^2K^2}$ for GaN, a confirmation that the BHI model accurately describes the transport physics of the diode. Furthermore, $\overline{\phi}_\mathrm{B}$ is almost exactly equal to the design barrier height in Fig. 3.9(a). The standard deviation of the barrier height fluctuations (σ_S) amounts to a ~10% lateral variation in barrier height across the device area.

The dashed line in Fig. 3.11(b) represents Eq. (3.4), with the values of $\overline{\phi}_{\mathrm{B}}$ and σ_{S} taken from the second-order fit coefficients according to Eq. (3.5). The experimental data are well-described by the dashed line, confirming the accuracy of the functional form of Eq. (3.4). The dashed line in Fig. 3.11(a) is generated by multiplying the BHI contribution to n given by Eq. (3.3) with the simulated values; we find excellent agreement between this line and the data. If only the BHI contribution is considered, calculated values of n do not agree with experimental values. This strongly suggests that three entirely distinct effects contribute to the experimental ideality factor: voltage partitioning, thermionic field emission and barrier height inhomogeneity. The analysis we have presented demonstrates that these three effects can be "factorized" and their magnitudes separately determined with the help of numerical $I-V-T$ simulations.

For high temperatures, the quadratic term in Eq. (3.5) becomes small and the data are approximately linear in powers of $q/k_{\mathrm{B}}T$. This is consistent with the commonly observed linearity of high-temperature Richardson data. As such, it may be tempting to perform a linear fit to the high-temperature data in order to extract A^* and ϕ_{B}. To demonstrate the limits of this method, we performed such a fit on the high-temperature data in Fig. 3.12. The fit yields a value for A^* and ϕ_{B} of 0.13 A/cm^{2}K^2 and 0.63 eV, respectively. This underestimation of the Richardson constant and the barrier height from a high-temperature linear fit was observed in a previous report of InGaN LED data[83]. These results suggest that the homogeneous thermionic emission equation does not capture all the relevant physics in our devices, even at high temperature where the data appear to be linear.

We propose that the physical origin of the lateral barrier height fluctuations observed in the PDD is random, nanoscale fluctuations in indium composition. Indium fluctuations as high as $25-50\%$ of the nominal alloy composition have been observed in InGaN films using atom probe tomography[84, 85, 86]. Other studies have linked compositional

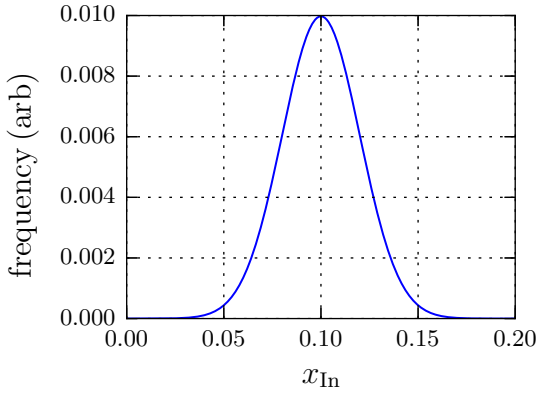

Figure 3.13: Distribution of In compositions corresponding to the measured value $\sigma_{\mathrm{S}} = 0.09\,\mathrm{eV}$.

fluctuations with the anomalously low turn-on voltage observed in multiquantum well LEDs[87, 83].

For the device structure pictured in Fig. 3.9, the extracted σ_{S} corresponds to a compositional standard deviation of only 2% In across the device area. A Gaussian distribution with a mean In composition of 10%, the nominal design composition, and a standard deviation of 2% is shown in Fig. 3.13. The distribution reveals that there is a nonzero proportion of the device area locally containing no more than 5% In. For the PDD in this study, this composition corresponds to a barrier height of 0.44 eV, nearly identical to the value of ϕ'_{B} at 100 K (see Fig. 3.11(b)). This confirms the assertion that inhomogeneous barrier transport, particularly at low temperature, is dominated by low-barrier regions and further implicates In compositional fluctuations as the physical source of BHI. Furthermore, there is no evidence of In clustering[88, 89] or phase segregation in the dipole layer of our device. Such an effect would imply the existence of regions where the local In composition is nearly zero. These regions would provide low-resistance short paths through the barrier that would become clearly evident at low temperature. The fact that the diode exhibits signatures of barrier-limited transport even at 100 K

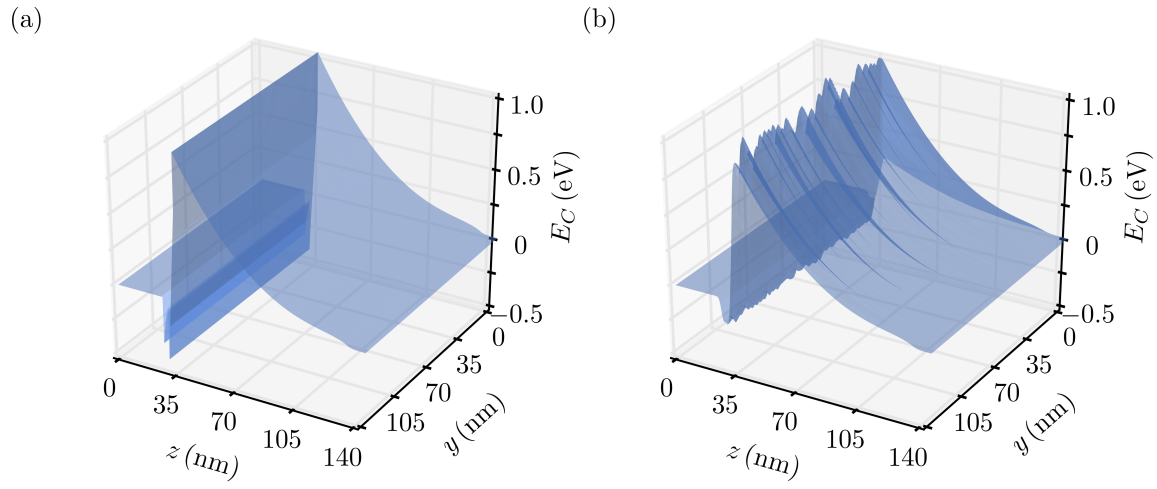

Figure 3.14: 3-dimensional schematic of the conduction band diagram for a laterally (a) homogeneous and (b) inhomogeneous InGaN PDD with $\sigma_S = 0.09\,\text{eV}$.

suggests that the local In composition does not fall to zero. A 3-dimensional schematic of a homogeneous and inhomogeneous InGaN PPD with $\sigma_S = 0.09\,\text{eV}$ is pictured in Fig. 3.14.

In this section we have shown that BHI theory can accurately explain the transport characteristics of the InGaN PDD. Simulation data suggest that voltage partitioning and thermionic field emission, while clearly present in the real device, cannot fully account for the observed experimental data. Despite the seeming success, so far we have relied only on diode data and have no independent demonstration that BHI is the cause of the anomalous diode $I - V$. As such we would like to test the predictions of BHI theory, specifically that lateral fluctuations produce a bias and temperature-dependent apparent barrier height. For that we turn to temperature-dependent transistor measurements, which are discussed in the next section.

3.3.2 Electron injection spectroscopy using the N-polar HET

While the BHI model seems to accurately describe the PDD data, a direct correlation between ϕ'_B and the electron injection energy has not yet been established. In fact, researchers routinely refer to ϕ'_B as the "apparent barrier height"[90, 91, 92], a name that reveals the uncertainty regarding its physical interpretation. Simply put, we seek to answer the question: "is ϕ'_B equal to the average energy of electrons emitted from the diode?". The answer to this question will have important device implications for III-N HETs. In this section we introduce a method called electron injection spectroscopy, which provides a direct measurement of the signature of BHI by using the collector barrier of the HET as an analyzer of hot electron states. Such a measurement will demonstrate the effects of BHI on transistor performance and will help provide a physical interpretation of ϕ'_B.

To date the most popular method for directly measuring BHI and its effect on localized band structure is ballistic electron emission microscopy (BEEM)[93, 94]. In this method a scanning tunneling microscope (STM) tip serves as the emitter of ballistic electrons into a very thin base provided by the Schottky metal while the semiconductor material serves as the collector. By varying the injection energy of the ballistic electrons and measuring the resulting collector current, the local barrier height can be determined with a lateral resolution of $\sim$1 nm. This method has been applied to study BHI in a wide variety of Schottky junctions[95, 96, 97] and semiconductor heterointerfaces[98, 99].

While BEEM methods are sensitive to the effects of BHI on ballistic electrons, which are out of equilibrium with the semiconductor lattice, the first comprehensive theory describing the effects of BHI on the transport properties of thermalized electrons was proposed by Tung[73]. In Chapter 2 we demonstrated that in the presence of BHI, the constant barrier height in the canonical thermionic emission equation must be replaced

with a bias and temperature-dependent barrier height ($\phi_B \rightarrow \phi'_B(V,T)$):

$$J = A^* T^2 \exp\left(-\frac{q\phi'_B(V,T)}{k_B T}\right)\left(\exp\left(\frac{qV}{k_B T}\right) - 1\right). \tag{3.6}$$

Specifically, ϕ'_B increases with both increasing temperature (see Fig. 3.11(b)) and increasing forward bias. If such a barrier is placed in a HET where it emits electrons toward an analyzer provided by the collector barrier, relative changes in the electron injection energy will reveal themselves as changes in the current transfer ratio α. In particular, as the injection energy increases the probability of transmission at the collector, and therefore α, increases. Because the injection energy is determined by the emitter barrier height, changes in α are correlated with changes in ϕ'_B.

The layer structure of the HET used in this study was identical to the device pictured in Fig. 3.2 except that the GaN base layer thickness was 3 rather than 10 nm. This device was chosen in order to minimize electron scattering events in the base and simplify the analysis. The growth and processing details were also identical. During measurement the HET was placed in a vacuum chamber whose sample stage was cooled with liquid nitrogen. At each target temperature, the transistor was measured in the modified Gummel configuration: the base and collector terminals were grounded while a forward bias (V) was applied to the emitter. In this configuration there was no bias applied between the base and the collector so that the quantum mechanical transfer characteristics of the collector remained constant for all emitter biases and temperatures. In this sense the electron "filter" was kept constant. The applied forward bias was swept between $0 - 1.5$ V and the emitter and collector currents were measured. Because we were ultimately interested in the transfer ratio J_C/J_E, the Gummel plot has been modified to display J_E and J_C rather than J_B and J_C, which appear in conventional Gummel plots.

The modified Gummel plot for the III-N HET in the temperature range $100 - 400$

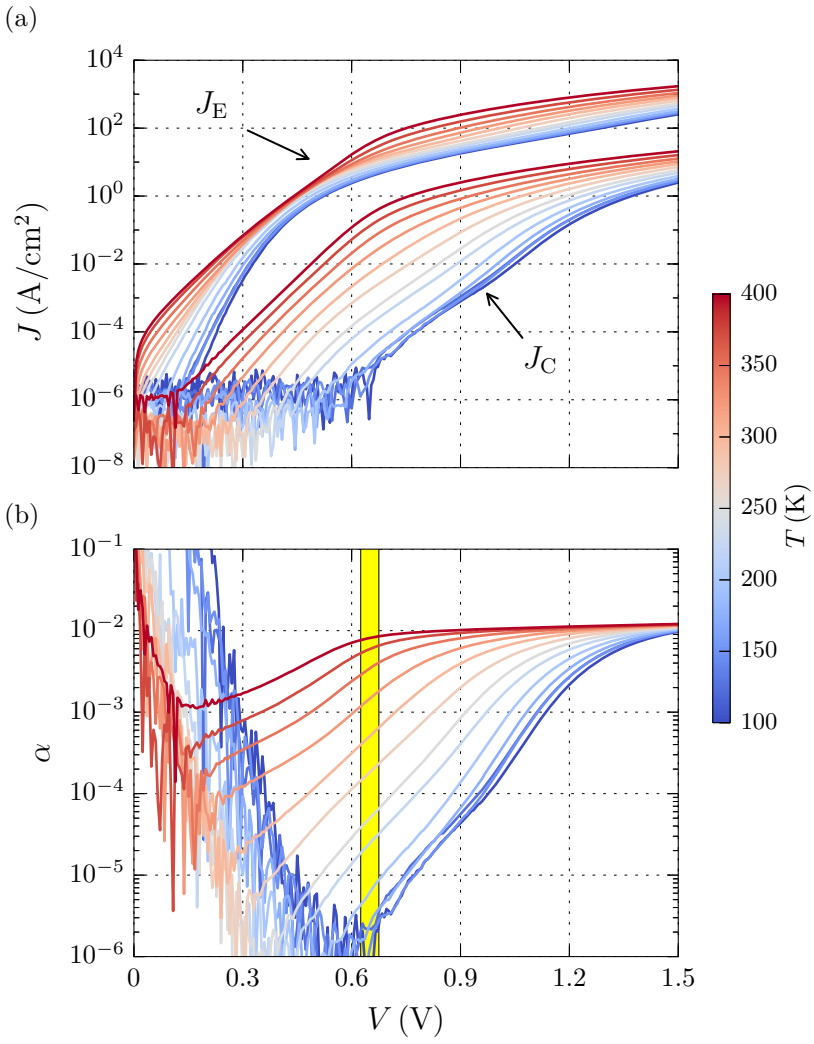

Figure 3.15: (a) Modified Gummel $I-V$ characteristics for the bias and temperature range $0-1.5$ V and $100-400$ K, respectively. The arrows label each family of curves representing the temperature series for J_E and J_C. (b) Corresponding transfer ratio ($\alpha = J_C/J_E$) for the same temperature and bias range. The yellow box indicates the values of α plotted in Fig. 3.16(a).

K is shown in Fig. 3.15(a). The emitter and collector currents both rise with emitter forward bias, and, because the collector barrier is large, $J_E \gg J_C$. Ohmic voltage drops become significant for applied biases in excess of $\sim$ 0.75 V, beyond which the $I - V$ curves in Fig. 3.15(a) flatten. These ohmic voltage drops ultimately limit the achievable intrinsic emitter forward bias and the magnitude of J_E. Furthermore, in these ohmic regions some portion of the applied voltage drops in the extrinsic regions of the device making it difficult to determine the precise intrinsic emitter bias accurately. Therefore, we will restrict the subsequent analysis to $V < 0.75$ V. The collector current resolution is limited by the instrument noise floor as well as the zero bias current noise at each temperature.

The bias and temperature-dependent current transfer ratio is pictured in Fig. 3.15(b). For a single temperature, between the voltages corresponding to the noise floor and to the point where ohmic voltage drops become significant, α exhibits a clear upward trend with bias. Additionally, for a fixed applied bias, α increases with increasing temperature (Fig. 3.16(a)). The applied bias value of 0.65 V was chosen for Fig. 3.16(a) because at this value, ohmic voltage drops are negligible and collector current noise is limited for most temperatures (see yellow box in Fig. 3.15(b)). This ensures that nearly all of the applied bias appears across the intrinsic emitter-base junction for all temperatures. At 0.65 V and $T < 200$ K the collector current, and therefore α, becomes noisy. Therefore, the data below 200 K in Fig. 3.16(a) are likely unreliable.

Because the quantum mechanical transfer characteristics at the base-collector junction are constant for all emitter biases and temperatures, an increase in α can only result from a corresponding increase in electron injection energy. This, in turn, can only be explained by an increase in the mean emitter barrier height with bias and temperature. As we will see in Chapter 5, the hot electron mean free path in GaN was measured to be $\sim$ 10 nm. Because the base in the III-N HET is 8 nm thick (5 nm InGaN + 3 nm GaN), electron

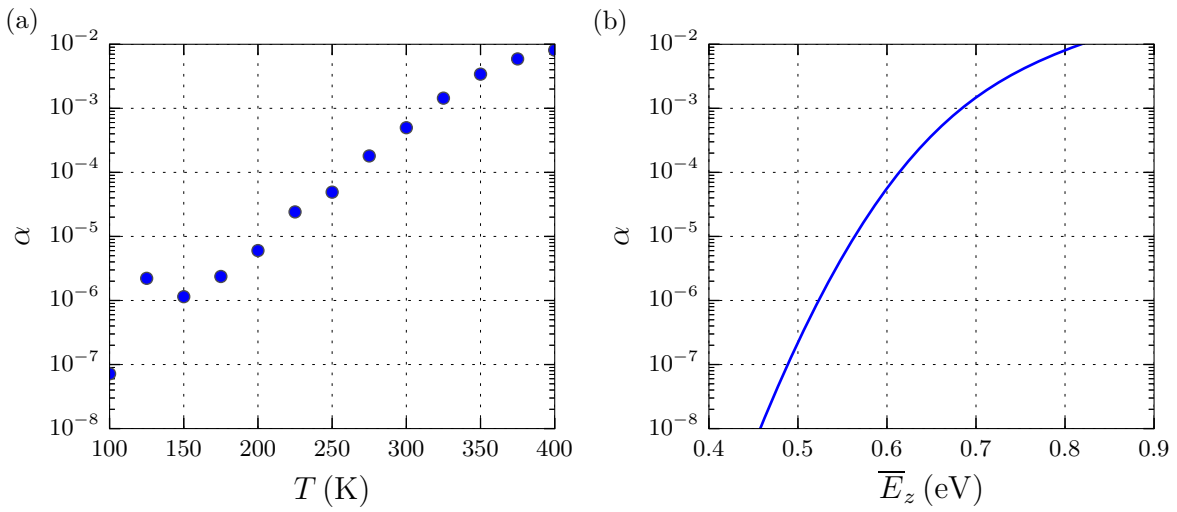

Figure 3.16: (a) Experimental transfer ratio at an emitter bias of 0.65 V for the temperature range $100 - 400$ K. These values are represented by the yellow box in Fig. 3.15. (b) Simulated transfer ratio for a Gaussian distribution of electrons with mean longitudinal energy $\overline{E}_z$. The experimental values in (a) are mapped onto the simulated values in (b). This mapping enables an estimate of the mean energy of the hot electron ensemble incident on the collector barrier at each temperature (see Fig. 3.17).

scattering in the base should be minimized. In this quasi-ballistic regime, the number of scattered electrons is a very weak function of injection energy and temperature. This ensures a close correspondence between increases in α and increases in emitter barrier height.

To further reinforce this correspondence, the energy-dependent transfer ratio for the AlGaN collector barrier was calculated. The details of the calculation were discussed earlier in this chapter (see Eq. (3.1)) and the results are pictured in Fig. 3.16(b). This calculation provides a one-to-one relationship between the transfer ratio and the mean kinetic energy of electrons arriving at the collector. Considering Fig. 3.16(a) and (b) together allows us to estimate the mean arrival energy of electrons in the HET we have measured. The temperature-dependent arrival energies and apparent emitter barrier height, as measured from emitter diode $I - V - T$, are pictured in Fig. 3.17.

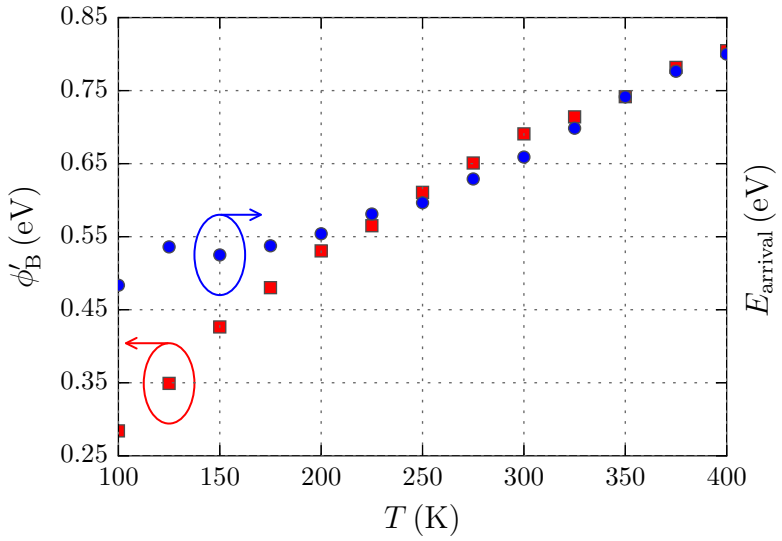

Figure 3.17: Apparent barrier height of the emitter diode (red squares) and electron arrival energies corresponding to the measured transfer ratios in Fig. 3.16(a)(blue dots). For $T > 200$ K, these two quantities are nearly equal, confirming both that the increase in α is due to the increase in ϕ'_B and that the base electrons travel ballistically.

There are two important observations and accompanying conclusions to make about Fig. 3.17: first, the values ϕ'_B and $E_{arrival}$ increase with temperature at identical rates above 200 K. This implies that the increase in α is indeed due to an increasing emitter barrier height caused by BHI. This trend also suggests that the apparent barrier height is approximately equal to the mean electron injection energy. In other words ϕ'_B has a clear and direct physical meaning and need not be considered an "apparent" quantity. Second, ϕ'_B and $E_{arrival}$ are nearly equal above 200 K. This implies that the average hot electron kinetic energy on the emitter and the collector side of the base are equal and that electron transport across the base is, therefore, ballistic.

These trends do not hold at the lowest temperatures. The apparent barrier height continues to fall with temperature while the estimated arrival energy remains constant. This is likely due to the current noise floor of the measurement apparatus as discussed earlier. Namely, the low temperature transfer ratios are likely unreliable due to collector

current noise. The arrival energies at low temperature are, therefore, similarly unreliable.

In the previous section, we proposed alloy fluctuations as the most likely cause of the observed BHI in InGaN PDDs. Despite the likely existence of such compositional fluctuations, several additional physical sources of barrier height inhomogeneity can be proposed. Because the polarization dipole barrier height is determined both by the In composition and the InGaN thickness, thickness fluctuations of ≤ 1 nm can provide the necessary σ_S. Scanning capacitance microscopy measurements of MOCVD-grown 3 nm InGaN/GaN quantum wells have revealed InGaN thickness fluctuations of several monolayers[100]. Barrier height fluctuations could also result from an inhomogeneous distribution of conductive threading dislocations that provide a low-energy current pathway though the band gap. The magnitude of leakage currents has been observed to scale with threading dislocation density in LEDs [101, 102] and in GaN Schottky diodes[103]. While it is difficult to diagnose the exact physical cause of BHI from a single device, these analysis methods can be applied to a series of InGaN PDDs designed to test each of the above hypotheses.

The analysis presented in this chapter has several important implications for the HET: first, the presence of lateral barrier height fluctuations results in a lower average electron injection energy than the design barrier would suggest. This means that we have been unable to make full use of the InGaN emitter barrier to launch hot electrons. In the example presented in this chapter, BHI causes a ~ 100 meV reduction in electron injection energy at room temperature. This is roughly equivalent to the energy lost in a single longitudinal optical phonon scattering event.

Secondly, current transport through inhomogeneous barriers is more resistive than in their homogeneous counterparts (see the discussion about the ideality factor in Section 3.3.1). This causes the flat-band diode resistance to be higher, which limits the achievable forward current density. To understand this, consider the discussion of extrinsic voltage

drops from Section 3.2. Using TLM measurements and calculations based on the device geometry, we demonstrated that the voltage drops in the extrinsic base region were negligible. TLM measurements were also performed on the emitter layer and the contact and sheet resistances were found to be 5.6 $\Omega \cdot$ mm and 1622 $\Omega/\square$, respectively. Per the method outlined in Appendix B, the emitter resistance and emitter voltage drop are found to be 100 Ω and 0.4 V, respectively, at an applied bias of 1.25 V. Immediately we learn that the emitter extrinsic regions are more resistive than those in the base. More importantly, however, there is an additional 0.85 V being dropped across the intrinsic device region in spite of the fact that the barrier has ostensibly been biased away at 1.25 V. This voltage drop corresponds to an intrinsic emitter resistance of 214 Ω, more than twice the resistance of the extrinsic emitter. Therefore, we may conclude that it is, in fact, the intrinsic emitter barrier that chokes the forward diode current! The physical cause of this choke is the resistive, low-barrier regions of the inhomogeneous InGaN barrier. As long as these inhomogeneities are present, they will have a deleterious effect on the achievable forward current density.

In this chapter we have presented the first demonstration of the III-N Nitrogen-polar HET. While the measured common-emitter current gain was very low, the excellent contacts to the highly-scaled base layer enabled otherwise ideal device operation. We used the working devices to study InGaN polarization dipole diode transport and to demonstrate the physical relevance of the apparent barrier height, which plays a central role in barrier height inhomogeneity theory. We determined that the most likely physical cause of barrier height inhomogeneity in the N-polar HET emitter is small-scale In compositional fluctuations. These fluctuations were shown to decrease the average injection energy of the PDD emitter and limit the emitter current density. To this point we have considered the transport properties of electrons in the vicinity of the emitter and collector barriers in the N-polar HET. In the next chapter, we will briefly analyze the transport

properties of Ga-polar HETs.

Chapter 4

Ga-polar HETs and AlN emitter diode transport

In this chapter we will present a brief analysis of the Ga-polar HET and the AlN emitter diode with the goal of comparing the results to the N-polar HET data presented in Chapter 3. The majority of the measurement and analysis methods are identical to those used for N-polar HETs. Therefore, we will refer the interested reader to Chapter 3 for a detailed description of these methods and provide only an abbreviated version here. The chapter will be organized into two brief sections: first, we will present the Ga-polar HET design and discuss its advantages over N-polar designs. We will also present and briefly analyze Ga-polar transistor data. Second, we will analyze the AlN emitter diode using $I-V-T$ measurements and BHI theory before discussing the implications of the results for HET operation.

4.1 Device design, growth and fabrication

The Ga-polar HET design is based on the polarization dipole approach discussed in Chapter 1. The conduction band diagram for such a design in pictured in Fig. 4.1. The emitter and collector barriers are formed using thin AlN and InGaN polarization dipole barriers, respectively. There are several important differences between this design and the N-polar design presented in Chapter 3. First, there is no large dipole barrier present at the base-collector interface as there is in the N-polar HET. This should reduce quantum mechanical reflections for moderate emitter barrier heights and lead to an increase in current gain. Second, the InGaN dipole emitter in N-polar HETs is intended to be a thermionic injector while the AlN diode in Ga-polar HETs is designed as a tunnel injector. Because the AlN layer is very thin, we expect electrons to be injected at the top of the drift field region of the emitter barrier in Fig 4.1 or at about 1.3 eV (see blue arrow in the figure). In Chapter 3 we found that lateral barrier height fluctuations led to resistive voltage drops in the emitter that ultimately limited the achievable current density. Because the AlN diode is a tunnel injector, we expect that the current choke may be even more severe in the Ga-polar HET.

A processed device schematic and layer structure for the Ga-polar HET is pictured in Fig. 4.2. The device was grown using an experimental hybrid technique: the collector barrier was grown by MOCVD and the emitter barrier by plasma-assisted MBE. The purpose of such a hybrid growth process was to avoid the unintentional incorporation of Ga into MOVCD-grown AlN films[104, 77]. Because the polarization charge discontinuity is higher at AlN/GaN junctions than at AlGaN/GaN junctions, growth of pure AlN by MBE enables a large electron injection energy without introducing a thick tunnel barrier into the emitter[81].

During device processing base mesa isolation was performed using a low-power re-

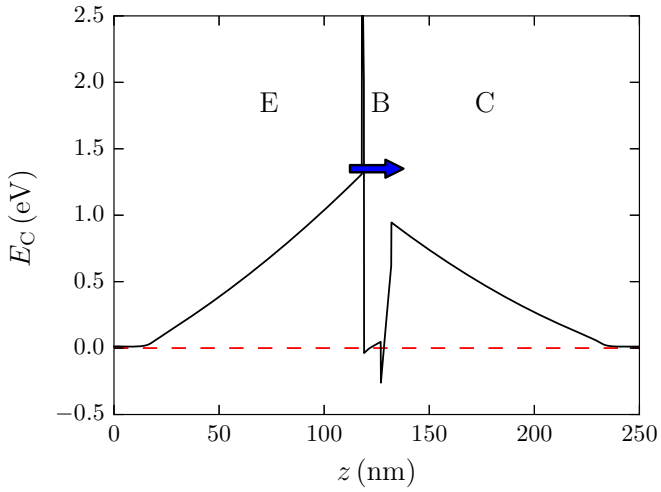

Figure 4.1: Conduction band diagram for the Ga-polar HET with an 8 nm GaN base. The regions of the band diagram that correspond to the emitter, base and collector have been labeled along with the equilibrium Fermi level (dashed red line). The thin AlN dipole layer provides a tunnel injector of hot electrons into the base (blue arrow).

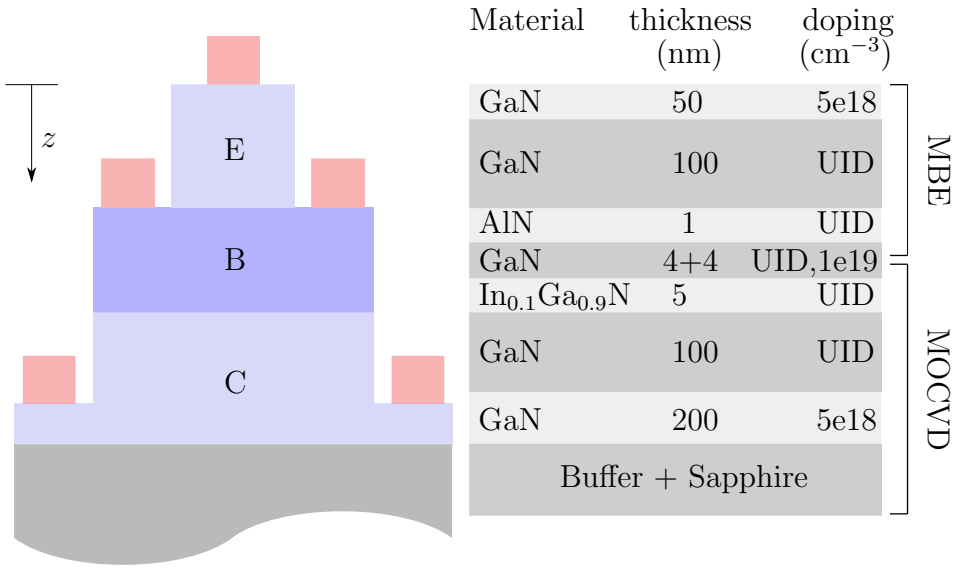

Material	thickness (nm)	doping (cm^{-3})	
GaN	50	5e18	MBE
GaN	100	UID	
AlN	1	UID	
GaN	4+4	UID,1e19	
$In_{0.1}Ga_{0.9}N$	5	UID	MOCVD
GaN	100	UID	
GaN	200	5e18	
Buffer + Sapphire			

Figure 4.2: Ga-polar HET layer structure and processed device schematic. The layers that compose the emitter, base and collector have been labeled and the metal contacts are pictured in red. The bottom half of the layer stack was grown by MOCVD and the top half by PAMBE.

active ion etch (RIE) with BCl_3/Cl_2 etch chemistry. To form an ohmic contact to the base through the wide-bandgap AlN interlayer, a selective BCl_3/SF_6 inductively coupled plasma (ICP) etch was performed. During etching the BCl_3 plasma removes GaN until the AlN layer is exposed. The subsequent reaction between the SF_6 plasma and the exposed AlN leads to the formation of a nonvolitile AlF_3 complex that prevents etching of AlN. After the selective etch was completed, the AlF_3 was removed with a 10 minute 400°C anneal in N_2[105]. An ohmic tunnel contact to the base layer was formed by depositing an Al/Au metal stack on the AlN interlayer. The emitter and collector contacts were also formed via Al/Au metal stacks deposited using e-beam evaporation.

4.2 Room temperature transistor operation

Common-emitter characteristics of the Ga-polar HET are shown in Fig. 4.3. The various regimes of transistor operation are labeled in the figure and discussed in detail in Chapter 3. The relatively smaller collector barrier in the Ga-polar HET has three effects: first, the device turn-on voltage is larger because the collector injects more current into the base for small collector biases; second, the device breakdown voltage is lower than in N-polar devices; and third, the current gain (β) is ~ 0.21, over an order of magnitude larger than in N-polar HETs. This corresponds to a transfer ratio of ~ 0.18. The large increase in gain from N-polar to Ga-polar HETs highlights the detrimental effect of the AlGaN polarization dipole in the collector of N-polar devices. The base contacts were characterized using TLM measurements and the contact and sheet resistances were found to be 1.15 $\Omega\cdot$mm and 4085 $\Omega/\square$, respectively. These values are substantially larger than those of N-polar HETs (0.34 $\Omega \cdot$ mm and 517 $\Omega/\square$). This is consistent with our statement in Chapter 3 that the low-bandgap InGaN layer in the N-polar HET enables low-resistance ohmic contacts to the base and, therefore, provides an advantage over Ga-

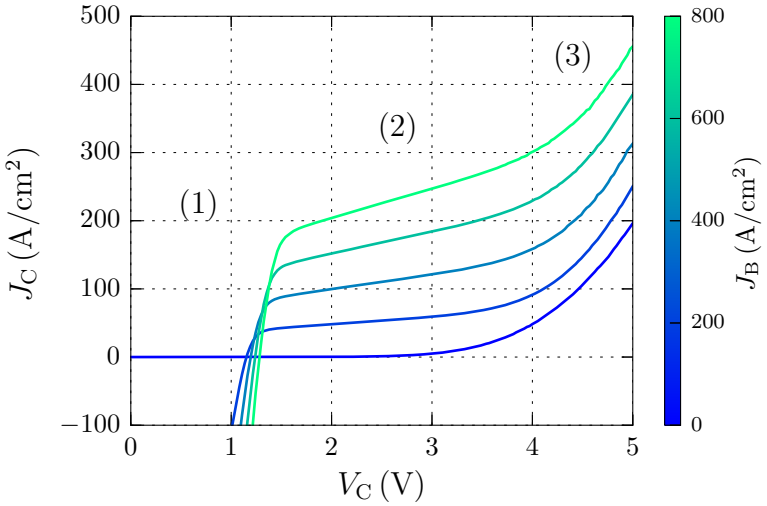

Figure 4.3: Common-emitter collector $I-V$ characteristics for the Ga-polar HET at room temperature. The three regimes of transistor operation are labeled as (1) - turn-on, (2) - saturation and (3) - breakdown. The current gain of the transistor is ~ 0.2.

polar HETs. Based on these data we may conclude that for polarization dipole HETs, Ga-polar devices have superior current gain but inferior quality base contacts.

4.3 AlN polarization dipole barrier transport

In this section we will follow an abbreviated version of the method presented in Chapter 3 for analyzing polarization barrier transport in the AlN emitter. Because a detailed analysis has already been performed in Chapter 3, here we aim only to introduce the analysis method in the context of tunnel barriers and discuss the effects of our results on transistor function. We will start by considering diode $I-V-T$ data, which is shown in Fig. 4.4. Note that this figure shows the emitter current in the modified Gummel configuration, which is equivalent to a two-terminal diode $I-V$ measurement. At low bias, the emitter current increases slowly until device turn-on ($V \simeq 1$ V). After turn-on the current increases exponentially before ohmic voltage drops begin to dominate.

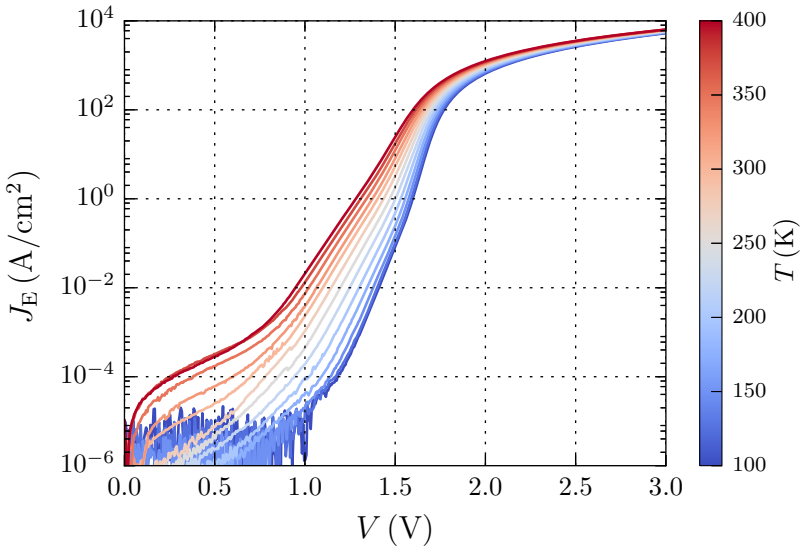

Figure 4.4: Forward bias AlN emitter diode $I-V-T$ characteristics for the temperature range $100-400$ K.

Furthermore, the low-bias current is temperature-dependent, which suggests the presence of a thermally-activated leakage mechanism for $V < 1$ V. If this leakage path were not present, the high temperature current would decrease to the noise floor at low bias as it does at low temperature.

In order to extract the saturation current (J_S) from the diode $I-V$ a data analysis algorithm was developed to identify the point where the slope of the current ($\mathrm{d}J_E/\mathrm{d}V$) is maximized. A small bias range is selected around this point and a line is fitted to the data in this range. The saturation current is then determined from the ordinate axis intercept of the fit line. The resulting Richardson plot is pictured in Fig. 4.5. The Richardson data are clearly nonlinear as they were for the InGaN diode discussed in Chapter 3. We hypothesize that this nonlinearity is cause by barrier height inhomogeneity (BHI). Following the discussions presented in Chapters 2 and 3, we assume a Gaussian

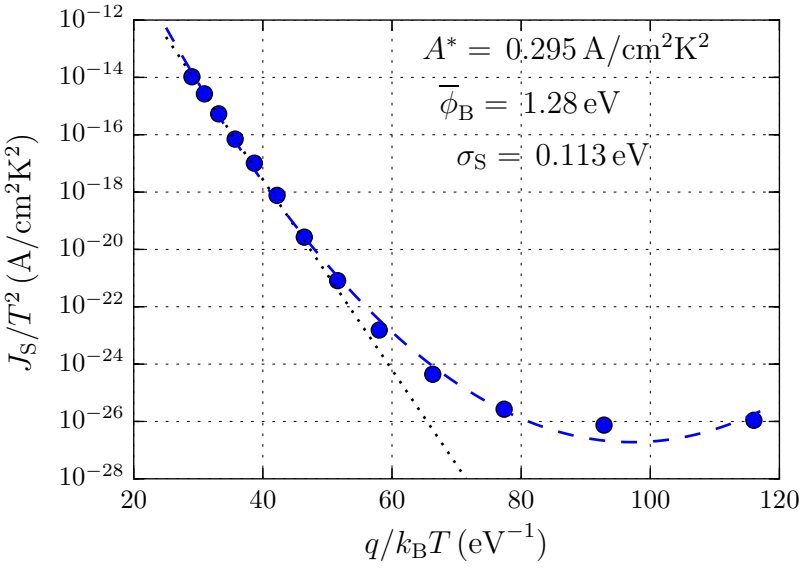

Figure 4.5: Richardson plot for the AlN emitter diode. The values of A^*, $\overline{\phi}_B$ and σ_S are extracted from the second order fit (blue dashed line). A linear fit to the high temperature data is also shown (black dotted line).

distribution of barrier heights and fit the data to the second-order equation:

$$\ln\left(\frac{J_\mathrm{S}}{T^2}\right) = \ln(\mathrm{A}^{**}) - \left(\frac{q}{k_\mathrm{B}T}\right)\overline{\phi}_B + \frac{1}{2}\left(\frac{q}{k_\mathrm{B}T}\right)^2 \sigma_\mathrm{S}^2, \tag{4.1}$$

where A^{**} is the effective Richardson constant, $\overline{\phi}_B$ is the mean barrier height and σ_S is the standard deviation of the barrier height distribution. The values of A^{**}, $\overline{\phi}_B$ and σ_S are then extracted from the zeroth, first and second order coefficients, respectively. The extracted mean barrier height is nearly identical to the designed injection energy in Fig. 4.1. The standard deviation in the barrier height amounts to a 9% variation over the device area. The effective Richardson constant, on the other hand, is two orders of magnitude smaller than the theoretical value for GaN (26 $\mathrm{A/cm^2K^2}$). We can understand this by appealing to the argument presented at the end of Chapter 2. Rather than regarding the Richardson constant as a material quantity, we should instead consider it

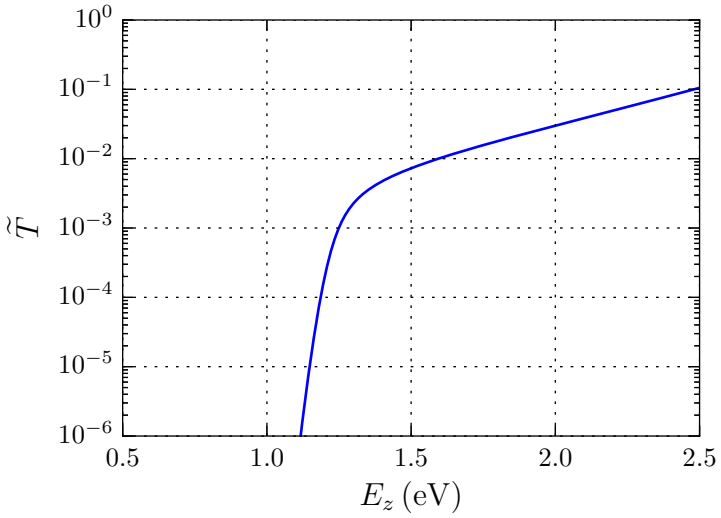

Figure 4.6: Transmission characteristics of the AlN diode. In the range of electron injection energies the transmission probability is $10^{-3} - 10^{-2}$.

to be device quantity. To this end we defined the effective Richardson constant using the approximate expression

$$A^{**} \simeq \widetilde{T}_0 A^*, \tag{4.2}$$

where $A^* = 26\,\mathrm{A/cm^2K^2}$ and $\widetilde{T}_0$ is the transmission probability of the barrier close to the mean electron injection energy. To test the applicability of this definition the transmission characteristics of the AlN polarization dipole barrier are calculated via the methods presented in Chapter 2 (Fig. 4.6). The figure demonstrates that the transmission probability for electrons around 1.3 eV is $\sim 5 \times 10^{-3}$. When plugged into Eq. (4.2) this gives $A^{**} \simeq 0.13\mathrm{A/cm^2K^2}$, much closer to the value obtained from the fit in Fig. 4.5. This result validates our reinterpretation of the Richardson constant in light of nonunity transmission at the barrier interface. Furthermore, the depressed value of A^{**} suggests that, even in the absence of BHI, the current provided by the AlN tunnel barrier will be reduced by two orders of magnitude compared with a thermionic emission barrier.

To demonstrate the limitations of traditional fitting methods, a linear fit to the high-

temperature Richardson data is performed (black dotted line in Fig. 4.5). From this linear fit and the traditional Richardson equation, we find $A^* = 5.01 \times 10^{-5}\,\mathrm{A/cm^2K^2}$ and $\phi_\mathrm{B} = 0.76\,\mathrm{eV}$. These results are consistent with previous observations that the high-temperature linear fit underestimates the value of A^* and ϕ_B (see [83] and Chapter 3 of this thesis). Therefore, the quadratic fitting method is the only acceptable approach for analyzing nonlinear Richardson data.

Finally, the apparent barrier height and the ideality factor of the AlN diode are extracted from the forward bias diode $I - V$ (Fig. 4.7). The dashed blue line in Fig. 4.7(a) represents the equation:

$$\phi'_\mathrm{B} = \overline{\phi}_\mathrm{B} - \frac{q}{2k_\mathrm{B}T}\sigma_\mathrm{S}^2, \tag{4.3}$$

where the values of $\overline{\phi}_\mathrm{B}$ and σ_S are taken from the quadratic fit in Fig. 4.5. It is important to note that when calculating ϕ'_B from J_S in Fig. 4.7(a), the correct value of A^* must be used. If the theoretical value of 26 $\mathrm{A/cm^2K^2}$ is used, Eq. (4.3) will not match well with the experimental data. This result demonstrates the fundamental nature of the Richardson plot and of J_S. By contrast, ϕ'_B is a derived quantity that requires accurate inputs from the Richardson plot. Simulated values of ϕ'_B span the range from 1.1 eV at 100 K to 1.37 eV at 400K, all larger than the values pictured in Fig. 4.7(a). This is similar to the results presented in Chapter 3. Therefore, as with the InGaN diode, the emitted electrons are not launched with the full barrier height energy. Barrier height inhomogeneity ensures that even if a 1.3 eV barrier is designed, the injection energy remains < 1 eV at room temperature. This difference is energetically equivalent to the emission of more than three optical phonons in the base ($\hbar\omega_\mathrm{OP} \simeq 92\,\mathrm{meV}$)! This is clearly detrimental for device gain and has important implications for future device designs (see Chapter 6).

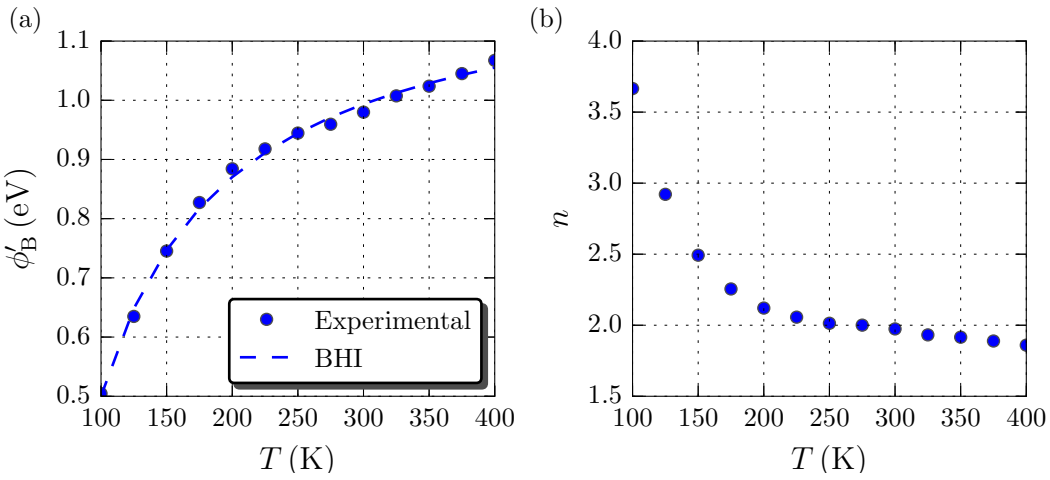

Figure 4.7: (a) Apparent barrier height and (b) ideality factor for the AlN emitter diode. The dashed blue line is generated using Eq. (4.3).

Beyond 1.6 V in Fig. 4.4, ohmic voltage drops in the intrinsic region become appreciable. This phenomenon was discussed in detail in Chapter 3. To summarize, fluctuations in barrier height give rise to current crowding effects in the vicinity of low barrier regions, which, in turn, cause resistive transport beyond a certain current density threshold. The resistance associated with the fluctuations is added to the previously mentioned tunnel resistance, albeit in a highly complicated and nonlinear fashion. Nonetheless, the fluctuations and the tunnel barrier together conspire to dramatically reduce the AlN emitter current density. This limits the potential of the Ga-polar, AlN emitter HET for high-frequency applications. Without a method for reducing these resistive voltage drops, emitter currents densities will remain prohibitively low.

At this time the physical source of the observed barrier height inhomogeneity is unknown. Because AlN is a binary, alloy fluctuations cannot be the cause of BHI in these diodes. Simulation data suggest that the high-temperature ideality factor due to thermionic field emission is ~ 1.2. Therefore, as with the InGaN diode in Chapter 3, thermionic field emission alone cannot account for the experimentally derived ideality factors, which are ~ 1.9 at high temperatures. It is more likely that thermionic field

emission plus either lateral thickness fluctuations or nonuniform threading dislocation-mediated transport is producing the temperature-dependent barrier height and the large ideality factor.

In this chapter we have presented an analysis of the Ga-polar HET and found it to have superior gain when compared with N-polar HETs. This is due to the relatively smaller InGaN collector barrier used in Ga-polar designs. The AlN emitter diode was analyzed and evidence of BHI was found. A quadratic fit to the Richardson data yielded accurate values for the mean barrier height and a standard deviation of about 10% across the device area. The values for the apparent barrier height suggested that the electrons were not emerging with the full designed injection energy but rather were injected into the base through low barrier regions. The depressed value of the effective Richardson constant was understood by simulating the tunneling probability through the thin AlN layer. The low electron tunneling rate and the observed BHI choke the forward emitter current and severely limit the ability of the AlN diode to provide large current densities.

So far we have considered the transport properties of electrons in the vicinity of the emitter and collector barriers in both N-polar and Ga-polar HETs. In the next chapter, we will round out our analysis by investigating quasi-ballistic electron transport in the base.

Chapter 5

Hot Electron Mean Free Path in GaN

In this chapter we will investigate hot electron transport in the base region of the HET. In particular, we will demonstrate how the HET can be used to measure the hot electron mean free path or, equivalently, the momentum relaxation rate in GaN. First, we will discuss the various electron scattering mechanisms in wurtzite GaN, paying particular attention to those likely to dominate for high-energy electrons at room temperature. Second, we will discuss relaxation rates and previous attempts to measure them in III-N materials. Third, we will derive a formula that quantifies the effect of momentum relaxation on the transistor transfer ratio. This will allow us to obtain information about microscale electron transport phenomena from macroscale device metrics. Fourth, we will present the device design and experimental procedure used to measure the mean free path in GaN and present measurement results and analysis. Finally, we will conclude by discussing the implications of our results for hot electron transistor operation.

5.1 Scattering mechanisms in wurtzite GaN

In this section we will review the scattering processes present in wurtzite GaN. The relative magnitudes of each scattering process depend on the material properties, the local electric field and the temperature. Our goal will be to determine which processes are most likely to dominate for hot electrons in the base region of the HET. This will enable a more complete physical understanding of the experimental results presented later in this chapter.

In general, when an electron is scattered, it undergoes a transition from initial momentum state $\boldsymbol{k}$ to a final state $\boldsymbol{k}'$. Elastic (energy-conserving) scattering events are characterized by $|\boldsymbol{k}'| = |\boldsymbol{k}|$ and inelastic events by $|\boldsymbol{k}'| \neq |\boldsymbol{k}|$. Transition rates are typically calculated by specifying the perturbing potential, calculating the interaction matrix elements connecting $\boldsymbol{k}$ and $\boldsymbol{k}'$ and using Fermi's Golden Rule. These rates are dependent upon the angle between $\boldsymbol{k}$ and $\boldsymbol{k}'$ as well as the energy difference in the case of inelastic scattering (see Ref. [106] for calculations of the generalized scattering rates for a wide variety of processes). To determine the effects of scattering on an ensemble of electrons, the wavepacket is decomposed into its constituent $\boldsymbol{k}$ states using Fourier methods, the scattering rates of each state are calculated separately and a new wavepacket is reconstructed from the scattered distribution of $\boldsymbol{k}'$. Although the electron ensemble injected into the base of a HET has a finite spread in $\boldsymbol{k}$, we will assume that we have a relatively narrow distribution such that the conclusions drawn from a single representative momentum state apply to the larger ensemble.

Broadly speaking, there are two distinct categories of scattering events: lattice scattering, which occurs even in perfect crystals, and defect scattering, which results from imperfections introduced into the lattice during growth and/or device fabrication. In this section we will briefly consider the relevant physical processes responsible for these

scattering events and estimate the scattering rate for each.

Lattice scattering in semiconductors is caused by the interaction of conduction band electrons with the vibrating atoms that make up the crystal lattice. The bandstructure of a semiconductor is calculated by assuming a static background of lattice atoms that gives rise to a perfectly periodic potential. In real semiconductors the lattice atoms oscillate about their equilibrium positions due to thermal excitation. The time-dependent displacement of these atoms causes perturbations in the lattice potential that scatter mobile electrons. Quantum mechanics stipulates that the energy and, therefore, the displacement amplitude, of these lattice vibrations is quantized in units of $\hbar$. These quanta of energy are called called phonons. Being bosons, the phonon occupation at a given frequency and temperature is given by the Bose-Einstein function. Furthermore, the relative phase of oscillation between nearest neighbor lattice sites determines the energy and momentum spectrum of the associated phonon. An in-phase oscillation of nearest neighbors is called an acoustic phonon while an out-of-phase oscillation is called an optical phonon.

Because the overall size of the crystal is equal to an integer multiple of the lattice constant, only certain combinations of wavevector and frequency will satisfy the boundary conditions at the crystal edges. These combinations are given by the dispersion relation $\omega(\boldsymbol{k})$. Every crystalline material has its own characteristic phonon spectrum determined by the masses of the constituent atoms and the bond strength. Generally speaking, the acoustic phonon spectrum is characterized by a relatively small $\boldsymbol{k}$ and a linear dispersion relation ($\omega(\boldsymbol{k}) \propto \boldsymbol{k}$). Optical phonons, by contrast, possess large $\boldsymbol{k}$ and a nearly flat dispersion relation ($\omega(\boldsymbol{k}) \neq f(\boldsymbol{k})$)[107]. In all cases phonon scattering events must conserve both energy ($E = E' + E_{\mathrm{ph}}$) and momentum ($\boldsymbol{k} = \boldsymbol{k}' + \boldsymbol{k}_{\mathrm{ph}}$). These conservation laws constrain the set of phonon states allowed to participate in a given interaction.

With these general features in mind, we will first discuss the scattering processes

attributed to acoustic phonons. Electron-acoustic phonon coupling can occur via two distinct mechanisms: deformation potential scattering and piezoelectric scattering. Deformation potential scattering occurs because the material bandgap is a strong function of the local lattice spacing. Deviations from the equilibrium lattice spacing, therefore, modulate the bandgap and lead to the the formation of local density-of-states barriers to electron flow. This is precisely the same mechanism that limits current flow in designed heterojunction barriers. We can use a linear dispersion relation and typical values for the wavevector and material sound speed (10^7 cm^{-1} and 5×10^5 cm/s, respectively) to calculate a typical acoustic phonon energy of $1 - 5$ meV. Because this energy is small compared to $k_{\mathrm{B}}T$ at room temperature ($\sim$ 25 meV), deformation potential scattering can be considered to be elastic except for $T < 100$ K. For electrons with a kinetic energy of 1 eV, the deformation potential scattering rate in GaN is $\sim 8 \times 10^{12}\,\mathrm{s}^{-1}$ at room temperature[108, 109].

The second mechanism of electron-acoustic phonon coupling is piezoelectric scattering. This scattering process arises from the modulation of the local piezoelectric field caused by the perturbed position of the lattice atoms. Unlike deformation potential scattering, this process arises from classical position-dependent electrostatic fields rather than quantum mechanical effects. The scattering rate for high-energy electrons due to piezoelectric coupling is $\sim 1 \times 10^{11}\,\mathrm{s}^{-1}$ at room temperature[109, 110]. This relatively slower rate implies that deformation potential scattering is the dominant acoustic scattering mechanism for hot electrons at room temperature.

For antiphase lattice oscillations, the dominant scattering mechanism is polar optical phonon (POP) scattering. In a highly ionic crystal like GaN, the Ga and the N atoms acquire a slight negative and positive charge, respectively. These oppositely charged atoms vibrate out of phase with one another and produce an oscillating dipole field that scatters electrons. The allowed vibrational modes are dependent upon the crystal

symmetry so that optical phonon emission may be preferentially directed along certain crystal axes. The POP energy in GaN is larger than that of other III-V materials (~ 92 meV) owing to the relatively strong Ga−N bond. In order to emit a POP, an electron must acquire a kinetic energy greater than the phonon energy. Therefore, the POP emission rate is zero for electron kinetic energies less than ~ 0.09 eV but rises quickly for higher energies[111]. The electron-POP interaction time is often estimated using a model based on the polar Frölich interaction, which predicts an emission time given by[112]:

$$\frac{1}{\tau_{\mathrm{e-ph}}} = \frac{e^2}{4\pi\hbar}\sqrt{\frac{2m^*\hbar\omega_{\mathrm{POP}}}{\hbar^2}}\left(\frac{1}{\epsilon_\infty} - \frac{1}{\epsilon_0}\right), \tag{5.1}$$

where $\hbar\omega_{\mathrm{POP}}$ is the polar optical phonon energy, m^* is the effective mass and ϵ_0 and ϵ_∞ are the DC and high-frequency dielectric constants, respectively. Plugging in the known material constants for GaN yields $\tau_{\mathrm{e-ph}} \simeq 9$ fs or a scattering rate of $\sim 1 \times 10^{14}\,\mathrm{s}^{-1}$. This is more than an order of magnitude faster than the deformation potential scattering rate, which suggests that POP emission is the dominant phonon-mediated relaxation mechanism for electrons in GaN. In the absence of hot phonon effects, the phonon absorption rate is $\sim 0.5 \times 10^{12}\ \mathrm{s}^{-1}$[111] owing to the relatively smaller occupation of POPs at room temperature. Note that, unlike thermalized bulk or 2DEG electrons, POP scattering for hot electrons with energies > 1 eV is a fairly elastic process.

In addition to intravalley POP processes, optical phonons can also mediate intervalley scattering events in which an electron experiences an abrupt change in both wavevector and effective mass. The closest satellite valley in GaN is the L valley, which researchers estimate is $1 - 2$ eV above the Γ valley minimum[113, 114, 115, 116]. An electron with kinetic energy greater than the L valley minimum may scatter from $\Gamma \rightarrow L$ with an optical phonon providing the necessary momentum difference. This kind of scattering event is potentially important for hot electrons in III-N HETs, which are routinely launched

with energy > 1 eV. If present, intervalley scattering can dramatically increase electron reflection at the collector barrier by inducing a large effective mass mismatch between electron states in the base and the collector.

Phonon scattering processes are always present even in perfect crystals. Real semiconductor crystals invariably contain defects, whether they be structural defects like threading dislocations or impurities like vacancies or ionized dopants. Many of these defects can be treated as isolated point or line charges, which scatter electrons according to a Rutherford-like formula[117]. The scattering cross section depends inversely on the square of the incident energy so that high-energy carriers "see" a smaller target area than do low-energy carriers. As such we would expect charged defect scattering to be less prominent for hot electrons than for thermalized electrons near the band edge.

It has been shown that for doping densities of $\sim 10^{18}$ cm^{-3} the defect-limited mobility is over an order of magnitude larger than the optical phonon-limited mobility for 2DEG electrons at room temperature[41] . This implies that defect scattering rates are at least an order of magnitude slower than POP scattering rates. Furthermore, these rates are calculated for thermalized electrons close to the conduction band edge. For reasonable doping levels ($10^{16} - 10^{19}$ cm^{-3}) the high-energy electron scattering rates drop by an order of magnitude compared with the low-energy rates[118, 18]. For this reason we expect defect scattering to be relatively slow and POP scattering to be the dominant overall scattering mechanism for hot electrons in GaN. It should be noted that for electron energies in excess of 1.5 eV, deformation potential scattering becomes appreciable and cannot be neglected. In the experiment presented in this chapter, however, electrons are launched with an energy of ~ 1 eV, safely below the onset of deformation potential scattering.

5.2 Energy and momentum relaxation rates in GaN: concepts and previous measurements

The electron-phonon scattering time ($\tau_{\mathrm{e-ph}}$) discussed in the previous section is the most fundamental time scale associated with scattering interactions. However, it is usually not possible to measure $\tau_{\mathrm{e-ph}}$ directly. Rather, the effects of phonon scattering are evident in the processes of momentum and energy relaxation. These relaxation events have their own characteristic time scales, which can be directly probed in real semiconductor films and devices. Here we discuss these processes conceptually and experimentally with the goal of better understanding the mean free path measurement in the HET.

The difference between energy and momentum relaxation can be most readily understood by considering the schematic in Fig. 5.1. The figure depicts an ensemble of electrons injected with initial longitudinal momentum k_z^0. For $t > 0$, the electrons undergo scattering events that perturb their individual momenta and cause the ensemble average momentum, $\langle k_z \rangle$, to decrease from k_z^0. After a time equal to the momentum relaxation time (τ_{m}), the longitudinal momenta are partially randomized such that $\langle k_z \rangle$ has decreased by $1/e$. Note that we have assumed that the scattering events are fairly elastic so that at $t = \tau_{\mathrm{m}}$ the kinetic energy (represented by the length of the arrows in Fig. 5.1) is approximately equal to its initial value: $\langle E_z \rangle \sim E_z^0 = \left(\hbar k_z^0\right)^2 / 2m^*$. In other words, we are assuming that the energy loss per collision is small compared with the initial kinetic energy. Furthermore, it is known that the electron-POP interaction favors small angle scattering events[110]. This implies that the electrons must undergo multiple scattering events in order to relax their momentum (i.e. $\tau_{\mathrm{m}} > \tau_{\mathrm{e-ph}}$). For $t > \tau_{\mathrm{m}}$ the electrons continue to scatter, losing a small amount of kinetic energy with each collision. Eventually, after a time equal to the energy relaxation time (τ_{E}), the electrons have lost most of the excess kinetic energy acquired at injection and have partially relaxed

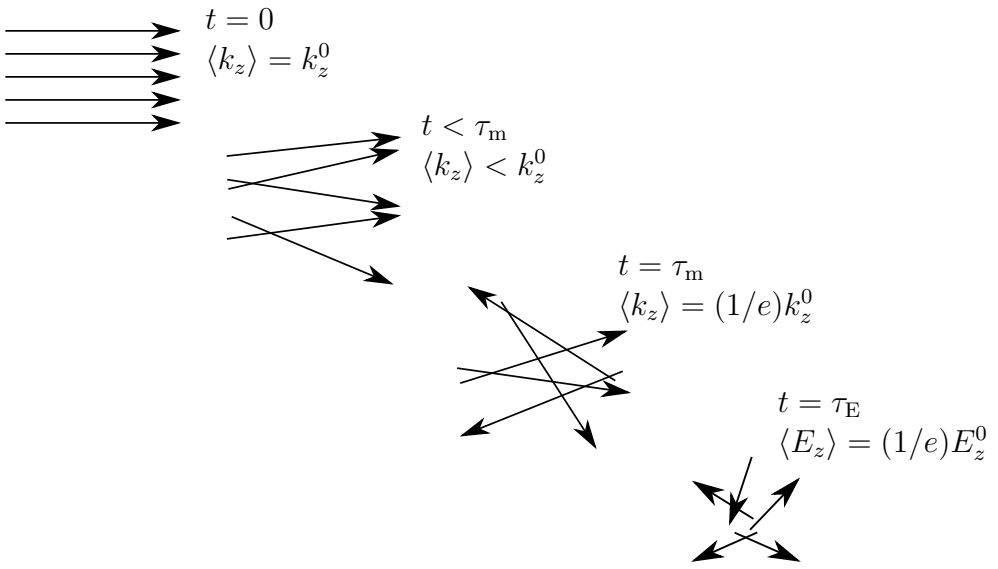

Figure 5.1: Schematic representation of momentum and energy relaxation for an injected electron ensemble with initial momentum k_z^0[106]. Momentum relaxation occurs when the direction of propagation is mostly randomized; energy relaxation occurs when most of the electron kinetic energy in excess of $k_{\mathrm{B}}T$ is lost.

to the band edge. At this point the average kinetic energy in the z-direction is equal to $(1/e)E_z^0$. Understanding these processes allows us to compare the magnitudes of the three characteristic time scales: $\tau_{\mathrm{e-ph}} < \tau_{\mathrm{m}} < \tau_{\mathrm{E}}$.

For reasonably elastic scattering events τ_{E} can be substantially larger than τ_{m}. In the III-N HET in particular hot electrons have $E_z \gg \hbar\omega_{\mathrm{POP}}$, implying that POP scattering is largely elastic. We may, therefore, expect $\tau_{\mathrm{E}} > \tau_{\mathrm{m}}$ in this case. This inequality was confirmed by ensemble Monte Carlo calculations, which found that for 1 eV electrons in GaN, the momentum relaxation rate is an order of magnitude faster than the energy relaxation rate[119].

Attempts to measure or extract these characteristic time scales experimentally have resulted in a broad range of values. One common technique used to measure relaxation rates is the optical pump-probe scheme. In this method femtosecond optical pulses are used to generate hot carriers in bulk GaN layers and probe the subsequent energy

relaxation rate. One study found this rate to be 680 fs[120]. The authors then used an energy loss rate model to determine the value of $\tau_{\mathrm{e-ph}}$ that best matched their data; they estimated a value of $\tau_{\mathrm{e-ph}} = 200$ fs. In another approach photoluminescence spectroscopy was done on a high-electron-mobility transistor (HEMT) to determine the high-field electron temperature in the channel[121]. When combined with the same energy loss rate model, these measurements yielded $\tau_{\mathrm{e-ph}} = 100$ fs. Both of these values for $\tau_{\mathrm{e-ph}}$ are an order of magnitude larger than the theoretical prediction given by Eq. (5.1). The authors explain this discrepancy with a combination of hot phonon absorption and screening effects due to the high density of excited electrons ($\sim 10^{20}\,\mathrm{cm}^{-3}$ in Ref. [121]).

Electrical measurements have also been used to probe relaxation rates in GaN. In one study, pulsed transport and heat pulse measurements were used to probe the energy relaxation dynamics in bulk GaN epilayers[122]. Again the data was fitted using power loss rate equations, from which $\tau_{\mathrm{e-ph}} = 5 - 10$ fs was extracted. In another study, measurements of the optical-phonon-limited hall mobility in an AlGaN/GaN HEMT yielded an estimated momentum relaxation time of $\tau_{\mathrm{m}} \sim 4$ fs[123]. This implies a value of $\tau_{\mathrm{e-ph}} < 4$ fs, less than half the value of the theoretical prediction.

There are a variety of possible explanations for the large range of $\tau_{\mathrm{e-ph}}$ values and their deviation from the theoretical prediction. First, it is known that $\tau_{\mathrm{e-ph}}$ is directly proportional to the density of states, which increases with energy[124]. This dependence is not accounted for in Eq. (5.1), which implicitly assumes that the carriers reside relatively close to the conduction band edge. Therefore, any value of $\tau_{\mathrm{e-ph}}$ extracted from relaxation rates will depend on the specific excitation conditions. Furthermore, the loss rate models used in these studies may rely on assumptions (e.g. strong electron-electron interactions) that do not apply to the given experimental conditions. For these reasons it is very difficult to extract a reliable value of $\tau_{\mathrm{e-ph}}$ from experimentally measured relaxation rates. There are simply too many measurement-specific factors that must be

accounted for. However, the measured relaxation times do provide a reliable estimate of an upper bound on τ_{e-ph}. This statement may not impress researchers as much as quoting a value for τ_{e-ph}, but such a statement is undoubtedly more trustworthy.

The experimental results discussed above probe only intravalley scattering events. One study has examined intervalley $\Gamma \rightarrow L$ scattering times using wavelength-tunable pump-probe spectroscopy[125]. Their results suggest that the L valley lies approximately 1.1 eV above the Γ valley minimum and that transitions from $\Gamma \rightarrow L$ occur in 1.02 ps. Interestingly, the transition from $L \rightarrow \Gamma$ takes 20 times longer, implying that L valley states scatter very slowly compared to Γ valley states. To determine the effect of $\Gamma \rightarrow L$ scattering on quasi-ballistic electrons in the HET, we can compare the hot electron transit time in the base to $\tau_{\Gamma \rightarrow L}$. A previous report[126] calculated that for electron transport along the crystal c-axis in GaN, the group velocity at energies around 1 eV is 8.5×10^7cm/s. For a total base width of 15 nm, the transit time is, therefore, about 18 fs, much shorter than $\tau_{\Gamma \rightarrow L}$. From these results we may conclude that while hot electrons in the base may have enough energy to scatter from $\Gamma \rightarrow L$, this process is too slow to appreciably affect hot electron transport in the HET.

5.3 Theory: the effect of hot electron scattering on the transfer ratio

In order to extract the hot electron mean free path from transistor measurements, we must form a quantitative connection between microscopic scattering events in the semiconductor and measurable, macroscopic device metrics like the transfer ratio (α). The conceptual picture of hot electron transport in the base is roughly equivalent to the process shown in Fig. 5.1. Electrons are injected from the emitter into the base with

a narrow distribution of momenta centered around k_z^0. As they travel across the base, these electrons experience an increasing number of scattering events and the ensemble average, $\langle k_z \rangle$, decreases toward zero. A depressed value of $\langle k_z \rangle$ results in increased reflection at the base-collector barrier and a measurable decrease in α. By this logic we expect that the transfer ratio of the device will decrease with increasing base width. In order for this simple trend to be scientifically useful, we must determine the quantitative relationship between scattering events in the base and α. It is important to note that because the transmission characteristics of the collector barrier depend only on k_z the HET is sensitive to momentum rather than to energy relaxation. In other words, the collector barrier provides a filter for k_z (or E_z) but not for E.

We start with several assumptions: first, we will assume that after electrons are injected into the base, they experience highly directional, quasi-ballistic transport. Carriers receive kinetic energy from the electric field in the case of a polarization dipole emitter and from the crystal lattice in a heterojunction emitter. This picture contrasts with that of diffusive transport where carrier motion is thermally generated and, on a microscopic level, random. Secondly, we assume that each electron in the base scatters independently. This is tantamount to an assumption of low-level injection such that electron-electron interactions are negligible. Finally, we will restrict our analysis to situations involving a few scattering events at most. While unrealistic for bulk semiconductors, this assumption is reasonable for the highly scaled base layers that appear in the HET.

These assumptions allow us to write the following simple differential equation for electron scattering in the base:

$$\frac{\mathrm{d}n_E}{\mathrm{d}t} = Cn_E, \tag{5.2}$$

where n_E is the number of electrons with energy E that have *not* scattered and C is a constant related to the scattering rate. This equation implies a constant, independent

scattering rate for each electron irrespective of its initial kinetic energy. This approximation is reasonably accurate for the narrow electron distributions that are injected into the base because the scattering rate is very weakly dependent on energy over that range. The solution to Eq. (5.2) is a decaying exponential of the form

$$n_E = n_E^0 \exp(-t/\tau), \tag{5.3}$$

where n_E^0 is the injected electron density at energy E and τ is the (energy-independent) time between scattering events. The following intuitive boundary conditions are satisfied: at $t = 0$ the number of unscattered electrons is n_E^0, or the total number of electrons at energy E (i.e. no carriers have scattered). As $t \to \infty$ the number of nonscattered electrons vanishes as expected.

The mean free path is given by the product of the injected electron group velocity and the scattering time:

$$\lambda_{\mathrm{MFP}} = v_E^0 \tau. \tag{5.4}$$

If we define $z \equiv v_E^0 t$ along the device transport axis we may write Eq. (5.3):

$$n_E = n_E^0 \exp(-z/\lambda_{\mathrm{MFP}}). \tag{5.5}$$

Equation (5.5) is valid for any low-density, narrow distribution of hot electrons traveling ballistically. To obtain an expression containing macroscopic variables, we must make one additional assumption: the electrons that have scattered, even once, have a randomized distribution of momenta. This is equivalent to stipulating that it only takes one scattering event to relax the momentum. While not physically accurate, this assumption will drastically simplify the algebra without compromising the final result. Furthermore, compared with the unscattered electrons, the relaxed electrons will contribute a negligible

amount to collector current. This is because the ensemble average of k_z is much smaller for the scattered electrons so that they are much more likely to be reflected at the collector barrier. We may then write the following expressions connecting the unscattered electron distribution to the transfer ratio (α):

$$\begin{aligned} \alpha &= \frac{1}{N}\int n_E \widetilde{T}(E)\mathrm{d}E, \\ \alpha_0 &= \frac{1}{N}\int n_E^0 \widetilde{T}(E)\mathrm{d}E, \end{aligned} \tag{5.6}$$

where $N = \int n_E^0 \mathrm{d}E$ is the total number of injected electrons. The first expression in Eq. (5.6) states that the ratio of transmitted to incident electrons is the product of the unscattered electron distribution and the transmission probability at the collector. There is no contribution from scattered electrons because we have assumed that their transmission probability vanishes. The second expression specifies the transfer ratio in the absence of scattering (α_0) or for zero transit length.

Multiplying both sides of Eq. (5.5) by $(1/N)\widetilde{T}(E)\mathrm{d}E$, integrating and substituting expressions (5.6) produces the main result of this section:

$$\boxed{\alpha = \alpha_0 \exp(-z/\lambda_{\mathrm{MFP}})}. \tag{5.7}$$

Insofar as Eq. (5.7) captures the relevant hot electron physics, a plot of α vs. base width on a semilog scale will be linear with slope $-1/\lambda_{\mathrm{MFP}}$ and ordinate axis intercept of $\ln(\alpha_0)$. It is important to remember our earlier assumption that the mean free path does not depend on kinetic energy for narrow distributions of injected electrons. This allows us to remove λ_{MFP} from the integrals (5.6) and obtain the simple expression above.

5.4 Device design and experimental results

To make use of Eq. (5.7) to extract the mean free path, three HET samples were grown with different base thicknesses but otherwise identical design. The layer structure of the three HETs and the processed device topology is shown in Fig. 5.2; the conduction band diagram for the 10 nm GaN base HET is shown in Fig. 5.3. The emitter-base (ϕ_{EB}) and base-collector (ϕ_{BC}) barriers were formed by thin InGaN and AlGaN polarization-dipole layers[127], respectively, and the thicknesses of the GaN layer in the base (t_{GaN}) were designed to be 3, 7 and 10 nm.

Strictly speaking, the base is composed of all layers in between the emitter and collector barrier maxima. Electrons that are injected over the emitter barrier must travel across the 5 nm InGaN dipole layer as well as the GaN base layer before arriving at the collector barrier. As such, the true base width is given by $t_{\mathrm{B}} = t_{\mathrm{InGaN}} + t_{\mathrm{GaN}}$. While the presence of the InGaN layer clearly affects the magnitude of the transistor gain, this layer is common to all three devices and, therefore, does not play a role in the extraction of the mean free path.

The three HETs were grown by MOCVD on the nitrogen-polar $(000\bar{1})$ plane on 4° miscut sapphire substrates. The contact layers were doped to $5 \times 10^{18}\,\mathrm{cm}^{-3}$ to allow for low-resistance ohmic contacts while the remaining layers were unintentionally doped ($\sim 2\times10^{17}\,\mathrm{cm}^{-3}$). During device processing emitter and base mesa isolation was achieved with conventional optical lithography and low-power reactive ion dry etches (RIE) with BCl_3/Cl_2 chemistry. Typical emitter mesa dimensions were $5\mu\mathrm{m} \times 50\mu\mathrm{m}$. Non-alloyed Al/Au ohmic contacts were deposited on the emitter, base and collector layers using e-beam evaporation. Low sheet resistance in the highly scaled base was enabled by the polarization-induced 2-dimensional electron gas (2DEG) at the AlGaN/GaN interface. Furthermore, as discussed in Chapter 3, the N-polar growth orientation enabled the direct

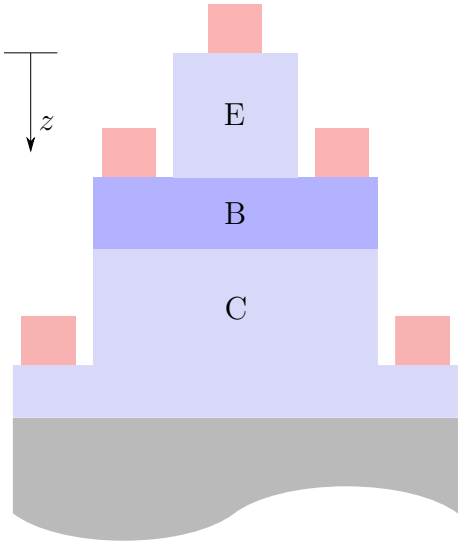

Material	thickness (nm)	doping (cm^{-3})
GaN	50	5e18
GaN	100	UID
$In_{0.12}Ga_{0.88}N$	5	UID
GaN	3, 7, 10	UID
$Al_{0.5}Ga_{0.5}N$	2	UID
$Al_{0.15}Ga_{0.85}N$	35	UID
grade	20	4e18
GaN	200	5e18
Buffer + Sapphire		

Figure 5.2: Processed layer structure for the mean free path N-polar HET series. The layers that make up the emitter, base, and collector have been labeled along with the z-axis orientation as it appears in Fig. 5.3.

deposition of ohmic base metals on the low-bandgap InGaN layer to achieve low contact resistance[75].

It is known that biasing a HET with large base resistance and large base-collector leakage in the common-base configuration can lead to erroneously high values of α because the base-collector diode leakage current is mistaken for hot electron current (see Chapter 3 of this thesis or Ref. [81] for a detailed discussion). This results in the overestimation of the mean free path as seen in a previous report[128]. To ensure an accurate measurement of α, the devices were biased in the common-emitter configuration: a constant base current density (J_B) was injected and the collector voltage (V_C) swept from zero to reverse bias while measuring the collector current density (J_C). Furthermore, the collector barrier was made large ($\phi_{BC} \sim \phi_{EB}$) in order to reduce base-collector diode leakage. This design is optimal for achieving reliable values for α and for measuring λ_{MFP} but is, of course, not suitable for achieving superior transistor performance.

The common-emitter $I - V$ characteristics of the three HET samples are shown in

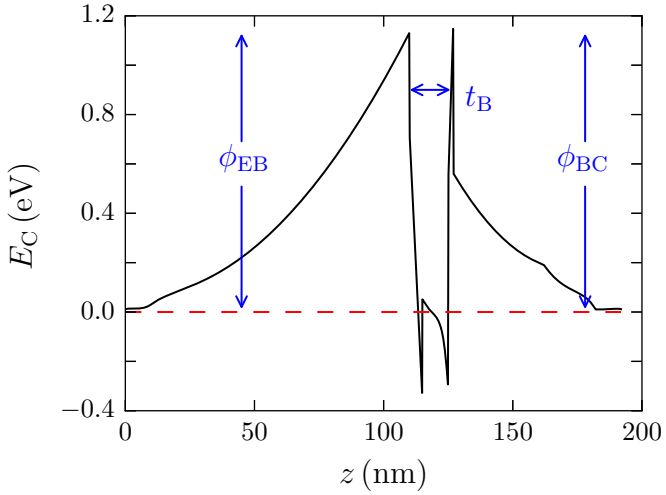

Figure 5.3: Conduction band diagram for the HET with $t_{GaN} = 10$ nm. The emitter-base and base-collector barrier heights are labeled ϕ_{EB} and ϕ_{BC}, respectively and the total base thickness is labeled t_B. The dashed red line indicates the Fermi level of the device at zero bias.

Fig. 5.4. All three devices show clear current modulation and a saturation region spanning about 3 V. The breakdown voltage is about 4 V for $t_{GaN} = 10$ nm and increases for $t_{GaN} = 3$, 7 nm as the hot electron current becomes relatively larger than the base-collector leakage current (for a detailed discussion of the common-emitter operation regions see Chapter 3 of this thesis). It is immediately clear that the collector current and, therefore, the transistor gain increases with decreasing t_{GaN} as expected from Eq. (5.7). Furthermore, the output conductance becomes more severe as t_{GaN} decreases. This is because the electrons arriving at the collector barrier have higher energy for $t_{GaN} = 3$ nm than they do for $t_{GaN} = 10$ nm and are thus more sensitive to changes in collector transmission with bias. This is the case only because the electron arrival energies are smaller than ϕ_{BC}. If the arrival energies could be made larger than ϕ_{BC}, increasing gain would, in fact, reduce output conductance. Therefore, a more general statement is appropriate: the closer the electron arrival energies are to ϕ_{BC}, the higher the output conductance.

The contact and sheet resistances for the three HETs were extracted via the transfer

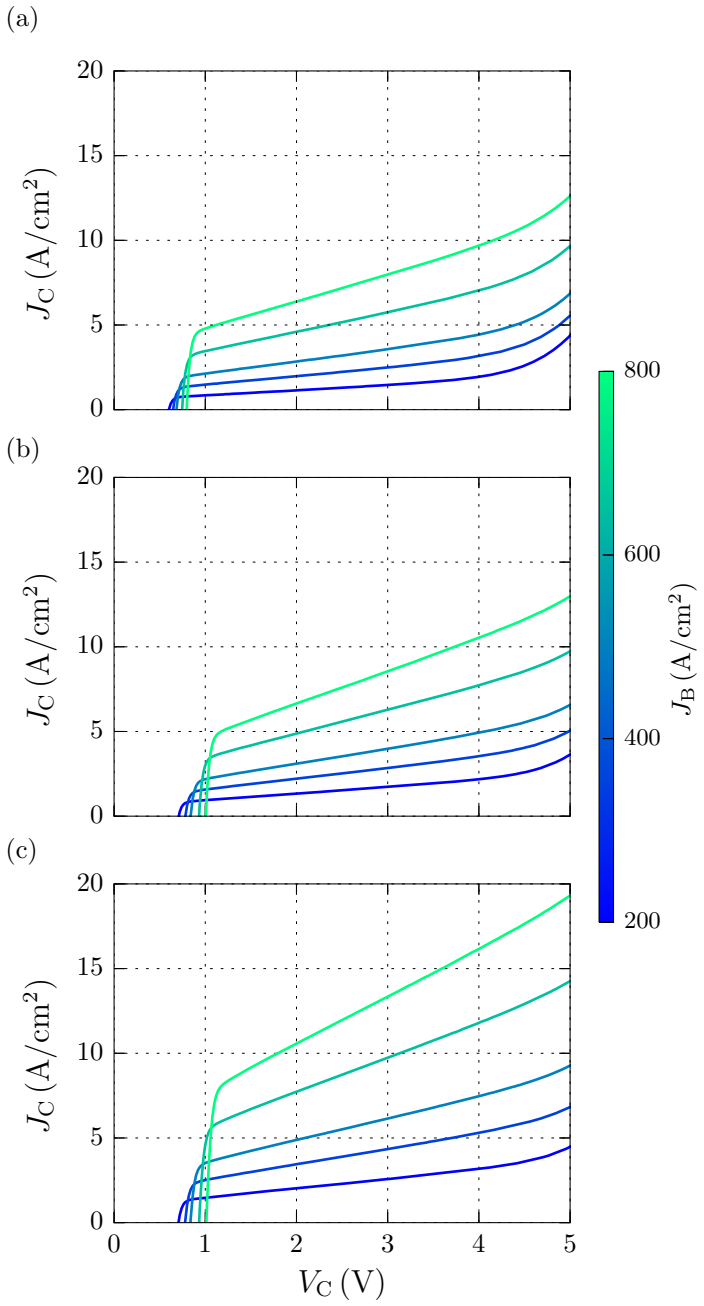

Figure 5.4: Common-emitter $I - V$ characteristics for (a) the 10 nm, (b) the 7 nm and (c) the 3 nm GaN base devices.

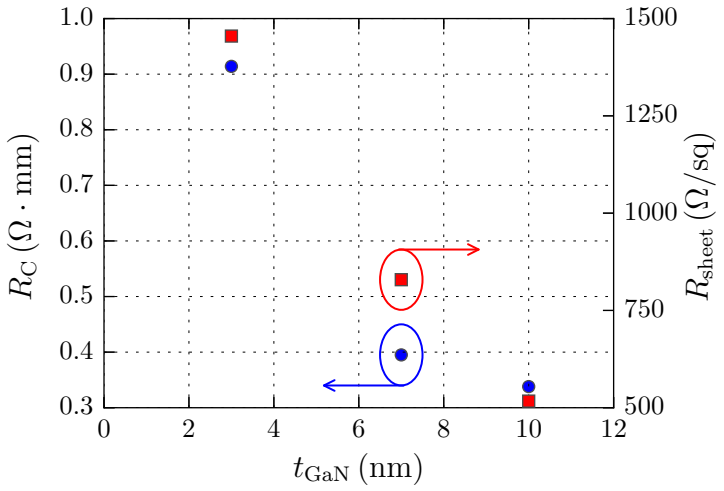

Figure 5.5: Base contact resistance (blue dots) and sheet resistance (red squares) extracted from TLM measurements for different GaN base width (t_{GaN}).

length method (TLM) on the base layer and the results are shown in Fig. 5.5. Base contacts are ohmic for all three values of t_{GaN}. The contact resistance increases from 0.34 to 0.91 $\Omega\cdot$mm and the sheet resistance from 517 to 1455 $\Omega/\square$ as t_{GaN} decreases. This is because the 2DEG at the AlGaN/GaN interface moves closer to the InGaN layer on the collector side of the base with decreasing t_{GaN}, where it experiences more frequent alloy scattering events. This results in a reduced 2DEG mobility and a resulting increase in base resistance.

To extract the transfer ratio (α), three devices were measured for each t_{GaN}. For each device and each J_{B}, α was calculated from the common-emitter $I-V$ at the knee voltage. These values were then averaged to produce one value for each combination of t_{GaN} and J_{B} (Fig. 5.6(a)). The values of α increase with increasing J_{B} as explained in Chapter 3. The transfer ratios for $J_{\mathrm{B}} = 200\,\mathrm{A/cm^2}$ along with the exponential fit function are pictured in Fig. 5.6(b). From the fit we extract a value of $\lambda_{\mathrm{MFP}} = 10.3\,\mathrm{nm}$ and $\alpha_0 = 0.009$.

We can use the extracted mean free path to calculate the momentum relaxation

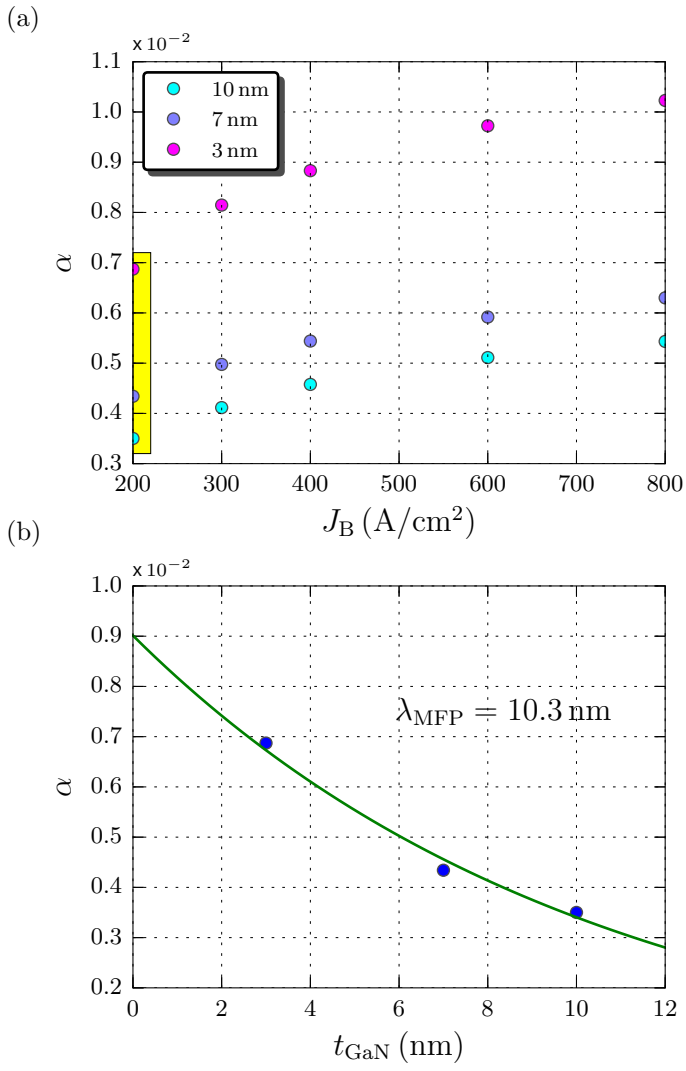

Figure 5.6: (a) Common-emitter current transfer ratio (α) for various base current densities. (b) Exponential fit to the transfer ratio as a function of GaN thickness at $J_B = 200\,\mathrm{A/cm^2}$. The data in (b) are taken from the yellow box in (a).

time via: $\tau_{\mathrm{m}} = \lambda_{\mathrm{MFP}}/v_{\mathrm{g}}$, where $v_{\mathrm{g}} = (1/\hbar)(\mathrm{d}E/\mathrm{d}k)$ is the group velocity of the injected electrons. We will use the value $v_{\mathrm{g}} = 8.5\times10^{7}$cm/s for 1 eV electrons given in Ref.[126] to calculate: $\tau_{\mathrm{m}} = 12.1$ fs. This relaxation time is very similar to the low-energy theoretical scattering time: $\tau_{\mathrm{e-ph}} = 9$ fs. The similarity between τ_{m} and the theoretical prediction for $\tau_{\mathrm{e-ph}}$ suggests that indeed optical phonon emission is the primary source of momentum relaxation for hot electrons in GaN. Additionally, we can speculate that for our specific injection conditions, $\tau_{\mathrm{e-ph}} < 10$ fs. This is very reasonable in light of our earlier discussion where we determined that $\tau_{\mathrm{e-ph}}$ decreases from 9 fs with increasing energy.

If we consider that the InGaN layer provides an additional 5 nm of scattering length, then the true base thicknesses used in this experiment were $t_{\mathrm{B}} = 8$, 12 and 15 nm. A mean free path of 10 nm implies that only the HET with $t_{\mathrm{GaN}} = 3$ nm was truly ballistic while electrons in the 7 and 10 nm GaN base samples experienced majority momentum relaxation. This result confirms the observation made in Chapter 3, where we analyzed the launch and arrival energies in the 3 nm GaN base HET and determined that the electrons were indeed traveling ballistically.

The value α_0 is the transfer ratio that would result from removing the GaN in the base entirely ($t_{\mathrm{GaN}} = 0$). The low value of $\alpha_0 = 0.009$ suggests that removing the GaN would not improve the device gain appreciably, owing to the large ϕ_{BC}, which would continue to reflect the vast majority of electrons. Furthermore, the collector simulations presented in Chapter 3 suggest that an α_0 of 0.009 corresponds to a mean electron arrival energy of about 0.8 eV. This is similar to the emitter injection energy and, therefore, suggests that there is little electron relaxation occurring in the 5 nm InGaN dipole layer.

In this chapter we have investigated quasi-ballistic hot electron transport in the base layer of the III-N hot electron transistor. By using the HET as a filter of electron momentum states, we have measured a hot electron mean free path of 10.3 nm and a corresponding momentum relaxation time of 12.1 fs. These results confirm our earlier

hypothesis that polar optical phonon emission is the dominant relaxation mechanism for hot electrons in GaN. Reducing the GaN thickness in the base was found to increase transistor current gain (β) but not enough to overcome the effects of the large base-collector barrier, which ensures that β remains much less than 1.

This concludes the data analysis section of this thesis. In the final chapter, we will summarize our results and suggest future experiments.

Chapter 6

Conclusions and Future Work

In this thesis we have explored various transport phenomena that affect III-N hot electron transistor performance. These phenomena fall within one of two categories: barrier-limited transport of majority carrier electrons in the vicinity of a heterointerface and hot electron transport of minority carriers in the base layer. Because our primary method for analyzing device performance is current-voltage-temperature measurements, it is necessary to determine the effects of microscale transport phenomena on measurable device metrics. To this end we have developed several theories to assist in the device analysis.

In Chapter 2 we developed a comprehensive theory of coherent electron transport in the vicinity of a barrier. We reviewed various methods for calculating the transmission probability before selecting the quantum transmitting boundary method for our devices. The ability to determine the precise transmission characteristics of an arbitrary barrier allowed us to model the effect of a wavepacket of hot electrons incident on the collector barrier of a HET and thus determine the arrival energy of these electrons from simple transistor measurements. Furthermore, the transmission probability was combined with the Tsu-Esaki formula to generate theoretical current-voltage-temperature curves for relevant barriers. These simulations were compared with experimental data to help

determine the effects of tunneling and voltage partitioning on observed device behavior. We also redefined the concept of the Richardson constant to account for nonunity tunneling probability at a barrier interface. The simulations developed in Chapter 2 are generally applicable to a wide variety of barriers and devices, including, but not limited to, HETs.

At the end of Chapter 2, we presented the theory of lateral barrier height inhomogeneity and explored the effects of barrier fluctuations on electron transport. We found that the primary indicator of barrier height inhomogeneity is a nonlinear Richardson plot. Moreover, we are the first to propose replacing the linear fit to the Richardson data with a second order fit, which simultaneously yields values for the effective Richardson constant, the mean barrier height and the standard deviation. We used this theory to provide an accurate description of the temperature-dependent transport properties of a GaN Schottky diode.

In Chapter 3 we investigated the properties of the N-polar HET and found that N-polar designs offer extremely low base resistance but at the cost of dramatically reduced current gain. The cause of both the low base resistance and the low gain was found to be the large AlGaN collector dipole barrier. We went on to analyze the InGaN emitter diode and found strong evidence of barrier height inhomogeneity, which was most likely caused by microscale fluctuations in indium composition in the barrier layer. These fluctuations give rise to resistive voltage drops in the intrinsic barrier region, which ultimately limited the forward current density. The InGaN diode results were corroborated via electron injection spectroscopy with the N-polar HET. These measurements along with a simulation of the transfer characteristics of the collector barrier demonstrated that the hot electron injection and arrival energies were nearly identical. This observation confirmed the barrier height inhomogeneity hypothesis and implied that electrons were traversing the base without appreciable scattering loss. We concluded that, although the current

gain is much less than unity, we have indeed achieved ballistic transistor operation in the N-polar HET.

In Chapter 4 we investigated the Ga-polar HET and found that the base resistance was higher than the N-polar device but that the current gain was substantially larger. Both of these observations were attributed to the smaller InGaN collector barrier. Analysis of the AlN emitter diode also revealed the presence of barrier height inhomogeneity, and subsequent fits produced barrier metrics that were in line with design expectations. The effective Richardson constant was found to be 100 times smaller than the theoretical value due to the tunnel barrier present in the AlN diode. This result suggested that the large current densities needed for high-frequency device operation cannot be achieved with this kind of tunnel injector. The physical cause of barrier height inhomogeneity in AlN tunnel diodes remains unknown and further investigation is needed.

Finally, in Chapter 5 we discussed hot electron transport in the base. We reviewed the possible relaxation mechanisms for hot electrons in GaN and found that polar optical phonon scattering was likely the dominant mechanism. By growing several N-polar HETs and measuring the dependence of the transfer ratio on the base width we were able to extract a hot electron mean free path of 10.3 nm. This value corresponded to a hot electron relaxation time of 12.1 fs, similar to the theoretically derived electron-phonon emission time of 9 fs. For future ballistic devices with moderate injection energies, the base must have a total thickness equal to or less than 10 nm.

6.1 Future Work

Future experimental work on III-N HETs could be driven by technological goals, scientific goals or, preferably, both. In the technological space, III-N HETs are still a long way from competing with state-of-the-art bipolar devices. The most immediate

hurdle to achieving technologically relevant performance is the low gain that is present in both Ga-polar and N-polar HETs. In both cases, the gain is limited by the relatively small difference between emitter and collector barrier heights. For N-polar devices the emitter and collector barrier heights are, at best, comparable. Currently, it is not possible to build a III-N heterojunction barrier that holds even a few volts without appreciable leakage currents. Therefore, one path forward (not discussed in this thesis) involves reducing the leakage currents through nitride heterostructures. Assuming the leakage is caused by conductive threading dislocations, this can be done either by growing HETs exclusively on bulk GaN substrates or by inserting thin p-doped layers to create a planar doped barrier. Reducing leakage would allow us to reduce the collector barrier height thus increasing gain without losing control of the device.

Assuming that either the leakage currents cannot be eliminated or that bulk GaN substrates are prohibitively expensive as a long-term solution, the other method for improving gain is to better understand and improve the emitter diode characteristics in both Ga-polar and N-polar devices. As we have seen, barrier height inhomogeneity causes the mean electron injection energy to decrease as electrons preferentially travel through low barrier regions of the emitter. This is particularly troubling because it is possible that, depending on the physical source of the inhomogeneity, the magnitude of the fluctuations increases with mean barrier height. That is, if barrier fluctuations tend to exist as a roughly fixed percentage of the total barrier height, increasing the AlN thickness or the indium composition will not cause a corresponding increase in injection energy and gain. In addition, we have seen that barrier height inhomogeneity chokes the emitter current density, which is an additional hurdle to overcome in the future. Therefore, the physical sources of inhomogeneity must be unambiguously identified if we hope to eliminate these deleterious effects.

This brings us to the scientific aspect of future HET research. Ultimately, sustained

progress will be enabled by a thorough understanding of device function and the relevant transport physics. As such, barrier height inhomogeneity and its role in HET function must be more thoroughly understood. In this thesis we have provided a few experimental and analytical methods that can be used to characterize these effects. However, there is much that remains unknown. At this point, our hypothesis that BHI in N-polar HETs is caused by indium compositional fluctuations is just that, a hypothesis. Perhaps half a dozen more devices must be grown before the physical cause can be clearly identified. For example, one could imagine growing an indium composition series so that the effects of alloy composition on dipole barrier transport can be determined. Also, growth on bulk or freestanding GaN substrates will help identify the role, if any, of dislocations on nonideal transport characteristics.

The most interesting studies would investigate the effects of changing growth conditions on device properties. For example, if the indium composition could be fixed while changing the temperature or ammonia flow (for MOCVD) or gallium flux (for MBE), diode measurements could provide a probe into the surface kinetics of the adatoms. Perhaps changing one of these conditions causes the indium and the gallium to segregate, which would increase the magnitude of the barrier height fluctuations. We could imagine asking the following research questions: for the Ga-polar emitter diode, does the growth temperature of the AlN affect the observed transport characteristics? Perhaps temperature affects the uniformity of the AlN layer and, therefore, the magnitude of the fluctuations. Also, what length scales are relevant? Do these effects disappear as the device is shrunk to submicron size or do the fluctuations occur on a scale that is too small to approach with the technology at our disposal? These questions are surely relevant for building a high-performance HET. But they are also relevant in their own right as studies that would more likely be found in a materials science department.

Despite the success of the electrical measurement technique and the proposed analysis

methods, materials characterization techniques would be extremely illuminating. For example, transmission electron microscopy (TEM) could be used to determine whether there are AlN thickness fluctuations on length scales comparable to our device size. Such a technique might also be used to probe for thickness fluctuations in the InGaN layer.

Future experiments that rely primarily on device measurements to answer these kinds of questions will have to be accompanied by suitably rigorous transport models. As we have seen, device behavior that deviates from idealized concepts is nothing except confusing without a framework within which our observations may be understood. To this end, efforts must be made to improve and refine the models proposed in this thesis. Such models are bound to encounter the natural limits of their applicability at which point they become insufficient. It has been said that the physical world tends to hide her true nature and there may be no place where this is more true than in the hot electron transistor. Still, I believe that with enough curiosity and bravery future researchers will find within the HET many fascinating phenomena to discover and loads of rich physics to comprehend.

Appendix A

Evaluation of the Gaussian integral

We want to evaluate the integral:

$$\frac{A^* T^2}{\sigma_{\mathrm{S}}\sqrt{2\pi}} \int_{-\infty}^{\infty} \exp\left(-\frac{(\overline{\phi}_{\mathrm{B}} - \phi_{\mathrm{B}})^2}{2\sigma_{\mathrm{S}}^2}\right) \exp\left(\frac{-q\phi_{\mathrm{B}}}{k_{\mathrm{B}}T}\right) \mathrm{d}\phi_{\mathrm{B}}. \tag{A.1}$$

We make the following substitutions:

$$\begin{aligned} u_{\mathrm{S}} &\equiv \frac{q(\phi_{\mathrm{B}} - \overline{\phi}_{\mathrm{B}})}{k_{\mathrm{B}}T}, \\ \sigma_{\mathrm{T}} &\equiv \frac{q\sigma_{\mathrm{S}}}{k_{\mathrm{B}}T}, \\ \mathrm{d}u_S &= \frac{q}{k_{\mathrm{B}}T}\mathrm{d}\phi_{\mathrm{B}}, \end{aligned} \tag{A.2}$$

so that the integral is transformed into

$$\frac{A^* T^2}{\sigma_{\mathrm{T}}\sqrt{2\pi}} \exp\left(\frac{-q\overline{\phi}_{\mathrm{B}}}{k_{\mathrm{B}}T}\right) \int_{-\infty}^{\infty} \exp\left(-u_{\mathrm{S}}\right) \exp\left(\frac{-u_{\mathrm{S}}^2}{2\sigma_{\mathrm{T}}^2}\right) \mathrm{d}u_{\mathrm{S}}. \tag{A.3}$$

This is a standard Gaussian integral of the form:

$$\int_{-\infty}^{\infty} \exp\left(-ax^2\right) \exp\left(-2bx\right) \mathrm{d}x = \sqrt{\frac{\pi}{a}} \exp\left(\frac{b^2}{a}\right), \tag{A.4}$$

so that Eq. (A.3) evaluates to

$$\frac{A^* T^2}{\sigma_\mathrm{T}\sqrt{2\pi}} \exp\left(\frac{-q\overline{\phi}_\mathrm{B}}{k_\mathrm{B}T}\right) \sqrt{2\pi}\sigma_\mathrm{T} \exp\left(\frac{\sigma_\mathrm{T}^2}{2}\right), \tag{A.5}$$

which simplifies to Eq. (2.66).

Appendix B

Calculation of extrinsic voltage drops

The device structure that we will analyze is pictured in Fig. B.1. Because these structures usually appear in the context of a vertical transistor, the top layer will be called the emitter (E) and the bottom layer the base (B). The relevant resistances, thicknesses and length scales have been labeled accordingly. Our goal is to determine the proportion of an applied bias that appears across the extrinsic regions. To do this, we first calculate the values of each resistor appearing in Fig. B.1(a) before multiplying by the current to get the voltage drop.

From TLM measurements the contact resistance (r_{C}) is extracted from the intercept of the fit line on a plot of resistance times pad width vs. TLM spacing. Common units for r_{C} are $\Omega \cdot \mathrm{mm}$. The resistance between the emitter contact and the emitter bulk is:

$$R_{\mathrm{E,C}} = \frac{r_{\mathrm{E,C}} L_{\mathrm{T}}}{A_{\mathrm{E,C}}}, \tag{B.1}$$

where $A_{\mathrm{E,C}}$ is the area of the emitter contact and L_{T} is the transfer length, equal to the

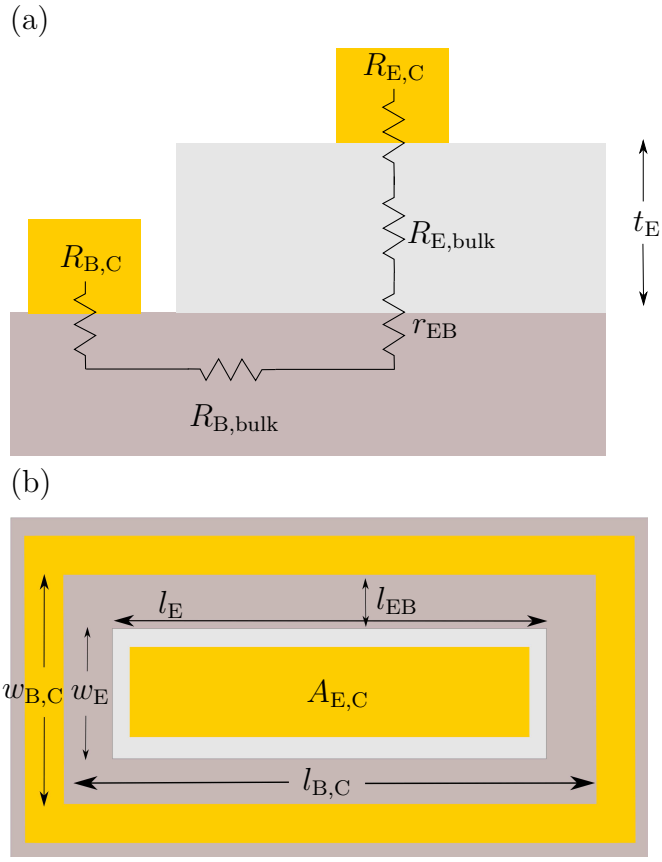

Figure B.1: (a) Side view and (b) top down view of the device mesa.

negative of the x-intercept on the resistance vs. TLM spacing plot.

The spreading resistance in the emitter mesa ($R_{\mathrm{E,bulk}}$) is calculated by first determining the bulk resistivity:

$$\rho_{\mathrm{E}} = R_{\mathrm{E,sheet}} t_{\mathrm{E}}, \tag{B.2}$$

where t_{E} is the thickness of the emitter contact layer. The spreading resistance is then

$$R_{\mathrm{E,bulk}} = \rho_{\mathrm{E}} \frac{t_{\mathrm{E}}}{l_{\mathrm{E}} w_{\mathrm{E}}} = R_{\mathrm{E,sheet}} \frac{t_{\mathrm{E}}^2}{l_{\mathrm{E}} w_{\mathrm{E}}}. \tag{B.3}$$

The next resistor in Fig. B.1(a) is r_{EB} or the dynamic resistance of the diode. This is the intrinsic, bias-dependent device resistance and we will leave this as an unknown. The bulk resistance in the base layer is

$$R_{\mathrm{B,bulk}} = R_{\mathrm{B,sheet}} \frac{l_{\mathrm{EB}}}{l_{\mathrm{B,C}}}. \tag{B.4}$$

Note that Eq. (B.4) is equal to the resistance of only one of the four sides of the access region in Fig. B.1(b). Therefore, we will only consider currents flowing into the part of the base contact whose length is labeled $l_{\mathrm{B,C}}$. The current flowing into this side of the contact (I') is given by:

$$I' = I \frac{l_{\mathrm{B,C}}}{2l_{\mathrm{B,C}} + 2w_{\mathrm{B,C}}}. \tag{B.5}$$

Finally, the resistance between the base contact and the base bulk is

$$R_{\mathrm{B,C}} = \frac{r_{\mathrm{B,C}}}{l_{\mathrm{B,C}}}, \tag{B.6}$$

where $r_{\mathrm{B,C}}$ is the contact resistance measured from the base TLMs. The reduced current I' also flows through $R_{\mathrm{B,C}}$.

Putting it all together, the voltage drop in the extrinsic regions at current I is:

$$\boxed{V_{\text{ext}} = I\left(\frac{r_{\text{E,C}}L_{\text{T}}}{A_{\text{E,C}}} + R_{\text{E,sheet}}\frac{t_{\text{E}}^2}{l_{\text{E}}w_{\text{E}}} + R_{\text{B,sheet}}\frac{l_{\text{EB}}}{2l_{\text{B,C}} + 2w_{\text{B,C}}} + \frac{r_{\text{B,C}}}{2l_{\text{B,C}} + 2w_{\text{B,C}}}\right)}. \quad \text{(B.7)}$$

Measurements of the contact and sheet resistance in the emitter and base layers thereby enable the complete determination of the extrinsic voltage drops.

Bibliography

[1] C. A. Mead, *Operation of tunnel-emission devices*, *Journal of Applied Physics* **32** (1961), no. 4.

[2] S. Sze and H. Gummel, *Appraisal of semiconductor-metal-semiconductor transistor*, *Solid-State Electronics* **9** (1966), no. 8 751 – 769.

[3] J. M. Shannon, *A majority-carrier camel diode*, *Applied Physics Letters* **35** (1979), no. 1.

[4] J. Shannon, *Hot-electron camel transistor*, *Solid-State and Electron Devices, IEE Journal on* **3** (September, 1979) 142–144.

[5] B. Ridley, *The diffusion of hot electrons across a semiconductor base*, *Solid-State Electronics* **24** (1981), no. 2 147 – 154.

[6] M. Heiblum, *Tunneling hot electron transfer amplifiers (THETA): Amplifiers operating up to the infrared*, *Solid-State Electronics* **24** (1981), no. 4 343 – 366.

[7] N. Yokoyama, K. Imamura, T. Ohshima, H. Nishi, S. Muto, K. Kondo, and S. Hiyamizu, *Tunneling hot electron transistor using GaAs/AlGaAs heterojunctions*, *Japanese Journal of Applied Physics* **23** (1984), no. 5A L311.

[8] N. Yokoyama, K. Imamura, T. Ohshima, H. Nishi, S. Muto, K. Kondo, and S. Hiyamizu, *Characterization of double heterojunction GaAs/AlGaAs hot electron transistors*, in *Electron Devices Meeting, 1984 International*, vol. 30, pp. 532–535, 1984.

[9] U. K. Reddy, J. Chen, C. K. Peng, and H. Morko, *InGaAs/InAlAs hot-electron transistor*, *Applied Physics Letters* **48** (1986), no. 26.

[10] N. Yokoyama, K. Imamura, H. Ohnishi, T. Mori, S. Muto, and A. Shibatomi, *Resonant-tunneling hot electron transistor (RHET)*, *Solid-State Electronics* **31** (1988), no. 34 577 – 582.

[11] A. F. J. Levi and T. H. Chiu, *Room-temperature operation of hot-electron transistors*, *Applied Physics Letters* **51** (1987), no. 13.

[12] A. F. J. Levi and T. H. Chiu, *Unipolar hot electron transistors*, *Physica Scripta* **1988** (1988), no. T23 227.

[13] M. Shur and L. F. Eastman, *Ballistic transport in semiconductor at low temperatures for low-power high-speed logic*, *Electron Devices, IEEE Transactions on* **26** (Nov, 1979) 1677–1683.

[14] C. R. Crowell, W. G. Spitzer, L. E. Howarth, and E. E. LaBate, *Attenuation length measurements of hot electrons in metal films*, *Phys. Rev.* **127** (Sep, 1962) 2006–2015.

[15] C. V. Shank, R. L. Fork, R. F. Leheny, and J. Shah, *Dynamics of photoexcited GaAs band-edge absorption with subpicosecond resolution*, *Phys. Rev. Lett.* **42** (Jan, 1979) 112–115.

[16] J. Shah, B. Deveaud, T. C. Damen, W. T. Tsang, A. C. Gossard, and P. Lugli, *Determination of intervalley scattering rates in GaAs by subpicosecond luminescence spectroscopy*, *Phys. Rev. Lett.* **59** (Nov, 1987) 2222–2225.

[17] P. Hesto, J.-F. Pone, and R. Castagne, *A proposal and numerical simulation of N^+NN^+ Schottky device for ballistic and quasiballistic electron spectroscopy*, *Applied Physics Letters* **40** (1982), no. 5.

[18] K. Hess and G. Iafrate, *Theory and applications of near ballistic transport in semiconductors*, *Proceedings of the IEEE* **76** (May, 1988) 519–532.

[19] J. R. Hayes, A. F. J. Levi, and W. Wiegmann, *Hot-electron spectroscopy of GaAs*, *Phys. Rev. Lett.* **54** (Apr, 1985) 1570–1572.

[20] A. F. J. Levi, J. R. Hayes, P. M. Platzman, and W. Wiegmann, *Injected-hot-electron transport in GaAs*, *Phys. Rev. Lett.* **55** (Nov, 1985) 2071–2073.

[21] M. Heiblum, M. I. Nathan, D. C. Thomas, and C. M. Knoedler, *Direct observation of ballistic transport in GaAs*, *Phys. Rev. Lett.* **55** (Nov, 1985) 2200–2203.

[22] A. F. J. Levi and T. H. Chiu, *Hot electron spectroscopy of GaAs*, *Physica B+C* **134** (1985), no. 13 480 – 486.

[23] P. England, J. R. Hayes, E. Colas, and M. Helm, *Hot-electron spectroscopy of Bloch electrons in high-order minibands in semiconductor superlattices*, *Phys. Rev. Lett.* **63** (Oct, 1989) 1708–1711.

[24] B. Brill and M. Heiblum, *Long-mean-free-path ballistic hot electrons in high-purity GaAs*, *Phys. Rev. B* **54** (Dec, 1996) R17280–R17283.

[25] M. Heiblum and M. Fischetti, *Ballistic hot-electron transistors*, *IBM Journal of Research and Development* **34** (1990), no. 4 530.

[26] S. Nakamura, M. Senoh, and T. Mukai, *High power InGaN/GaN double heterostructure violet light emitting diodes*, *Applied Physics Letters* **62** (1993), no. 19.

[27] S. Nakamura, T. Mukai, and M. Senoh, *Candela-class high-brightness InGaN/AlGaN double-heterostructure blue-light-emitting diodes*, *Applied Physics Letters* **64** (1994), no. 13.

[28] S. Nakamura, M. Senoh, S.-i. Nagahama, N. Iwasa, T. Yamada, T. Matsushita, H. Kiyoku, and Y. Sugimoto, *Characteristics of InGaN multi-quantum-well-structure laser diodes*, *Applied Physics Letters* **68** (1996), no. 23.

[29] S. Nakamura, M. Senoh, S.-i. Nagahama, N. Iwasa, T. Yamada, T. Matsushita, Y. Sugimoto, and H. Kiyoku, *Room-temperature continuous-wave operation of InGaN multi-quantum-well structure laser diodes*, *Applied Physics Letters* **69** (1996), no. 26.

[30] O. Ambacher, *Growth and applications of Group III-nitrides*, *Journal of Physics D: Applied Physics* **31** (1998), no. 20 2653.

[31] T. Hashimoto, F. Wu, J. S. Speck, and S. Nakamura, *A GaN bulk crystal with improved structural quality grown by the ammonothermal method*, *Nature Materials* **6** (2007) 568–571.

[32] M. H. Wong, S. Keller, S. D. Nidhi, D. J. Denninghoff, S. Kolluri, D. F. Brown, J. Lu, N. A. Fichtenbaum, E. Ahmadi, U. Singisetti, A. Chini, S. Rajan, S. P. DenBaars, J. S. Speck, and U. K. Mishra, *N-polar GaN epitaxy and high electron mobility transistors*, *Semiconductor Science and Technology* **28** (2013), no. 7 074009.

[33] F. Bernardini, V. Fiorentini, and D. Vanderbilt, *Spontaneous polarization and piezoelectric constants of III-V nitrides*, *Phys. Rev. B* **56** (Oct, 1997) R10024–R10027.

[34] C. Stampfl and C. G. Van de Walle, *Density-functional calculations for III-V nitrides using the local-density approximation and the generalized gradient approximation*, *Phys. Rev. B* **59** (Feb, 1999) 5521–5535.

[35] P. Rinke, M. Winkelnkemper, A. Qteish, D. Bimberg, J. Neugebauer, and M. Scheffler, *Consistent set of band parameters for the group-III nitrides AlN, GaN, and InN*, *Phys. Rev. B* **77** (Feb, 2008) 075202.

[36] K. H. Li, X. Liu, Q. Wang, and Z. Mi, *Ultralow-threshold electrically injected AlGaN nanowire ultraviolet lasers on Si operating at low temperature*, *Nature Nanotechnology* **10** (2015) 140–144.

[37] Y. Yue, Z. Hu, J. Guo, B. Sensale-Rodriguez, G. Li, R. Wang, F. Faria, B. Song, X. Gao, S. Guo, T. Kosel, G. Snider, P. Fay, D. Jena, and H. G. Xing, *Ultrascaled InAlN/GaN High Electron Mobility Transistors with Cutoff Frequency of 400 GHz*, *Japanese Journal of Applied Physics* **52** (2013), no. 8S 08JN14.

[38] Y. Tang, K. Shinohara, D. Regan, A. Corrion, D. Brown, J. Wong, A. Schmitz, H. Fung, S. Kim, and M. Micovic, *Ultrahigh-Speed GaN High-Electron-Mobility Transistors with f_T/f_{max} of 454/444 GHz*, *Electron Device Letters, IEEE* **36** (June, 2015) 549–551.

[39] D. Denninghoff, J. Lu, E. Ahmadi, S. Keller, and U. Mishra, *N-polar GaN/InAlN/AlGaN MIS-HEMTs with 1.89 S/mm extrinsic transconductance, 4 A/mm drain current, 204 GHz f_T and 405 GHz f_{max}*, in *Device Research Conference (DRC), 2013 71st Annual*, pp. 197–198, June, 2013.

[40] Y.-F. Wu, M. Moore, A. Saxler, T. Wisleder, and P. Parikh, *40-W/mm Double Field-plated GaN HEMTs*, in *Device Research Conference, 2006 64th*, pp. 151–152, June, 2006.

[41] D. Jena, *Polarization induced electron populations in III-V nitride semiconductors: Transport, growth, and device applications.* PhD thesis, University of California, Santa Barbara, 2003.

[42] O. Ambacher, J. Smart, J. R. Shealy, N. G. Weimann, K. Chu, M. Murphy, W. J. Schaff, L. F. Eastman, R. Dimitrov, L. Wittmer, M. Stutzmann, W. Rieger, and J. Hilsenbeck, *Two-dimensional electron gases induced by spontaneous and piezoelectric polarization charges in N- and Ga-face AlGaN/GaN heterostructures*, *Journal of Applied Physics* **85** (1999), no. 6 3222–3233.

[43] T. Zhu and R. Oliver, *Unintentional doping in GaN*, *Phys. Chem. Chem. Phys* **14** (2012) 9558–9573.

[44] P. Hohenberg and W. Kohn, *Inhomogeneous electron gas*, *Phys. Rev.* **136** (1964) B864–B871.

[45] M. L. Cohen and T. K. Bergstresser, *Band structures and pseudopotential form factors for fourteen semiconductors of the diamond and zinc-blende structures*, *Phys. Rev.* **141** (Jan, 1966) 789–796.

[46] M. Nightingale and C. Umrigar, *Quantum Monte Carlo Methods in Physics and Chemistry.* Nato Science Series C, 1998.

[47] G. Bastard, *Superlattice band structure in the envelope-function approximation*, *Phys. Rev. B* **24** (1981) 5693–5697.

[48] G. Bastard, *Wave Mechanics Applied to Semiconductor Heterostructures*. Les Éditions de Physique, 1991.

[49] G. Wentzel *Zeits. f. Physik* **38** (1926) 518.

[50] H. Kramers *Zeits. f. Physik* **39** (1926) 828.

[51] L. Brillouin *Comptes Rendus* **183** (1926) 24.

[52] R. Shankar, *Principles of Quantum Mechanics*. Springer, 2 ed., 1994.

[53] P. Morse and H. Feshbach, *Methods of Theoretical Physics*, vol. 2. McGraw-Hill, 1953.

[54] W. W. Lui and M. Fukuma, *Exact solution of the Schrödinger equation across an arbitrary one dimensional piecewise linear potential barrier*, *Journal of Applied Physics* **60** (1986), no. 5 1555–1559.

[55] K. F. Brennan and C. J. Summers, *Theory of resonant tunneling in a variably spaced multiquantum well structure: An Airy function approach*, *Journal of Applied Physics* **61** (1987), no. 2 614–623.

[56] D. C. Hutchings, *Transfer matrix approach to the analysis of an arbitrary quantum well structure in an electric field*, *Applied Physics Letters* **55** (1989), no. 11 1082–1084.

[57] E. N. Glytsis, T. K. Gaylord, and K. F. Brennan, *Theory and design of semiconductor electronwave interference filter/emitters*, *Journal of Applied Physics* **66** (1989), no. 12 6158–6167.

[58] O. M. Probst, *Tunneling through arbitrary potential barriers and the apparent barrier height*, *American Journal of Physics* **70** (2002), no. 11 1110–1116.

[59] Y. Ando and T. Itoh, *Calculation of transmission tunneling current across arbitrary potential barriers*, *Journal of Applied Physics* **61** (1987), no. 4 1497–1502.

[60] J.-G. S. Demers and R. Maciejko, *Propagation matrix formalism and efficient linear potential solution to Schrödinger's equation*, *Journal of Applied Physics* **90** (2001), no. 12 6120–6129.

[61] B. Jonsson and S. Eng, *Solving the Schrödinger equation in arbitrary quantum-well potential profiles using the transfer matrix method*, *Quantum Electronics, IEEE Journal of* **26** (1990), no. 11 2025–2035.

[62] C. S. Lent and D. J. Kirkner, *The quantum transmitting boundary method*, *Journal of Applied Physics* **67** (1990), no. 10 6353–6359.

[63] W. R. Frensley, *Numerical evaluation of resonant states*, *Superlattices and Microstructures* **11** (1992), no. 3 347 – 350.

[64] C. L. Fernando and W. R. Frensley, *An efficient method for the numerical evaluation of resonant states*, *Journal of Applied Physics* **76** (1994), no. 5 2881–2886.

[65] R. Butt, *Introduction to Numerical Analysis Using MATLAB*. Infinity Science Press, 2008.

[66] C. Juang, K. J. Kuhn, and R. B. Darling, *Stark shift and field-induced tunneling in $Al_xGa_{1-x}As/GaAs$ quantum-well structures*, *Phys. Rev. B* **41** (1990) 12047–12053.

[67] R. Tsu and L. Esaki, *Tunneling in a finite superlattice*, *Applied Physics Letters* **22** (1973), no. 11 562–564.

[68] U. K. Mishra and J. Singh, *Semiconductor Device Physics and Design*. Springer, 2008.

[69] I. Ohdomari, T. S. Kuan, and K. N. Tu, *Microstructure and Schottky barrier height of iridium silicides formed on silicon*, *Journal of Applied Physics* **50** (1979), no. 11 7020–7029.

[70] J. L. Freeouf, T. N. Jackson, S. E. Laux, and J. M. Woodall, *Effective barrier heights of mixed phase contacts: Size effects*, *Applied Physics Letters* **40** (1982), no. 7 634–636.

[71] T. Okumura and K. N. Tu, *Analysis of parallel Schottky contacts by differential internal photoemission spectroscopy*, *Journal of Applied Physics* **54** (1983), no. 2 922–927.

[72] A. Tanabe, K. Konuma, N. Teranishi, S. Tohyama, and K. Masubuchi, *Influence of Fermi-level pinning on barrier height inhomogeneity in PtSi/pSi Schottky contacts*, *Journal of Applied Physics* **69** (1991), no. 2 850–853.

[73] R. T. Tung, *Electron transport at metal-semiconductor interfaces: General theory*, *Phys. Rev. B* **45** (Jun, 1992) 13509–13523.

[74] R. T. Tung, *Electron transport of inhomogeneous schottky barriers*, *Applied Physics Letters* **58** (1991), no. 24 2821–2823.

[75] S. Dasgupta, Nidhi, D. F. Brown, F. Wu, S. Keller, J. S. Speck, and U. K. Mishra, *Ultralow nonalloyed ohmic contact resistance to self aligned N-polar GaN high electron mobility transistors by In(Ga)N regrowth*, *Applied Physics Letters* **96** (2010), no. 14.

[76] G. Gupta, E. Ahmadi, K. Hestroffer, E. Acuna, and U. Mishra, *Common emitter current gain >1 in III-N hot electron transistors with 7-nm GaN/InGaN base*, *Electron Device Letters, IEEE* **36** (May, 2015) 439–441.

[77] H. Li, S. Keller, S. H. Chan, J. Lu, S. P. DenBaars, and U. K. Mishra, *Unintentional gallium incorporation in AlN and its impact on the electrical properties of GaN/AlN and GaN/AlN/AlGaN heterostructures*, *Semiconductor Science and Technology* **30** (2015), no. 5 055015.

[78] S. Keller, N. A. Fichtenbaum, F. Wu, D. Brown, A. Rosales, S. P. DenBaars, J. S. Speck, and U. K. Mishra, *Influence of the substrate misorientation on the properties of N-polar GaN films grown by metal organic chemical vapor deposition*, *Journal of Applied Physics* **102** (2007), no. 8.

[79] M. Sumiya, K. Yoshimura, T. Ito, K. Ohtsuka, S. Fuke, K. Mizuno, M. Yoshimoto, H. Koinuma, A. Ohtomo, and M. Kawasaki, *Growth mode and surface morphology of a GaN film deposited along the N-face polar direction on c-plane sapphire substrate*, *Journal of Applied Physics* **88** (2000), no. 2.

[80] S. Dasgupta, N. Nidhi, A. Raman, J. Speck, and U. K. Mishra, *Room temperature operation and DC characteristics of InAlN/GaN/AlGaN hot electron transistors with common base transfer ratio $\alpha = 0.97$*, in *Device Research Conference (DRC), 2010*, pp. 133–134, June, 2010.

[81] G. Gupta, M. Laurent, H. Li, D. Suntrup, E. Acuna, S. Keller, and U. Mishra, *Design space of III-N hot electron transistors using AlGaN and InGaN polarization-dipole barriers*, *Electron Device Letters, IEEE* **36** (Jan, 2015) 23–25.

[82] S. Chand and J. Kumar, *Effects of barrier height distribution on the behavior of a Schottky diode*, *Journal of Applied Physics* **82** (1997), no. 10.

[83] D. A. Browne, B. Mazumder, Y.-R. Wu, and J. S. Speck, *Electron transport in unipolar InGaN/GaN multiple quantum well structures grown by NH3 molecular beam epitaxy*, *Journal of Applied Physics* **117** (2015), no. 18.

[84] M. J. Galtrey, R. A. Oliver, M. J. Kappers, C. J. Humphreys, D. J. Stokes, P. H. Clifton, and A. Cerezo, *Three-dimensional atom probe studies of an $In_xGa_{1-x}N$/GaN multiple quantum well structure: Assessment of possible indium clustering*, *Applied Physics Letters* **90** (2007), no. 6.

[85] M. J. Galtrey, R. A. Oliver, M. J. Kappers, C. J. Humphreys, P. H. Clifton, D. Larson, D. W. Saxey, and A. Cerezo, *Three-dimensional atom probe analysis of green- and blue-emitting $In_xGa_{1-x}N/GaN$ multiple quantum well structures*, *Journal of Applied Physics* **104** (2008), no. 1.

[86] R. Shivaraman, Y. Kawaguchi, S. Tanaka, S. P. DenBaars, S. Nakamura, and J. S. Speck, *Comparative analysis of $20\bar{2}1$ and $20\overline{21}$ semipolar GaN light emitting diodes using atom probe tomography*, *Applied Physics Letters* **102** (2013), no. 25.

[87] T.-J. Yang, R. Shivaraman, J. S. Speck, and Y.-R. Wu, *The influence of random indium alloy fluctuations in indium gallium nitride quantum wells on the device behavior*, *Journal of Applied Physics* **116** (2014), no. 11.

[88] P. Ruterana, S. Kret, A. Vivet, G. Maciejewski, and P. Dluzewski, *Composition fluctuation in InGaN quantum wells made from molecular beam or metalorganic vapor phase epitaxial layers*, *Journal of Applied Physics* **91** (2002), no. 11.

[89] K. H. Baloch, A. C. Johnston-Peck, K. Kisslinger, E. A. Stach, and S. Gradeak, *Revisiting the In-clustering question in InGaN through the use of aberration-corrected electron microscopy below the knock-on threshold*, *Applied Physics Letters* **102** (2013), no. 19.

[90] S. Chand and J. Kumar, *Evidence for the double distribution of barrier heights in Pd_2Si/n-Si Schottky diodes from I - V - T measurements*, *Semiconductor Science and Technology* **11** (1996), no. 8 1203.

[91] A. F. Özdemir, A. Turut, and A. Kökçe, *The double Gaussian distribution of barrier heights in Au/n-GaAs Schottky diodes from I-V-T characteristics*, *Semiconductor Science and Technology* **21** (2006), no. 3 298.

[92] İ. Taşçıoğlu, U. Aydemir, and Ş. Altındal, *The explanation of barrier height inhomogeneities in Au/n-Si Schottky barrier diodes with organic thin interfacial layer*, *Journal of Applied Physics* **108** (2010), no. 6.

[93] W. J. Kaiser and L. D. Bell, *Direct investigation of subsurface interface electronic structure by ballistic-electron-emission microscopy*, *Phys. Rev. Lett.* **60** (Apr, 1988) 1406–1409.

[94] L. D. Bell and W. J. Kaiser, *Observation of interface band structure by ballistic-electron-emission microscopy*, *Phys. Rev. Lett.* **61** (Nov, 1988) 2368–2371.

[95] A. E. Fowell, R. H. Williams, B. E. Richardson, and T. H. Shen, *The Au/CdTe interface: an investigation of electrical barriers by ballistic electron emission microscopy*, *Semiconductor Science and Technology* **5** (1990), no. 4 348.

[96] H. Palm, M. Arbes, and M. Schulz, *Fluctuations of the Au-Si(100) Schottky barrier height*, *Phys. Rev. Lett.* **71** (Oct, 1993) 2224–2227.

[97] A. A. Talin, R. S. Williams, B. A. Morgan, K. M. Ring, and K. L. Kavanagh, *Nanometer-resolved spatial variations in the Schottky barrier height of a Au/n-type GaAs diode*, *Phys. Rev. B* **49** (Jun, 1994) 16474–16479.

[98] A. Fowell, A. Cafolla, B. Richardson, T.-H. Shen, M. Elliott, D. Westwood, and R. Williams, *Probing heterojunctions by ballistic electron emission microscopy*, *Applied Surface Science* **5658, Part 2** (1992), no. 0 622 – 627.

[99] M.-l. Ke, D. I. Westwood, S. Wilks, S. Heghoyan, A. Kestle, C. C. Matthai, B. E. Richardson, and R. H. Williams, *Ballistic electron emission microscopy of strained and relaxed $In_{0.35}Ga_{0.65}As/AlAs$ interfaces*, *Journal of Vacuum Science & Technology B* **13** (1995), no. 4 1684–1688.

[100] X. Zhou, E. T. Yu, D. Florescu, J. C. Ramer, D. S. Lee, and E. A. Armour, *Observation of subsurface monolayer thickness fluctuations in InGaN/GaN quantum wells by scanning capacitance microscopy and spectroscopy*, *Applied Physics Letters* **85** (2004), no. 3.

[101] D. S. Li, H. Chen, H. B. Yu, H. Q. Jia, Q. Huang, and J. M. Zhou, *Dependence of leakage current on dislocations in GaN-based light-emitting diodes*, *Journal of Applied Physics* **96** (2004), no. 2.

[102] S. W. Lee, D. C. Oh, H. Goto, J. S. Ha, H. J. Lee, T. Hanada, M. W. Cho, T. Yao, S. K. Hong, H. Y. Lee, S. R. Cho, J. W. Choi, J. H. Choi, J. H. Jang, J. E. Shin, and J. S. Lee, *Origin of forward leakage current in GaN-based light-emitting devices*, *Applied Physics Letters* **89** (2006), no. 13.

[103] J. W. P. Hsu, M. J. Manfra, D. V. Lang, S. Richter, S. N. G. Chu, A. M. Sergent, R. N. Kleiman, L. N. Pfeiffer, and R. J. Molnar, *Inhomogeneous spatial distribution of reverse bias leakage in GaN Schottky diodes*, *Applied Physics Letters* **78** (2001), no. 12.

[104] B. Mazumder, S. W. Kaun, J. Lu, S. Keller, U. K. Mishra, and J. S. Speck, *Atom probe analysis of AlN interlayers in AlGaN/AlN/GaN heterostructures*, *Applied Physics Letters* **102** (2013), no. 11.

[105] G. Gupta, E. Ahmadi, K. Hestroffer, E. Acuna, and U. Mishra, *Common emitter current gain > 1 in III-N hot electron transistors with 7-nm GaN/InGaN base*, *Electron Device Letters, IEEE* **36** (May, 2015) 439–441.

[106] M. Lundstrom, *Fundamentals of Carrier Transport*. Cambridge University Press, 2009.

[107] J. Singh, *Electronic and Optoelectronic Properties of Semiconductor Structures*. Cambridge University Press, 2003.

[108] C. Jacoboni and P. Lugli, *The Monte Carlo Method for Semiconductor Device Simulation*. Springer Science and Business Media, 1989.

[109] H. Morkoç, *Nitride Semiconductor Devices: Fundamentals and Applications*. Wiley, 2013.

[110] B. Ridley, *Quantum Processes in Semiconductors*. Oxford University Press, 1982.

[111] H. Arabshahi, *Simulations of electron transport in GaN devices*. PhD thesis, Durham University, 2012.

[112] B. K. Ridley, *Hot phonons in high-field transport*, *Semiconductor Science and Technology* **4** (1989), no. 12 1142.

[113] C.-K. Sun, Y.-L. Huang, S. Keller, U. K. Mishra, and S. P. DenBaars, *Ultrafast electron dynamics study of GaN*, *Phys. Rev. B* **59** (Jun, 1999) 13535–13538.

[114] M. Goano, E. Bellotti, E. Ghillino, G. Ghione, and K. F. Brennan, *Band structure nonlocal pseudopotential calculation of the III-nitride wurtzite phase materials system. Part I. Binary compounds GaN, AlN, and InN*, *Journal of Applied Physics* **88** (2000), no. 11.

[115] M. Piccardo, L. Martinelli, J. Iveland, N. Young, S. P. DenBaars, S. Nakamura, J. S. Speck, C. Weisbuch, and J. Peretti, *Determination of the first satellite valley energy in the conduction band of wurtzite GaN by near-band-gap photoemission spectroscopy*, *Phys. Rev. B* **89** (Jun, 2014) 235124.

[116] L. C. de Carvalho, A. Schleife, and F. Bechstedt, *Influence of exchange and correlation on structural and electronic properties of AlN, GaN, and InN polytypes*, *Phys. Rev. B* **84** (Nov, 2011) 195105.

[117] E. Conwell and V. F. Weisskopf, *Theory of impurity scattering in semiconductors*, *Phys. Rev.* **77** (Feb, 1950) 388–390.

[118] H. Piprek, *Nitride Semiconductor Devices: Principles and Simulation*. Wiley, 2007.

[119] C. Bulutay, B. K. Ridley, and N. A. Zakhleniuk, *Electron momentum and energy relaxation rates in GaN and AlN in the high-field transport regime*, *Phys. Rev. B* **68** (Sep, 2003) 115205.

[120] H. Ye, G. W. Wicks, and P. M. Fauchet, *Hot electron relaxation time in GaN*, *Applied Physics Letters* **74** (1999), no. 5 711–713.

[121] S. K. Tripathy, G. Xu, X. Mu, Y. J. Ding, K. Wang, Y. Cao, D. Jena, and J. B. Khurgin, *Evidence of hot electrons generated from an AlN/GaN high electron mobility transistor*, *Applied Physics Letters* **92** (2008), no. 1.

[122] N. M. Stanton, A. J. Kent, A. V. Akimov, P. Hawker, T. S. Cheng, and C. T. Foxon, *Energy relaxation by hot electrons in n-GaN epilayers*, *Journal of Applied Physics* **89** (2001), no. 2 973–979.

[123] N. Balkan, M. C. Arikan, S. Gokden, V. Tilak, B. Schaff, and R. J. Shealy, *Energy and momentum relaxation of hot electrons in GaN/AlGaN*, *Journal of Physics: Condensed Matter* **14** (2002), no. 13 3457.

[124] J. Shah, *Hot electrons and phonons under high intensity photoexcitation of semiconductors*, *Solid-State Electronics* **21** (1978), no. 1 43 – 50.

[125] S. Wu, P. Geiser, J. Jun, J. Karpinski, D. Wang, and R. Sobolewski, *Time-resolved intervalley transitions in GaN single crystals*, *Journal of Applied Physics* **101** (2007), no. 4.

[126] M. Wraback, H. Shen, S. Rudin, E. Bellotti, M. Goano, J. C. Carrano, C. J. Collins, J. C. Campbell, and R. D. Dupuis, *Direction-dependent band nonparabolicity effects on high-field transient electron transport in GaN*, *Applied Physics Letters* **82** (2003), no. 21 3674–3676.

[127] G. Gupta, M. Laurent, J. Lu, S. Keller, and U. K. Mishra, *Design of polarization-dipole-induced isotype heterojunction diodes for use in III-N hot electron transistors*, *Applied Physics Express* **7** (2014), no. 1 014102.

[128] S. Dasgupta, J. Lu, Nidhi, A. Raman, C. Hurni, G. Gupta, J. S. Speck, and U. K. Mishra, *Estimation of hot electron relaxation time in GaN using hot electron transistors*, *Applied Physics Express* **6** (2013), no. 3 034002.